

Plastics & Rubber Singapore Journal

[Volume 16]



The Plastic and Rubber Institute of Singapore

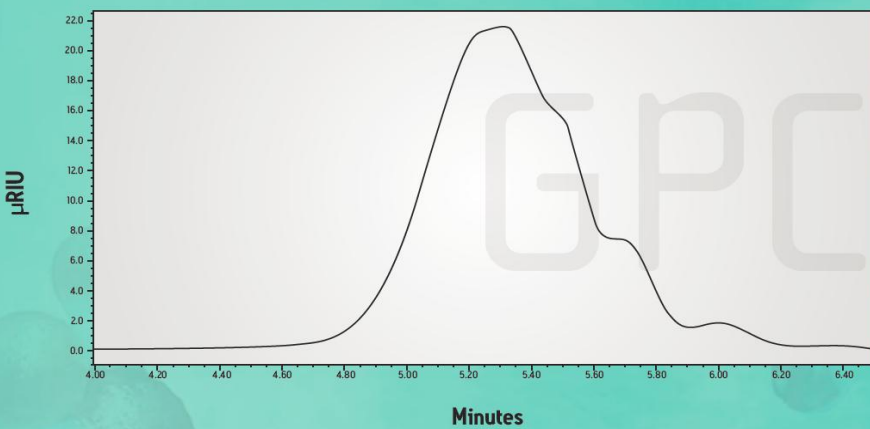
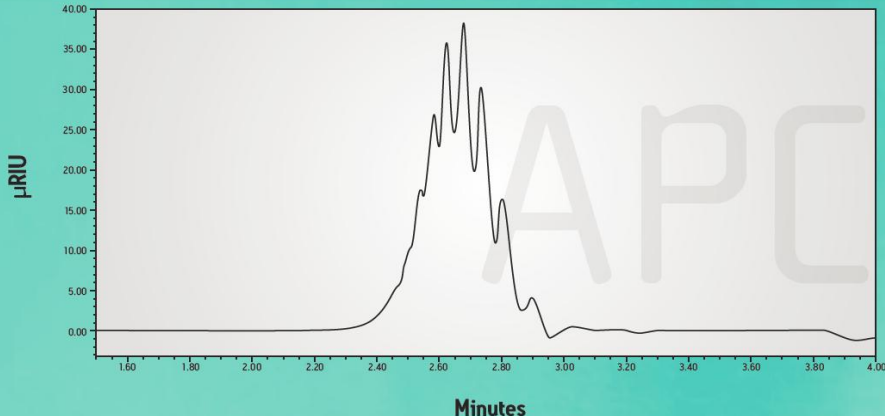
[An official publication of the Plastic and Rubber Institute of Singapore]



Waters

THE SCIENCE OF WHAT'S POSSIBLE.®

APC vs. GPC with narrow standard polystyrene $M_p = 510$



THE PATH TO INNOVATION.

WITH ADVANCED POLYMER CHROMATOGRAPHY, IT'S VERY CLEAR.

More information about your polymers in less time. Every time. That's what it takes to bring innovation into advanced Chemical Materials markets. And that's exactly what you can expect from the truly unique instrumentation and column chemistries of the Waters® ACQUITY Advanced Polymer Chromatography® (APC™) System.

To learn more about why polymer chromatography will never be the same again, visit waters.com/APC or call 6593 7111



CONTENTS

Foreword

PRIS Management Committee 2015

Corporate members of PRIS

A Message from the President of PRIS

TECHNICAL PAPERS

A Practical Combination Test Method for Effectively Evaluation of the Rubber Materials for Fenders

By Kousik Kumar Mishra

Copolymerization Studied with MALDI ToF MS

By Alex van Herk

Electrode Nano-materials for Energy Storage and Conversion Application

By Tan Hui Teng, Alex Yan Qingyu, Ho Keen Hoe, Lee Hiang Wee, Ng Ming Xuan and Ho Thiam Aik

Tin-lead Alloy/Carbon Polymeric Composites with High Electrical Conductivity

By Yongzheng Pan

Synthesis and Characterisation of Anode Nano-materials for Lithium Ion Batteries

By Tan Hui Teng, Alex Yan Qingyu, Kee Yong Yao, Chan Zing Weng, Kevin Leow Cheng Sheng and Ho Thiam Aik

Film for Filtering Infra-Red Radiation from the Sunlight

By Kang Semi, Kim Jee Hyun, Murali Krishnaswamy and Hong Han

Volatile Corrosion Inhibitor (VAPPRO 872)

By Tong Shaw Wen, Geradine Yeo Li Yee, Quek Xin Lin, Ho Thiam Aik and Moe Patrick

Optimisation and Characterisation of Commercial Water-based Corrosion Inhibitor (VCI)

By H. Bryan Lim Han Yuan, Alex Low Shaw Boon, Cheang Tze Mun, Ho Thiam Aik and Moe Patrick

Foreword

The Plastics and Rubber Institute of Singapore (PRIS) is a national academic organization established for members who are in businesses related to plastic and rubbers. The members are from manufacturing industries, trading companies, service business, education and research institutes and students from polytechnics and universities. PRIS publishes journals periodically aiming to meet the interest of and promote information exchange in the local industries and within researchers pertaining to plastics, rubbers and additives as well as relate interesting high-tech areas.

The committee of PRIS is publishing its 16th issue of Plastic and Rubber Singapore Journal. This issue includes methods for characterization of rubber products and investigation of copolymerization; nano-materials and polymer composites for energy applications, functional films and inhibitors for corrosion control etc. I would like to take this opportunity to thank our members, corporate members and all related persons and companies for their strong support. I would like to thank all the authors for their dedicated contribution for this journal.

I am grateful to Dr. Zhao Jianhong and Dr. Ludger Paul Stubbs for reviewing the papers. I am also grateful to Ms Jane Koh for her help and coordinate for the publication of the hard copies soon. The support from Mr. Nee Pai How, Mr. Sanjeev Kumar, Dr. Gu Haiwen and Mr. Ong Kian Soo is also appreciated.

Thank you.

Hong Han

Editor

PRIS Management Committee 2015

| | |
|------------------------------|--|
| Dr Zhao Jianhong | - President |
| Mr Ong Kian Soo | - Vice-President / Social Secretary |
| Mr Sanjeev Kumar | - Vice-President |
| Mr Nee Pai How | - Honorary Secretary |
| Dr Gu Haiwen | - Honorary Treasurer |
| Mr Ho Thiam Aik | - Membership Secretary (Student Affairs) |
| Dr Hong Han | - Publication Secretary |
| Dr Ludger Paul Stubbs | - Technical Secretary |
| Dr Pan Yongzheng | - Education Secretary |
| Dr Daniel Wang SF | - Committee Member |
| Dr Lau Soo Khim | - Committee Member |
| Mr Shi Junhao | - Committee Member |

Corporate Members and Supporting Companies and organizations

Apollo International Limited
Chemart (S) Pte Ltd
HLN Rubber Products Pte Ltd
LMS Technologies Pte Ltd
Purac Asia Pacific Pte Ltd
Quantum Technologies Global Pte Ltd
RTP Company (S) Pte Ltd
Trelleborg Marine Systems Asia Pte Ltd
Mindtrac (S) Pte Ltd
East Chemical Pte Ltd
Maha Chemicals (Asia) Pte Ltd
Zwick Asia Pte Ltd
TUV SUD PSB
Chatsworth Associates Pte Ltd
Singapore Polytechnic
Institute of material Research and Engineering Singapore (IMRE)
Institute of Chemical & Engineering Sciences Singapore (ICES)
Singapore Institute of Manufacturing Technology (SIMTech)
Oil & Colour Chemists' Association (OCCA)
S'pore Chemical Industry Council Limited (SCIC)
Plastics & Rubber Institute Malaysia (PRIM)

A Message from the President of PRIS

The Plastics and Rubber Institute of Singapore (PRIS) is very proud to present you this issue of Plastics and Rubber Singapore – an official technical journal of the Institute.

Plastics and rubbers are nowadays widely used in all walks of our life playing irreplaceable roles. Though some of the manufacturing related processes have moved out of Singapore, polymeric material applications, the science and technologies are getting more and more important for our future development. As the national professional society for the plastic and rubber industry, PRIS has consistently devoted over the past 36 years since its establishment to the cause of developing, promoting, and introducing new and advanced polymer science and technologies to the Singapore plastics and rubber industry.

PRIS acts as the centre for promoting the interests of its members through a variety of technical activities such as regular workshop, seminars, conferences, training courses, and visits to manufacturing plants and industrial sites. We also organize various networking and entertaining events for members to communicate and exchange view in friendly and relaxed environment. Publication of the Journal has served as a means for technical communications, exchange of views, and promotion of new technologies. This issue of the Journal has included a few selected papers that were presented at our meeting and seminars in the past year for the benefit of our members and readers; it is also glad to see that a few papers are authored by teachers and students from Singapore Polytechnic.

I would like to take this opportunity to thank all PRIS members for their support rendered to the Management Committee over the past years. I would also like to congratulate Dr. Hong Han, the Editor of the Journal, and the Journal sub-Committee members Dr. Ludger Stubs, Dr. Pan Yongzheng, Mr. Ong Kian Soo, and Ms Jane Koh, for the excellent job done throughout the process of the publication.

Finally, on behalf of the Institute, I would like to thank our corporate members for their supports in the publication of the journal.

Dr. Zhao Jianhong

President

The Plastics and Rubber Institute of Singapore

A Practical Combination Test Method for Effectively Evaluation of the Rubber Materials for Fenders

Kousik Kumar Mishra

4 Jalan Pesawat Singapore 619362

Abstract A reliable, viable analytical method to assess the composition of recently procured fenders prior to delivery has been developed, using a simple sampling procedure from the surface of the fender. This new technique will help to ensure that fenders supplied use the correct quality of rubber compound required to adhere to the specification. The recommended tests to evaluate the quality of fenders, based on a sample of only 20-50grams which can be easily gathered by obtaining scrapings from the final product prior to installation, without affecting the fenders performance during application.

Keywords: fender; quality; recycled rubber; test.

1. Introduction

1.1 Fender system:

Fendering systems are mission critical equipment for marine environments globally. Long gone are the days of wooden or rope fenders, and the use of rubber has become standard best practice. Although rubber fenders have a long lifecycle, ultimately it is still limited. Depending on the environment and quality of the fender itself, the expected average lifespan will be approximately 15 to 20 years. Designing a fender system requires engineers to determine the berthing energy of a vessel or range of vessels that are likely to be docked against the system, then determining what capacity the fender needs to have to absorb that kinetic energy. Finally, engineers must find a way to avoid creating too much force and damaging either the wharf structure or vessel.

It's accepted that high quality fenders can add value to port operations as sourcing quality materials and fully tested compounds allows ports to drive cost efficiencies, minimise maintenance requirements and reducing the risk of incidents. High quality fenders also have a longer service life and, due to reduced maintenance requirements, also lead to fewer "lost" days for ports, and their shipping operators. In addition to these commercial concerns, fendering systems are a port's first line of defence when a vessel comes into dock and play a key role in protecting the safety of port personnel, vessel crew, cargo and infrastructure.

However, there has been a worrying trend becoming more pronounced across the industry in recent years, of putting up front costs higher on the agenda than whole life costs. Although this enables immediate cost savings for procurement managers it means that, over the course of the fender's lifecycle, costs will be higher. Some unscrupulous fender suppliers are taking the opportunity to undercut reputable fender manufacturers by supplying lower cost, but lower quality fenders. They are able to elicit cost savings to pass on to their customers (in the immediate term) in two ways:

- By using a higher percentage of recycled rubber within the fenders, instead of virgin rubber
- Replacing carbon black fillers with non-reinforcing fillers

A simplified comparison chart representing the whole life cost differences between the two can be found below:

| Spending requirements | Low quality fender | High quality fender |
|--------------------------------------|--------------------|---------------------|
| Purchase price of a CONE 1000 fender | \$8,000 | \$10000 |
| Installation | \$4000 | \$4000 |
| Replacement after five years | \$9200 | n/a |
| Re-installation | \$6000 | n/a |
| Maintenance | \$9000 | \$4000 |
| Maintenance installation | \$12000 | \$4800 |
| Total 10 year whole life cost | \$48200 | \$22800 |

These manufacturers also ‘copy’ correction factors from reputable manufacturers without understanding these factors are derived based on both rubber compound used as well as fender geometry. They do not make any investment in PIANC Type approved fenders.

1.2 Setting the Standards

“Although PIANC is not in a position where it may “regulate the industry” or deliver any certification, PIANC is very careful to promote best practice. We also stress that in the long term, through life cycle approaches, it is recommended to use the most adapted, strong and resistant fender protection to quays” mentioned by Geoffrey Caude, PIANC President, 2011. There are a number of different standards used worldwide to design fender systems but the most commonly used is PIANC’s “Guidelines for the design of fender systems, 2002”, which was updated from its predecessor of 1984. Although PIANC set out these guidelines, they do not regulate the industry, or indeed, enforce the guidelines in practical terms. This has led to some fender suppliers misusing PIANC “certification” by applying it to fenders that use higher percentages of filler and recycled rubber than is appropriate. PIANC’s guidelines specify that robust material testing is a necessity, and the fact that this is not routinely performed by all suppliers as part of their quality assurance process is a serious concern. Laboratory and full scale testing are fundamental to the design and production of mission critical equipment and the industry needs the reassurance that both sets of testing have been performed. Some suppliers are able to cut costs though replacing natural rubber with reclaimed rubber, and using large amounts of non-reinforcing fillers, which is a poor substitute for the carbon black reinforcing filler used in high quality fenders. These lower cost fenders, therefore, do not meet the required specifications, won’t perform adequately whilst they’re in use and, as such, won’t have the product lifecycle they are claimed to have. Additionally, port owners, contractors and consultants have no simple method available to test the quality of the fender’s material once it is purchased and installed.

A new analytical test has been developed to help buyers understand and substantiate what is in a fender and ensure that port owners, operators and contractors can ensure the highest quality of fenders going forward. Both chemical and physical testing are required to verify the rubber quality of the fender and ensure that it remains stable and suitable for the use it was intended for, throughout its lifecycle, to ensure maximum protection of the port infrastructure and the vessels that come to berth there.

2. Methods

To demonstrate and quantify the difference in performance characteristics of a high quality and low quality fender, the following tests were carried out in an independent third party laboratory:

- Comparison of the physical properties of the rubber samples. The samples were cut from two commercial sized fenders: one a typical high quality fender, and one a typical low cost fender
- Comparison of the chemical properties of the fenders. The samples were taken from the fender surface of two commercial sized fenders: one a typical high quality fender, and one a typical low cost fender.

The following tests were conducted:

| Physical analysis:Test | Equipment Used | Expected Standard |
|------------------------|-------------------------|-------------------|
| Density | Weighing balance | ISO 2781 |
| Hardness | Shore A hardness tester | ASTM D2240 |
| Tensile strength | Universal test machine | ASTM D412 |
| Elongation at break | Universal test machine | ASTM D412 |

Chemical analysis:

| Test | Equipment Used | Expected Standard |
|---|-----------------|-------------------|
| Polymer (virgin plus recycled rubber) % | TGA /FTIR | ASTM D6370/D297 |
| Carbon black % | TGA /FTIR | ASTM D6370/D297 |
| Ash % | TGA | ASTM D297 |
| Calcium Carbonate (white filler %) | Chemical method | ASTM D297 |

1. For further information on TGA and FTIR equipment, please see footnote [2].

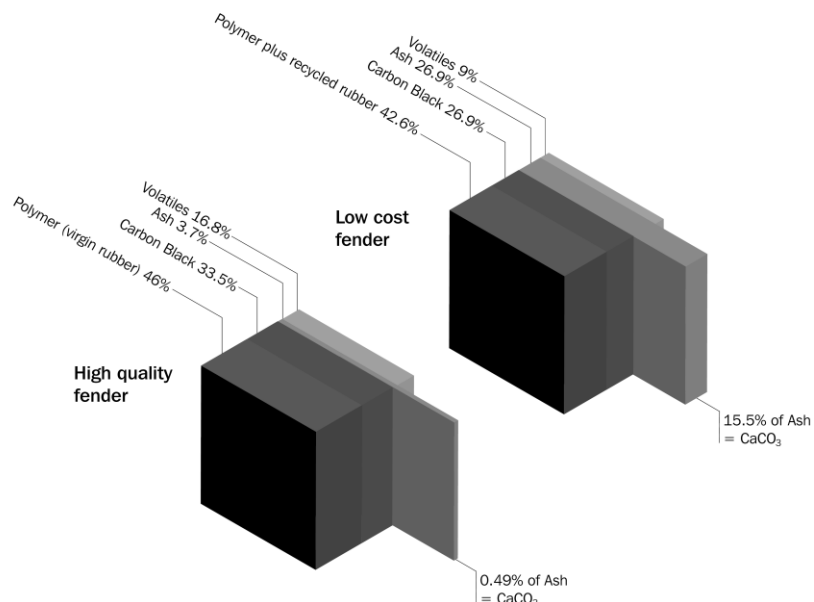
3. Results and discussion

Physical analysis:

| Test | Standard | High quality fender | Low cost fender | Requirement |
|------------------------|------------|---------------------|-----------------|--------------------|
| Density (g/cc) | ISO 2781 | 1.15 | 1.29 | Not specified |
| Hardness (shore A) | ASTM D2240 | 67 | 71 | Max. 78 |
| Tensile Strength (Mpa) | ASTM D2240 | 15.4 | 9.3 | 15.2 - 13.6 (Note) |
| Elongation @ Break (%) | ASTM D2240 | 364 | 278 | 297 - 333 (Note) |

2. For more detailed information on results, see footnote [3].

Chemical analysis:



NB: Carbon Black is the high quality, reinforcing filler. Ash contains CaCO_3 , the non-reinforcing white filler.

The cost of a fender is often reduced by using a higher percentage of recycled rubber, and low cost non-reinforcing white calcium carbonate (CaCO_3) fillers in the formulation. We found that fenders with recycled rubber and filler are heavier (and denser) than virgin rubber fenders. This significant weight difference enables a user to evaluate whether a fender uses low cost recycled materials, or is the genuine article, made with high performance rubber compound, with the benefits of long life and superior resilience. Chemical and physical analyses revealed some further interesting insights into the materials used for manufacturing the fenders, and the properties these materials have:

- Values of tensile strength and elongation at break for the low cost fender were lower than the high quality fender and not in compliance with the user specification.
- Rubber to filler ratio (Polymer %: Carbon Black % + Ash %) for the high quality fender was 1.23. This simply means 1 kg of filler was blended with 1.23 kg of rubber. The rubber to filler ratio for low cost fender was only 0.88, which means 1 kg of filler was blended with just 0.88 kg of rubber.
- The low cost fender contained 28.45% less rubber than high quality fenders. The presence of more rubber in high quality fenders explains the reason behind better physical properties of these fenders, and also justifies the higher cost. For perspective, the cost of rubber is usually three times higher than fillers like carbon black.

- Most of the raw rubbers are weak when vulcanized and need reinforcing filler to increase mechanical properties of the final product. Ash analysis of the high quality fender indicated that it contains 100% carbon black filler which is high quality reinforcing filler.
- On the other hand, the ash analysis result of the low cost fender showed presence of only 55% carbon black and 45% CaCO₃. The price of CaCO₃ is approximately a fifth cheaper than carbon black. CaCO₃ is considered as white, non-reinforcing filler which is usually used to reduce the cost of the rubber compound but does not help in improving the properties.
- The density of low cost fender is 12% higher than the high quality fender. The reason behind the higher density of the low cost fender could be attributed to the following two factors:
 - The presence of high density CaCO₃ in the formula at 15.54%, as determined by ash analysis. Note that density of CaCO₃ is 2.7 g/cc while that of Carbon black is 1.8g/cc.
 - The presence of a high percentage of recycled rubber in the formulation is the other contributing factor. The density of recycled rubber is 1.15 to 1.20 g/cc while that of virgin rubber is 0.92 g/cc.

Recycling of rubber is a hard line, energy intensive process in which rubber powder is cooked with aggressive chemicals. This process breaks long rubber molecules into shorter ones and thereby reduces the physical properties. Usually tensile strength of recycled rubber is one-third of virgin Natural rubber (NR). Chemical analysis showed that the low cost fender contained 60% NR. However, the low tensile strength, elongation at break and high density of the fender pointed towards the presence of high percentage of recycled rubber instead of virgin rubber.

4. conclusion

These newly developed physical and chemical tests provide a reliable, viable analytical method which can now be made available for buyers to be able to assess the composition of recently procured fenders prior to delivery, using a simple sampling procedure from the surface of the fender. This new technique will help to ensure that fenders supplied use the correct quality of rubber compound required to adhere to the specification. The recommended tests to evaluate the quality of fenders, based on a sample of only 20-50grams are listed in the table below. These samples can be easily gathered by obtaining scrapings from the final product prior to installation, without affecting the fenders performance during application.

| Test | Standard | Specification |
|----------------|------------|---------------|
| Density | ISO 2781 | Max 1.20 g/cc |
| Polymer % | ASTM D6370 | Min. 45% |
| Carbon Black % | ASTM D6370 | Min 30% |
| Ash % | ASTM D297 | Max 5% |

Chemical testing is not enough the guarantee fender performance and full scale testing should also be performed in the factory to guarantee the lifecycle and performance of fenders meet the specification they are intended for. As demonstrated, manufacturers with in house design and engineering capabilities are able to test their compounds in the laboratory and provide full scale testing on prototypes and finished products. It's therefore imperative that port owners and specifies understand the importance of not making procurement decisions purely based on up-front costs.

The equipment will need to be replaced earlier, and in the long term, require heavier investment, not to mention the higher risks of failure during service life. Decision makers should be aware of these key differences and the varying quality on offer when buying on the basis of short term cost savings. There is a need for the whole industry to come together to discuss changes to a culture that is causing unprecedented levels of downtime and putting ports at risk.

5. Reference and footnotes

[1]. Analytical equipment like TGA/FTIR are not usually used in testing for the fender industry for quality control checks, but were applicable in this case to enable chemical analysis of the rubber compounds.

TGA: Thermogravimetric Analysis measures the amount and rate of change in the weight of a material as a function of temperature or time in a controlled environment. Measurements are used primarily to determine the composition and predict thermal stability at temperatures up to 1000°C. The technique can characterize substances that exhibit weight loss or gain due to decomposition, oxidation or dehydration.

FTIR: Fourier Transform Infrared Spectroscopy is most useful for identifying chemicals that are either organic or inorganic in nature. It can be utilized to quantify some components of an unknown mixture. It can be applied to the analysis of solids, liquids and gases. The term Fourier Transform Infrared Spectroscopy refers to a fairly recent development of the manner in which the data is collected and converted from an interference pattern to a spectrum. Today's FTIR instruments are computerized which makes them faster and more sensitive and accurate for composition analysis.

NB: TGA/FTIR are unable to differentiate between virgin and recycled rubber generated from natural rubber.

- [2]. It is assumed that tensile strength and elongation at break of samples prepared from cured product will be 5-15% lower than samples prepared in the laboratory by moulding of uncured rubber
- [3]. Specification: Tensile Strength Min 16Mpa, Elongation at break 350% min. (Ref: Physical Testing of Rubber by Roger Brown, Chapter 3, page 47). The values reported were median of five reading. Tensile strength 16mpa min, E@B 350% min when tested in the compound. These values are lower when tested in the sample taken from final produce (fender). 20192

Mr Kousik Kumar Mishra is currently working with Trelleborg, a Sweden based company and market leader in non-tyre industrial products, since 2001. Mishra was responsible for the Technical development of Marine fenders, Mining products and general purpose & special purpose industrial goods for Trelleborg Singapore, China & Australia manufacturing units. Currently He is working as Global Technical and Market Support Manager for Trelleborg Marine Systems and supporting technical and sales team globally in fender business.

With more than 15 years of experience in the rubber industry, Mishra has presented technical papers in various international conferences. Mishra holds a B.Tech in Rubber Technology from University of Calcutta, M.Sc (Tech) from UDCT, Mumbai University and an Executive MBA from the Chicago Booth School of Science.



LMS Technologies is a leading distributor of Scientific Instruments for Material Science and Polymer Technology in S.E.A region representing highly-acclaimed ThermoFisher Haake and Shimadzu range of products.

Tel : +65 64511123
Fax : +65 64521011
Email : info@lmstech.com.sg
www.lmsscientific.com

 **SHIMADZU**
Excellence in Science

First-class universal testing machines to meet R&D requirements in the development of safer and higher quality materials and products. Combined with a wide selection of accessories, including grips, precision extensometers, environmental chambers, and advance TrapeziumX testing software; Shimadzu UTM systems offers comprehensive solutions that meets international test standards.



Thermo Fisher
S C I E N T I F I C

Parallel Process 11 co-rotating extruder for R&D in the polymer and food industry. The small amount of material needed to conduct experiments enables the researcher to carry out an array of trials in a cost and labor effective manner and obtain results that are relevant to production conditions

Copolymerizations Studied with MALDI ToF MS

Alex van Herk

Institute of Chemical and Engineering Sciences
1 Pesek Road, Jurong Island Singapore, 627833
Email: alexander_herk@ices.a-star.edu.sg

Abstract A reliable method based on a single MALDI-ToF-MS spectrum of the copolymers was applied to determine reactivity ratios. Since MALDI-ToF-MS gives information on individual polymer chains, access to homo-propagation and cross-propagation probabilities becomes available. These probabilities provide the reactivity ratios by simulation of a first order Markov chain by using the Monte Carlo method. The experimental results of random copolymers of P(styrene-co-butylacrylate) was reported. The reactivity ratio of styrene and butylacrylate was calculated as 0.79 and 0.21 respectively.

Keywords: *Copolymers; MALDI-ToF-MS spectrum; reactivity ratio.*

1. Introduction

One of the ultimate challenges in polymer chemistry is the ability to control the physical properties of a copolymer by tailoring its microstructure. Knowing the reactivity ratio of the comonomers allows predicting and tuning of the copolymer's microstructure, both with respect to composition and topology. The classical method to ascertain reactivity ratios is by determining the comonomer composition of a range of polymers prepared with different feed compositions. A fast and reliable method that can prevent this tedious and time-consuming laboratory work is therefore highly desired. Various methods to determine reactivity ratios have been reported which deal with either the differential or the integral form of the Mayo-Lewis equation [1]. Nevertheless, most methods have the disadvantage that still quite some reactions have to be performed with different feed compositions. Moreover, comparison of ratios obtained by diverse methods often shows a relatively big variety due to a statistical error by for example linearization of the equations and absence of weighing the individual data. Choosing the right statistical method is therefore crucial for the reliability of the outcome [2].

Since a copolymer is a statistical mixture of individual molecules, a copolymer sample obtained from a single experiment in principle contains all the information required to retrieve the reactivity ratios. Still, examples of methods that only require a single experiment are limited. Jaacks introduced a method in which the ratios are determined from a single experiment when one of the two monomers is in large excess [3]. This method is limited to systems in which the reactivity ratios do not have an extreme difference in values [4]. Rudin reported on the use of a single NMR spectrum by using the sequence distribution as determined from the measured diads or triads [5]. However, to obtain a highly resolved spectrum, long measuring times are required and assigning the peaks is not straightforward. In ICES we recently acquired a MALDI-ToF MS and have implemented a new method to obtain information about copolymerizations. Matrix assisted laser desorption/ionization time-of-flight mass spectrometry (MALDI-ToF-MS) is a fast and accurate technique to determine copolymer compositions and in principle should be suitable to rapidly determine reactivity ratios of comonomers. The principle of MALDI ToF MS is that polymer chains are brought into flight in a mass spectrometer by using a matrix material for the sample that easily evaporates when illuminated by a laser beam and with it, it brings the polymer chains into flight. A salt is added to bring the polymer a charge.

Recently, we have reported on the use of MALDI-ToF-MS to determine polymer topologies and to study mechanistic aspects of various copolymerization systems [6,7]. The first to apply MALDI-ToF-MS to determine reactivity ratios of comonomers were Suddaby and Willemse but they still required data from different reactions [8,9].

In this study we are going to apply a reliable method to determine reactivity ratios based on a single MALDI-ToF-MS spectrum of the copolymers. Since MALDI-ToF-MS gives information on individual polymer chains, access to homo-propagation and cross-propagation probabilities becomes available [10]. These probabilities provide the reactivity ratios by simulation of a first order Markov chain by using the Monte Carlo method. The reactivity ratios have been determined with this new method successfully for three different types of copolymerizations *i.e.* free radical polymerization, ring-opening polymerization of cyclic esters and of oxiranes and anhydrides [11].

2. Methodology and Results

MALDI-ToF-MS spectra give highly accurate molar masses of all the polymer chains in the sample which not only enables elucidation of individual chain lengths, but provides full characterization including the copolymer's chemical composition and to some extend the copolymer topology (random, gradient, block, alternating). MALDI-ToF-MS spectra can be deconvoluted by employing the equation:

$$m_{cal} = n_1 Mw_1 + m_2 Mw_2 + E_l + E_H + M^+ \quad (1)$$

where E_l and E_H represent the molar masses of the end groups at opposite sides of the chain, $n_1 Mw_1$ and $m_2 Mw_2$ represent the number and molar mass of the repeating units of monomer M_1 and M_2 respectively, and M^+ the mass of the cation (a salt is usually added for charging the polymer chains in order for them to be accelerated in the mass spectrometer). With this equation, a complete matrix with $n_{l,i}$ rows and $m_{2,j}$ columns can be constructed for a given end group combination. (see Figure 1). The peaks in the spectrum are assigned to a certain position in the matrix employing the inequality:

$$|m_{exp} - m_{cal}| \leq \frac{\Delta m}{2} \quad (2)$$

In which m_{exp} represents the experimental mass, m_{cal} the calculated mass and Δm the accuracy ($1-2 \text{ g}\cdot\text{mol}^{-1}$). By calculating the natural abundance isotope distributions for each position in the matrix and rescaling it to the corresponding highest-intensity mass-peak, a full spectrum can be simulated as well as the corresponding contour plot, which provides information about the polymer composition (see Figure 2).

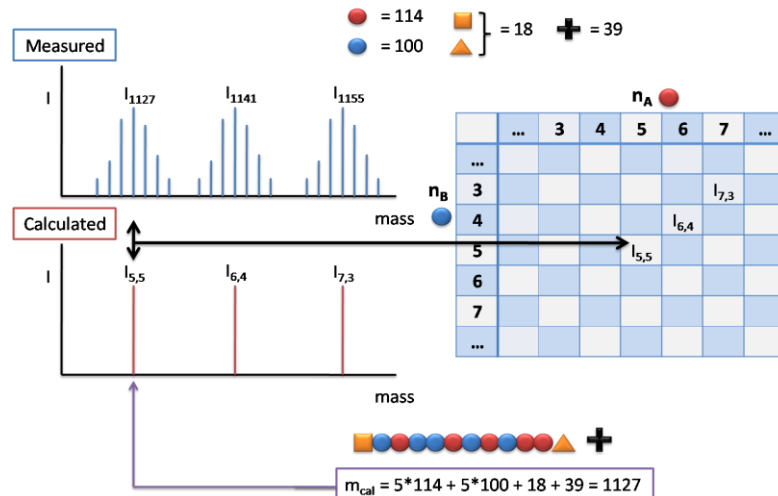


Figure 1. Schematic representation of the matrix of the copolymer.

The chemical composition distributions for the chain lengths covered by the total chain length distribution can be obtained by diagonally walking through the matrix from $(0, M_{1,n})$ to $(M_{2,n}, 0)$ after normalization using the sum of intensities within this chain length. The distribution of monomer repeating units along an individual chain can be

described by a first order Markov chain by means of the Mayo-Lewis (terminal) model [11]. In this study we use the terminal model for copolymers in which we can distinguish the following four probabilities:

$$\begin{array}{ll} \sim M_1^* + M_1 \rightarrow \sim M_1 M_1^* & P_{11} = \frac{r_1(M_1)/(M_2)}{r_1(M_1)/(M_2) + 1} \\ \sim M_1^* + M_2 \rightarrow \sim M_1 M_2^* & P_{12} = \frac{1}{r_1(M_1)/(M_2) + 1} \\ \sim M_2^* + M_2 \rightarrow \sim M_2 M_2^* & P_{22} = \frac{r_2}{(M_1)/(M_2) + r_2} \\ \sim M_2^* + M_1 \rightarrow \sim M_2 M_1^* & P_{21} = \frac{(M_1)/(M_2)}{(M_1)/(M_2) + r_2} \end{array}$$

The reactivity ratios are then given by $r_1 = P_{11}/P_{12} [M_2]/[M_1]$ and $r_2 = P_{22}/P_{21} [M_1]/[M_2]$. The reactivity ratios can be obtained from the MALDI-ToF MS spectrum at one chain length at a time (see slice in Figure 2), also allowing to look for chain length dependent effects, still from one single experiment.

a. 50 STY/50 BA

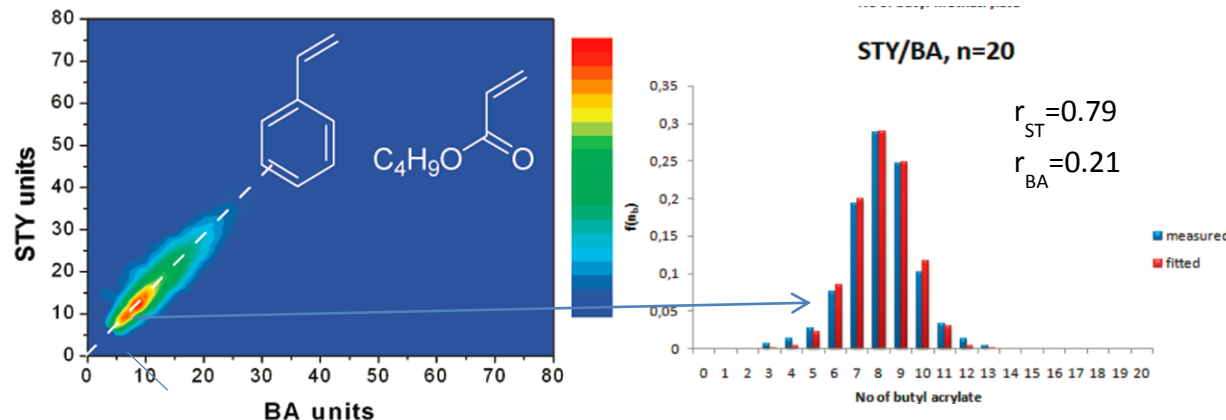


Figure 2: Copolymer matrix for a styrene-butylacrylate copolymer represented in a contour plot and one chemical composition distribution (CCD) at chain length 20 monomer units (right) also showing the fitted CCD resulting in the reactivity ratios for this copolymerization system.

3. Reference

- [1] a) C. Hagiopol, *Copolymerization*, Towards a systematic approach, Springer, **1999**. b) A.L. Polic, T.A. Duever, A. Penlidis, *J. Polym. Sci., Part A: Polym. Chem.* **1998**, 36, 813. c) M. Finemann, S.D. Ross, *J. Polym. Sci.*, **1950**, 5, 259. d) T. Kelen, F. Tüdös, *J. Macromol. Sci., Chemistry*, **1975**, A9, 1.
- [2] a) R. van der Meer, H.N. Linssen, A.L. German, *J. Polym. Sci., Part A: Polym. Chem.* **1978**, 16, 2915. b) A.M. van Herk, T. Dröge (1997) *Macromol. Theory Simul.* **6** 1263-1276. c) A.M. van Herk (1995) *J. Chem. Ed.* **72** 138-140
- [3] V. Jaacks, *Makromol. Chem.* **1972**, 161, 161.
- [4] D. R. Burfield, C. M. Savariar, *J. Polym. Sci., Polym. Lett. Ed.* **1982**, 20, 515.
- [5] A. Rudin, K. F. O'Driscoll, M. S. Rumack, *Polymer* **1981**, 22, 740.
- [6] S. Huijser, B.B.P. Staal, J. Huang, R. Duchateau, C.E. Koning, *Angew. Chem. Int. Ed.* **2006**, 45(25), 4104.
- [7] S. Huijser, B.B.P. Staal, J. Huang, R. Duchateau, C.E. Koning, *Biomacromolecules* **2006**, 7(9), 2465.
- [8] K. G. Suddaby, K. H. Hunt, D. M. Haddleton, *Macromolecules* **1996**, 29, 8642.
- [9] R. X. E. Willemse, A. M. Van Herk, *J. Am. Chem. Soc.* **2006**, 128, 4471.
- [10] M. S. Montaudo, A. Ballistreri, G. Montaudo, *Macromolecules* **1991**, 24, 5051.
- [11] S. Huijser, G.D. Mooiweer, R. van der Hofstad, B.B.P. Staal, J. Feenstra, A.M. van Herk, C.E. Koning, R. Duchateau (2012) *Macromolecules* **45**, 4500-4510

Alex van Herk (1956) is senior researcher at the Institute of Chemical and Engineering Sciences in Singapore since 2012 and part-time professor in Polymer Reaction Engineering at the Eindhoven University of Technology, the Netherlands (where he worked full-time from 1986 till 2012). Since 2009 he also is teaching at NUS regularly. His field of research is nanotechnology, water-based coatings and emulsion polymerization. He is editor of four books and author of 180 papers. At present he is chairman of the Foundation Emulsion Polymerization, a multisponsored liaison program between industry and academia.

Electrode Nanomaterials for Energy Storage and Conversion Applications

H. T. Tan¹, Q. Y. Yan Alex¹, K. H. Ho², H. W. Lee², M. X. Ng², T. A. Ho²

¹School of Material Science and Engineering
Nanyang Technological University

²Diploma in Materials Science
School of Chemical & Life Sciences
Singapore Polytechnic

Abstract Manganese oxide nanoparticles, a pseudocapacitor material, can be synthesised through hydrothermal synthesis to control and produce nanoparticles of desired morphologies. The addition of carbon nanotubes, a good electric conductor, into this synthesis process allows these nanoparticles to be formed on these nanotubes and be embedded within them. This overcomes the poor electrical conductivity limitation of manganese oxide, thus allowing its excellent pseudocapacitance properties to be harnessed. In hope to optimise the pseudocapacitance of this nanocomposite, the nanoparticle crystal structure, morphology and the effects of nanoparticle's morphology on specific capacitance under varying parameters of synthesis time, temperature as well as the volume of potassium permanganate were respectively characterised and studied using X-ray diffraction, scanning electron microscopy and cyclic voltammetry. Post studies show the synthesis of nanoparticles with flower, hexagonal plates and nanorods morphologies where flowers possess birnessite crystal structure while hexagonal plates and nanorods possess nsutite crystal structure. Optimal specific capacitance was shown to be achieved at 160°C, 120 minutes and using 2mL of 0.25M potassium permanganate where the highest specific capacitance obtained was 335F/g.

Keywords: Manganese oxide nanoparticles; carbon nanotubes; pseudocapacitance; morphology; specific capacitance.

1. Introduction

Environmental issues and depleting fossil fuels have sparked interest in the research and development of alternative energy storage/conversion devices in recent years. Supercapacitors, or electrochemical capacitors, have received enormous attention owing to their potential applications ranging from mobile devices to electric vehicles. Supercapacitors are broadly classified into double-layer capacitors and pseudocapacitors with each having different mechanisms of energy storage. Double-layer capacitors store energy via non-Faradic accumulation of charges at the electrolyte-electrode interface while pseudocapacitors store charges by undergoing Faradic reactions which involve the transfer of electrons [4]. Pseudocapacitors display higher specific capacitance over double-layer capacitors and thus, various transition metal oxides have been investigated as potential pseudocapacitor materials [3].

Out of the various oxides investigated, hydrated ruthenium oxide ($\text{RuO}_2 \cdot n\text{H}_2\text{O}$) was reported to have specific capacitances of up to 700F/g [4]. However, the use of ruthenium oxide is limited by its high cost, toxicity, and the required use of highly acidic electrolytes to obtain peak performance. On the other hand, manganese oxide (MnO_2) nanoparticles (NPs) which have the advantages of low synthesis cost, abundance, non-toxicity and ability to perform well in neutral electrolyte systems, has recently garnered attention as a promising pseudocapacitor material. Although hydrated MnO_2 has a theoretical specific capacitance value of 1370 F/g, it has been experimentally reported to exhibit specific capacitances within 100 – 200 F/g which is far from the theoretical value of 1370 F/g owing to its poor electrical conductivity [6].

MnO_2 can be synthesised using different techniques, such as simple reduction, sol-gel, co-precipitation and in particular, hydrothermal synthesis. Hydrothermal synthesis was found to be a good technique in the preparation of nanomaterials with different morphologies such as wires, rods, urchins and belts. The main advantages of hydrothermal synthesis over the other synthesis routes are its ability to have good control over the morphologies of the nanoparticles formed as well as environmental benign since water is used as the solvent. Each nanostructure has its own advantages when used in potential applications. In the synthesis of MnO_2 NPs, it was observed that the NPs could take up 3 different morphologies which are highly relevant to the discussion of this study [6]. The NPs would initially aggregate to form spherical flower agglomerates which with prolonged durations and specific conditions of ageing, would gradually transform into nanorods. This transformation was due to the fact that the high specific surface areas of nanospheres/nanoflowers led to high surface energies, and thus they would aggregate further to

form structures such as nanorods as they are more stable and have lower surface energies. This transformation is consistent with the Ostwald Ripening process which stated that larger particles with lesser surface energy form at the expense of smaller particles with greater surface energy. The third morphology observed was hexagonal plates morphology and this morphology was regarded as an intermediate of the transformation from nanoflowers to nanorods. Hexagonal plates appeared due to insufficient time and temperature for the transformation to occur completely. Thus, it could be deduced that nanoflowers have the highest surface energies, followed by the hexagonal plates, and then nanorods. Generally, nanoflowers are desired as it has higher surface area available for surface faradic reaction than hexagonal plates and nanorods morphology which therefore allow higher pseudocapacitance to be obtained.

There has been an increasing use of carbon additives, such as carbon nanofoams, graphenes and CNTs, during the synthesis of MnO_2 NPs to overcome its poor electrical conductivity and improve its performance as a supercapacitor. Due to their high electrical conductivity, such carbon additives are added to facilitate electron transport to the MnO_2 NPs during Faradic reactions.

This study aims to deduce the optimum synthesis of MnO_2 -CNT composite with the highest specific capacitance. MnO_2 was synthesised onto functionalised multi-wall CNTs through hydrothermal synthesis with different reaction conditions, namely synthesis time, synthesis temperature, and the volume of potassium permanganate (KMnO_4) used for the synthesis. The effects of the reaction parameters on the morphology, the crystal structure of the morphology produced and morphology on specific capacitance of the MnO_2 -CNT composite are studied and discussed.

2. Experimental

2.1 Preparation of Hydrothermal Synthesis

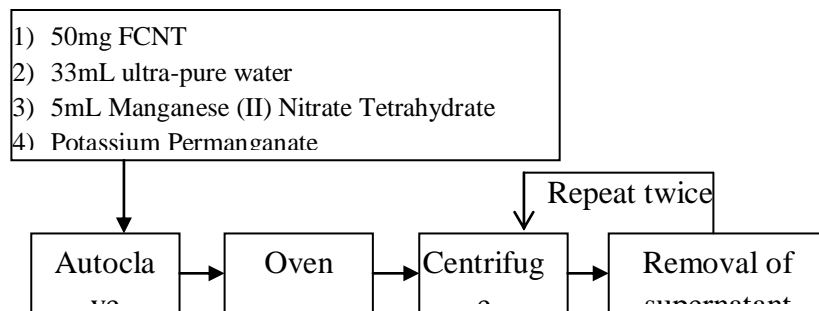


Figure 2.1.1: Hydrothermal synthesis procedure

Table 2.1.2: Samples and their respective parameters

| Parameter 1: Volume of 0.25M KMnO_4 (mL) | Parameter 2: Temperature (°C) | Parameter 3: Time (Min) | | |
|---|-------------------------------|-------------------------|-----|-----|
| | | 45 | 120 | 180 |
| | | 120 | A1 | A2 |
| 0.4 | 120 | 160 | A4 | A5 |
| | | 200 | A7 | A8 |
| | | 120 | B1 | B2 |
| | 160 | 160 | B4 | B5 |
| | | 200 | B7 | B8 |
| | | 120 | C1 | C2 |
| | 160 | 160 | C4 | C5 |
| | | 200 | C7 | C8 |
| | | 200 | | C9 |

50mg of FCNT and 5mL of 1% w/v aqueous manganese (II) nitrate tetrahydrate were added into an autoclave's Teflon capsule. After which the desired volume of the variable 0.25M KMnO_4 were added before adding ultra pure water till the solution reaches 50ml in total. The resulting solution is then sonicated for 5mins. The autoclave with its

Teflon capsule inside was subsequently placed and heated in an oven at the desired temperature and duration. Next, the synthesised mixture was transferred into a centrifuge tube and subjected to centrifugation. After the first cycle ends, the supernatant was removed and the centrifuge tube was topped up with ultra pure water till the solution reaches 50ml before the next centrifugation. Another 2 cycles of centrifugation, refilling of ultra-pure water and removal of supernatant were carried out in order to remove reactants from the sample. This procedure as illustrated in figure 2.1.1 is repeated for all the 36 samples with their respective parameter as listed below in table 2.1.2.

2.2 Scanning Electron Microscope (SEM) analysis

The centrifuge tube containing our sample was topped up with ultra-pure water before ultra-sonicating the solution. A micropipette was used to draw small amount of sample from the test tube and dropped on the shiny surface of silicon wafer. The silicon wafer was dried in an oven at 70°C before inserting into JEOL JSM-7600F FE-SEM for viewing of the sample's NPs' morphology. This procedure was repeated for each sample.

2.3 Cyclic Voltammetry (CV) test

A mortar was used to grind 12mg of sample and 1.5mg of carbon black for 10 minutes. A slurry was obtained by adding 3 drops of NMP and 25mg of 5% w/w PVDF in NMP solution into the grinded sample. A dry 1cm X 1cm carbon paper was weighed and the slurry was applied evenly on the surface of the weighed carbon paper and dried under vacuum in a vacuum oven at 40°C overnight to remove the NMP solvent and trapped air. The dried carbon paper was weighed to obtain the mass of sample applied onto it. It was then set up as a working electrode, along with a platinum wire counter electrode, and a silver chloride reference electrode. CV was then conducted using Solartron Analytical Model 1470E with the following scan rates: 5, 10, 20, 40, 80, 100, 200, 500 and 1000mV.s⁻¹ and potential window of -0.5 to 1.5V. From the obtained voltammogram, the area within the graph is calculated using software and the specific capacitance is calculated with the equation shown in figure 2.3.1. This procedure was repeated for each sample.

$$\frac{\text{Area within the voltammogram graph}}{\text{Mass of sample} \times \text{scan rate}} = \text{Specific capacitance}$$

Figure 2.3.1: Equation for calculating specific capacitance

2.4 X-ray Diffraction (XRD) test

Some amount of a sample was powdered with a mortar and transferred onto the centre of a specimen holder and was subsequently pressed down using a glass slide to flatten the sample. The specimen holder was then transferred into the specimen stage of Shimadzu LabX XRD-6000 X-ray Diffractometer and the test was carried out using a pre-set programme.

3. Results and discussions

3.1 Morphology

When the samples were viewed under SEM, we observed various morphologies which are recorded in table 3.1.1. In total, 3 morphologies of manganese oxide NPs were obtained and they are flower, hexagonal plate and nanorods which can be illustrated in figure 3.1.2.

3.2.1 Time effect

From the morphologies obtained in our sample, it was observed that as synthesis time increases, the favoured morphology shifts from flower to hexagonal plates followed by nanorods. Based on the observations recorded in table 3.1.1, part of this trend can be observed from sample B1 to B6 and C1 to C6. Flower and hexagonal plate NPs were observed at 45mins synthesis with flower morphology being most prominent. However as synthesis time increases, only hexagonal plate morphologies were observed. Another part of this trend can be observed in samples from C7 to C9 where both flower and hexagonal plates NPs were observed in 45mins synthesis time but at higher synthesis time, flower morphology were no longer observed while nanorods morphologies were observed instead.

However, this trend could not be observed from samples ranging A1 to A9 which was synthesised using 0.4ml of 0.25M KMnO₄ and from samples from B7 to B9 which have common parameters of 200°C and 1ml of 0.25M

KMnO_4 . This could be due to the smaller amount of 0.25M KMnO_4 used and the applied synthesis temperature parameter having a more dominant effect over the time parameter thus preventing this trend from expressing.

Table 3.1.1: Morphologies of NPs observed in samples with varying synthesis time, temperature and volume of 0.25M KMnO_4

| | | | Parameter 1: Time (Min) | | |
|---|---|-----|---|--|--|
| | | | 45 | 120 | 180 |
| Parameter 3: Volume of 0.25M KMnO_4 (mL) | Parameter 2: Temperature ($^{\circ}\text{C}$) | 0.4 | Sample A1; Hexagonal plate morphology. | Sample A2: No visible NPs. | Sample A3; Hexagonal plate morphology. |
| | | 1 | Sample A4; Hexagonal plate morphology. | Sample A5; Hexagonal plate morphology. | Sample A6; Hexagonal plate morphology. |
| | | 2 | Sample A7: No visible NPs. | Sample A8: No visible NPs. | Sample A9; Hexagonal plate morphology. |
| Parameter 3: Volume of 0.25M KMnO_4 (mL) | Parameter 2: Temperature ($^{\circ}\text{C}$) | 0.4 | Sample B1: Mixed presence of flower and hexagonal plate morphology. | Sample B2: Hexagonal plate morphology. | Sample B3: Hexagonal plate morphology. |
| | | 1 | Sample B4: Mixed presence of flower and hexagonal plate morphology. | Sample B5: Hexagonal plate morphology. | Sample B6: Hexagonal plate morphology. |
| | | 2 | Sample B7: Hexagonal plate morphology. | Sample B8: Hexagonal plate morphology. | Sample B9: Hexagonal plate morphology. |
| Parameter 3: Volume of 0.25M KMnO_4 (mL) | Parameter 2: Temperature ($^{\circ}\text{C}$) | 0.4 | Sample C1; Flower morphology. | Sample C2: Hexagonal plate morphology. | Sample C3: Hexagonal plate morphology. |
| | | 1 | Sample C4: Flower morphology with minor presence of hexagonal plate. | Sample C5: Hexagonal plate morphology. | Sample C6: Hexagonal plate morphology. |
| | | 2 | Sample C7: Mixed presence of flower and hexagonal plate morphology. | Sample C8: Mixed presence of hexagonal plate & nanorods morphology. | Sample C9: Mixed presence of hexagonal plate & nanorods morphology. |

3.1.2 Temperature effect

It was observed that an increasing synthesis temperature results in a similar trend where the favoured type of morphology shifts from flower to hexagonal plates followed by nanorods. This could be observed from sample B1, B4, B7, C1, C4 and C7. Flower morphology were prominent at lower synthesis temperatures but as synthesis temperature increases towards 200°C, hexagonal plates morphology was observed to have higher prominence than flower. From sample C2, C5, C8, C3, C6 and C9, it was observed that at lower synthesis temperatures of 120°C and 160°C, only hexagonal plate morphology were found. However at 200°C, nanorods were observed also. This trend was not observed in other samples. This may also probably due to the other parameters having a more dominant effect over the temperature parameter which as a result prevented this trend from expressing.

3.1.3 Effect of volume of 0.25M KMnO_4

The volume of KMnO_4 used was observed to affect the morphology of NPs as well. An increase in the volume of KMnO_4 used was observed to lead to flower and nanorods morphologies. This can be observed in samples A1, B1, C1, A4, B4, C4, A7, B7 and C7 where the morphology of the greatest prominence shifts from hexagonal plates to flower morphology with increasing volume of KMnO_4 . Samples A8, B8, C8, A9, B9 and C9 on the other hand shows that with increasing volume of KMnO_4 the morphology of the greatest prominence shifts from hexagonal plates to nanorods morphology. Similarly as previously discussed parameters, the possibility of a dominant effect of other parameters could have prevented other samples from expressing these trends. It has been noted that only at 0.4ml of 0.25M of KMnO_4 , some samples were observed to be absent of NPs. As KMnO_4 is the precursor to MnO_2 , the low

amount of KMnO_4 used may have resulted in low yield of MnO_2 which could be too low for significant precipitation of MnO_2 to form NPs.

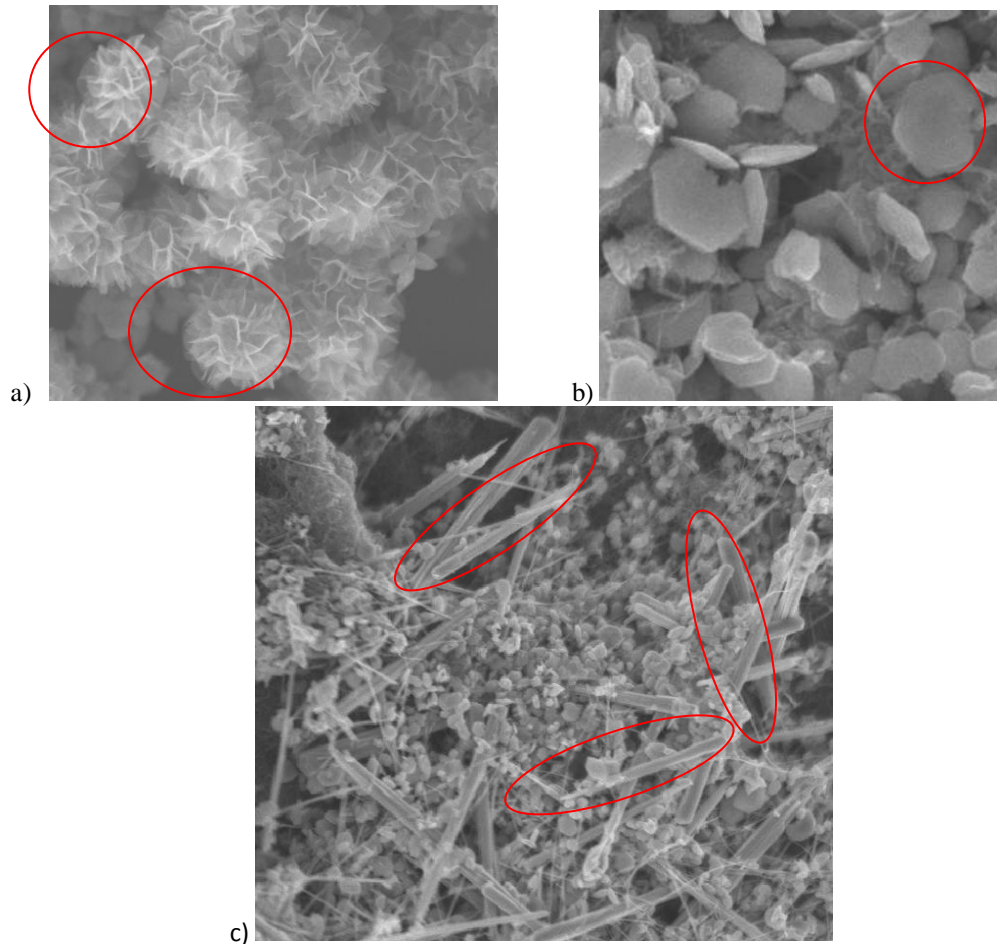


Figure 3.1.2: a) Flower morphology MnO_2 NP b) Hexagonal plate morphology MnO_4 NP c) Nanorods Morphology MnO_2 Nanoparticle NP

3.1.4 Discussion:

Comparing to other literature such as one by Suh et al., they reported that an elevated temperature and longer synthesis time favoured the growth of nanorods morphologies over the flower morphologies [5]. In another study conducted by Subramanian et al. it was also found that with increasing synthesis time the flower NPs forms into hexagonal plate NPs first before subsequently forming nanorods NPs [4]. These findings are consistent with our results however the difference in our results is the additional presences of hexagonal plates morphology which suggest that the morphological transformations of our NPs in most of our sample were incomplete since hexagonal plate morphologies were found to be intermediates of the transformation from flower to nanorods morphologies. For how morphologies are affected by concentration of reactants used, we are at the moment unable to find any similar studies for comparison as our project may be one of the first to conduct morphology studies using this parameter.

It is known that pseudocapacitance is proportional to the surface area of NPs and surface area of flower morphology is the highest followed by hexagonal plate morphology and subsequently nanorods. It thus can be deduced that decreasing temperature and time could lead to pseudocapacitors with higher specific capacitance as flower morphology is favoured with these parameters.

3.2 Cyclic voltammetry test

Each sample was tested with different scan rate: 5, 10, 20, 40, 80, 100, 200, 500 and 1000mV.s⁻¹. The specific capacitance results obtained for each sample are shown in table 3.2.1. For this discussion, results obtained from 40mV.s⁻¹ scan rate have been selected for discussion and comparison.

Using statistics, we identified the range in which the specific capacitance results are not considered an outlier.

Median of data: 171.25

1st Quartile: 129.44; 2nd Quartile: 219.75

Interquartile range: 219.75 – 129.44 = 90.31

$$219.75 + 90.31 \times 1.5 = 355.215; \text{ and } 129.44 - 90.31 \times 1.5 = -6.025$$

Table 3.2.1: Sample's specific capacitance (F/g)

| Parameter 1: Volume of 0.25M KMnO₄ (mL) | Parameter 2: Temperature (°C) | Parameter 3: Time (Min) | | |
|---|--|--------------------------------|---------------------|---------------------|
| | | 45 | 120 | 180 |
| 0.4 | 120 | A1 162.20 | A2 128.32 | A3 277.07 |
| | 160 | A4 207.36 | A5 219.75 | A6 169.57 |
| | 200 | A7 468.36 | A8 114.56 | A9 151.51 |
| | 120 | B1 212.31 | B2 129.44 | B3 140.01 |
| | 160 | B4 159.34 | B5 174.17 | B6 171.25 |
| | 200 | B7 121.94 | B8 209.97 | B9 114.16 |
| 2 | 120 | C1 187.97 | C2 99.23 | C3 80.45 |
| | 160 | C4 244.39 | C5 334.60 | C6 275.36 |
| | 200 | C7 170.21 | C8 323.17 | C9 184.57 |

Thus the range of specific capacitance in which the result is acceptable is 0 to 355.215F/g. Therefore sample A7 with 468.36 F/g is an outlier data and will be discussed separately from other samples. Based on the CV results obtained, outlier sample A7 produced the highest specific capacitance of 468.36 F/g. However, the SEM images of this sample as shown in figure 3.2.2 did not show any presence of NP.

This observation of achieving very high specific capacitance despite absence of NPs in SEM images may be a result of non-uniform distribution of NPs throughout the sample as shown by the two red circles in figure 3.2.3 where one circle has NP present while the other have none. Thus for that sample, the specimen sent for CV test may have a large amount of NPs present while the specimen sent for SEM analysis may have extremely low amount NPs found on it. Therefore more tests have to be carried out in future to investigate this anomaly.

From table 3.2.1 there are no observable trends as to how different parameters affect the specific capacitance of the produced pseudocapacitor material. However from the results it was observed that samples with higher specific capacitance are most frequently produced when using 120 mins synthesis time or 160°C synthesis temperature or 2ml of 0.25M of KMnO₄. This could help in understanding the optimum conditions to synthesise manganese oxide NPs with optimum specific capacitance.

Based on the results in table 3.2.4, there is no observable trend which suggests that the NP's morphology plays a part in the specific capacitance. The lowest and highest specific capacitances were obtained by samples with hexagonal plate morphology. Furthermore, samples with nanorods morphology managed to exhibit higher specific capacitance than samples with flower morphologies. This is unexpected as it is theoretically expected that flower morphologies with higher surface area would exhibit higher specific capacitance. Furthermore, many journals during literature review also indicated that flower morphologies would exhibit higher specific capacitance.

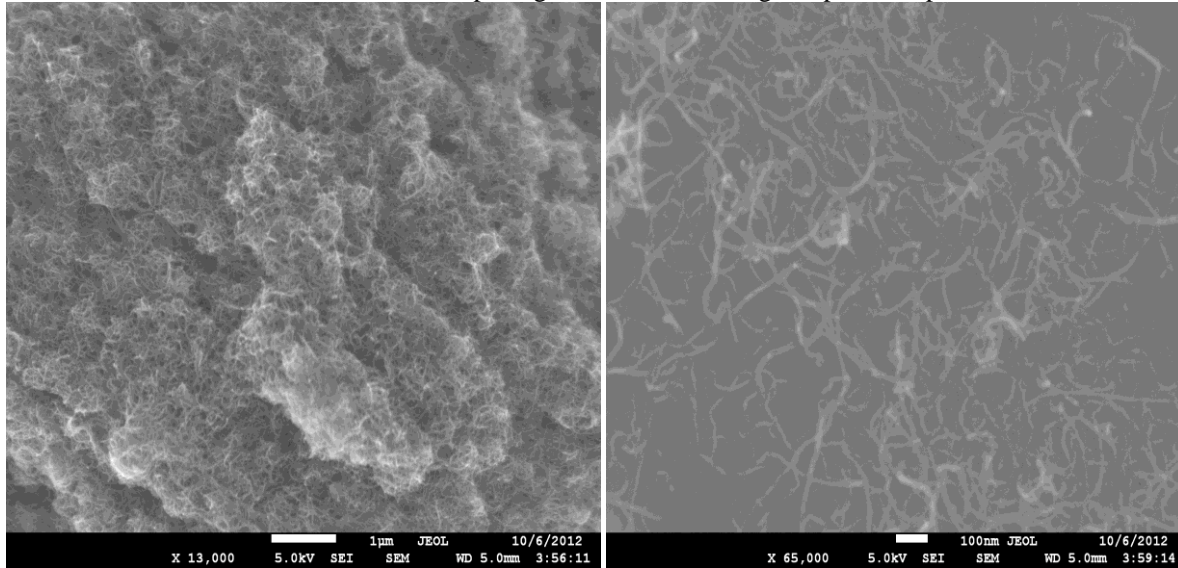


Figure 3.2.2: SEM images of outlier sample

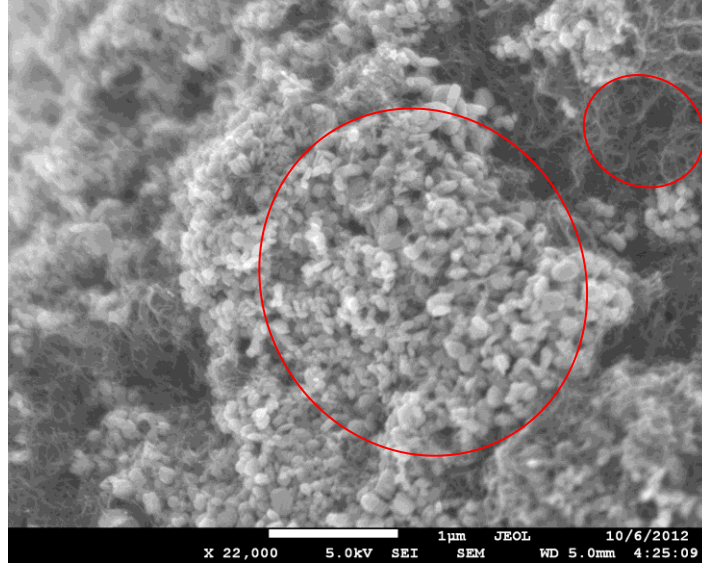


Figure 3.2.3 SEM image showing non uniform distribution

Table 3.2.4: Range of specific capacitance achieved by various morphologies

| Morphology | Range of specific capacitance (F/g) |
|------------------|-------------------------------------|
| Flower | 170.21 – 212.31 |
| Hexagonal plates | 80.45 – 334.60 |
| Nanorods | 184.57 – 323.17 |

A possibility as to why hexagonal plates and nanorods morphology achieved better specific capacitance than flower morphology despite theory and journals supporting flower as the morphology that would achieve superior

specific capacitance; may be due to the fact that embedment and amount of NPs produced playing a significant role in determining the resulting specific capacitance.

3.3 X-ray diffraction test

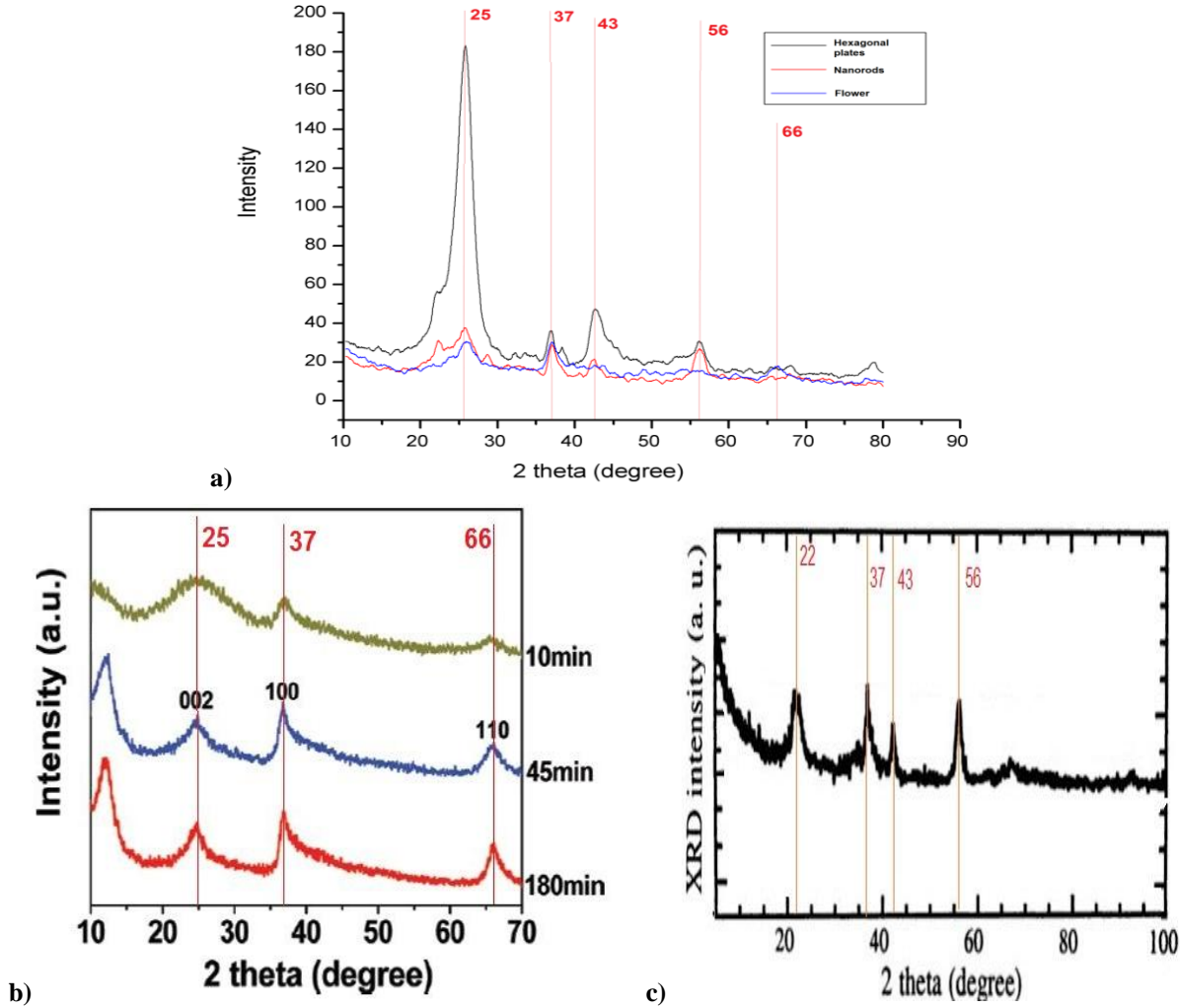


Figure 3.3.1: a) XRD graph of the various morphologies in our samples b) XRD graphs of birnessite MnO_2 ; c) XRD graphs of nsutite MnO_2

By comparing the flower morphology XRD data with the birnessite crystal structure XRD data recorded by Zhu et al. in figure 3.3.1, it is found that MnO_2 in NPs with flower morphology are arranged in birnessite crystal structure as they have common peaks at 25° , 37° and 66° [7]. On the other hand, by comparing the hexagonal plates and nanorods morphology XRD data with the nsutite crystal structure XRD data recorded by Julien and Massot in figure 3.3.1, it is found that MnO_2 in NPs with the hexagonal plates and nanorods morphology are arranged in birnessite crystal structure as they have common peaks at $\sim 25^\circ$, 37° , 43° and 56° [2].

Birnessite, in theory and from various literature exhibits superior capacitance over nsutite crystal structure as the crystal structure of birnessite has better ion-exchange, adsorption, intercalation and higher surface area available on the crystal. But as discussed in cyclic voltammetry section under effects of NP's morphology on specific capacitance, it was found that flower morphology achieved the lowest specific capacitance compared to nanorods and hexagonal plate morphologies. This may be due to other possible factors such as amount of NP present and degree of embedment which may have a significant or dominant effect over that of crystal structure.

4. Conclusions

In our search of optimising the specific capacitance of MnO_2 -CNT nanocomposite, success was made in producing MnO_2 nanoparticles with flower, hexagonal plates and nanorods morphologies for our studies. Through XRD, flower morphology was found to possess birnessite crystal structure while hexagonal plates and nanorods morphologies were found to possess nsutite crystal structure. By comparing results between the different parameters used and the morphologies observed, it was observed that as synthesis temperature and time increases the favoured morphology shifts from flower to hexagonal plates to nanorods while with increasing volume of KMnO_4 used, it was observed to lead to flower and nanorods morphologies. It was expected that samples with flower morphology NPs would achieve higher specific capacitance as it possess a higher surface area and a birnessite crystal structure but results from CV tests show otherwise.

It was therefore hypothesised that there may be other factors such as degree of NPs embedment and amount of NPs synthesised that may have a more dominant influence on the specific capacitance of the MnO_2 -CNT nanocomposite and thus further investigation into other possible factors should be carried it out. Last but not least a discovery that may potentially make progress in our goal to optimise the specific capacitance of MnO_2 -CNT nanocomposite, it was observed that higher specific capacitance was frequently shown to be achieved at 160°C or 120 minutes or using 2mL of 0.25M potassium permanganate where the highest specific capacitance obtained was 335F/g.

5. References

- [1] Cottineau T., Toupin M., Delahaye T., Brousse T., Belanger D.: Nanostructured transition metal oxides for aqueous hybrid electrochemical supercapacitors. *Applied Physics A*, 82, 599-606 (2006).
- [2] Julien C. M., Massot M.: Vibrational Spectroscopy of Electrode Materials for Rechargeable Lithium Batteries III. Oxide Frameworks. *Proceedings of the International Workshop "Advanced Techniques for Energy Sources Investigation and Testing"*, (2004).
- [3] Raymundo-Piñero E., Khomenko V., Frackowiak E., Beguin F.: Performance of Manganese Oxide/CNTs Composites as Electrode Materials for Electrochemical Capacitors. *The Electrochemical Society*, 152, A229-A235 (2005).
- [4] Subramanian V., Zhu H., Vajtai R., Ajayan P. M., Wei B.: Hydrothermal Synthesis and Pseudocapacitance Properties of MnO_2 Nanostructures. *Journal of Physical Chemistry*, 109, 20207-20214 (2005).
- [5] Suh C. P., Suk F. C., Chian Y. L.: Controlled Synthesis of Manganese Dioxide Nanostructures via a Facile Hydrothermal Route. *Journal of Nanomaterials*, 2012, (2012).
- [6] Wei W., Cui X., Chen W., Ivey D. G.: Manganese oxide-based materials as electrochemical supercapacitor electrodes. *Chemistry Society Review*, 40, 1697-1721 (2011).
- [7] Zhu J., Shi W., Ni X., Rui X., Tan H., Lu X., Huey H. H., Ma J., Yan Q.: Oxidation-Etching Preparation of MnO_2 Tubular Nanostructures for High-Performance Supercapacitors. *American Chemical Society Applied Materials Interfaces*, 4, 2769-2774 (2012).

Mr. Ho Thiam Aik is currently working in the Singapore Polytechnic, Department of Student Development and Alumni Relations as Alumni Manager. Prior that, he has 17 years of teaching experience in the School of Chemical and Life Sciences. His basic degree was in Materials Engineering from Nanyang Technological University, and he obtained his MSc in Environmental Safety and Health from National University of Singapore. His areas of specialization include Corrosion Science, Analytical Chemistry and Workplace Safety and Health.

Synthesis and Characterisation of Anode Nanomaterials for Lithium Ion Batteries

H. T. Tan¹, Q. Y. Yan Alex¹, Y. Y. Kee², Z. W. Chan², C. S. Leow Kevin² and T. A. Ho²

¹School of Material Science and Engineering
Nanyang Technological University

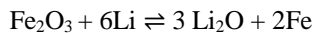
²Diploma in Materials Science
School of Chemical & Life Sciences
Singapore Polytechnic

Abstract Iron (III) oxide nanoparticles are prospective alternative anode materials for lithium ion batteries owing to their higher theoretical capacity, excellent corrosion resistance and eco-friendly nature. Hydrothermal synthesis using solution-based reactions will be applied to produce well-controlled size, morphology and composition iron oxide nanoparticles. In order to discover the optimum conditions in which the best electrochemical performance can be obtained, the nanoparticle morphology, size, crystal structure, and corrosion rate under varying parameters of synthesis time, temperature as well as the concentration of iron source were analysed and studied respectively using scanning electron microscopy, X-ray diffraction, cyclic voltammetry and electrochemical impedance spectroscopy. According to the experimental results, it was found that the sample with optimum parameter was synthesised at 120°C for 4 hours using 1 mmol of iron (III) chloride.

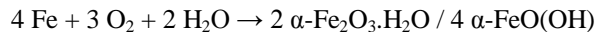
Keywords: Iron (III) oxide nanoparticles; theoretical capacity; corrosion rate; scanning electron microscopy.

1. Introduction

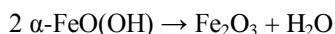
So far, the vast need for long-lasting high capacity batteries still could not be satisfied by current energy storage technology. Studies on nano-structured materials with different morphologies are of great interest in the field of lithium ion batteries because of their higher lithium-ion diffusion coefficients and larger contact area between the electrode and electrolyte [1]. Among all possible anode materials, iron (III) oxide, Fe₂O₃ stands up as one of the safer, abundant, less expensive and higher capacity alternatives. The Fe₂O₃ crystal lattice can store six Li ions per formula unit and its theoretical capacity is as high as 1005 mAh/g, versus 370 mAh/g of the conventional graphite anode [3]. The reversible electrochemical reaction of Fe₂O₃:



In this experiment, iron (III) chloride hexahydrate, FeCl₃.6H₂O reacts with water and oxygen to form iron (III) oxide nanoparticles through hydrothermal synthesis. In the presence of strong acidic solution, hydrochloric acid (HCl), the iron precursors are being hydrolysed and oxidised its oxide derivatives. Due to the hydrated nature of iron (III) chloride, the iron (III) oxide formed is hydrated as well [2].



Hydrated iron (III) oxide or iron (III) oxyhydroxide is also written as $\alpha\text{-FeO(OH)}$. The water content within in the crystal structure of iron (III) oxyhydroxide can be eliminated through dehydration. The most common way is to perform thermal processing called annealing. The temperature required for dehydration to take place above 200°C and it is indicated that $\alpha\text{-FeO(OH)}$ precursors can be completely transformed into hematite at 300°C [3].



When iron (III) ions, Fe³⁺ first reacts with water molecules in solution, six-line ferrihydrite (Fe₅HO₈.4H₂O) nanodots are formed. After that, ferrihydrite (Fe₅HO₈.4H₂O) nanodots are converted to goethite, $\alpha\text{-FeO(OH)}$

nanodots through the hydrolysis process as the hydrothermal reaction goes on. Goethite nanodots aggregated and grew into nanorods through “Ostwald ripening” mechanism [4]. Through annealing, goethite nanorods were sintered at 300°C for 2 hours in air and transformed to mesoporous hematite α -Fe₂O₃ nanorods. The formation of mesopores is due to removal of hydroxide, OH groups when FeO(OH) was transformed to α -Fe₂O₃. These α -Fe₂O₃ nanorods are further transformed into nanospheres which are more stable via “Ostwald ripening” process [4].

2. Experimental

2.1 Preparation of Anode Material via Hydrothermal Synthesis

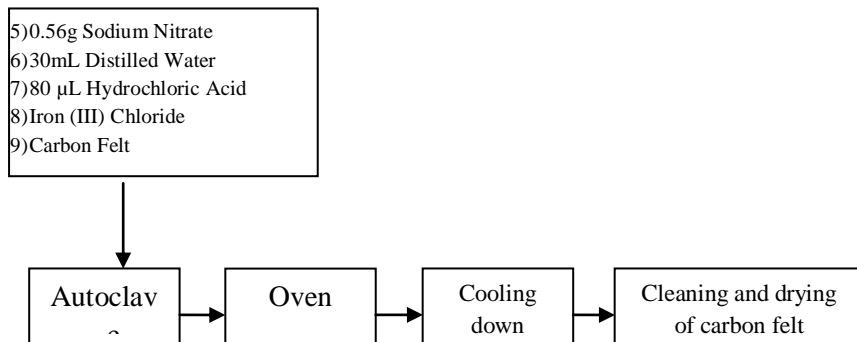


Figure 1: Procedure of Hydrothermal Synthesis

Table 1: Samples and their respective parameters

| Parameter 3: Concentration of Iron (III) Chloride (mmol) | | Parameter 1: Synthesis Time (Hour) | | | |
|--|-----|------------------------------------|---------------|---------------|----------------|
| | | 4 | 5 | 6 | 12 |
| Parameter 2: Synthesis Temperature (°C) | 0.5 | | | | |
| | 1 | 120-III-0.5-4 | 120-III-0.5-5 | 120-III-0.5-6 | 120-III-0.5-12 |
| | 1.5 | 150-III-0.5-4 | 150-III-0.5-5 | 150-III-0.5-6 | 150-III-0.5-12 |
| Parameter 2: Synthesis Temperature (°C) | 0.5 | 100-III-1-4 | 100-III-1-5 | 100-III-1-6 | 100-III-1-12 |
| | 1 | 120-III-1-4 | 120-III-1-5 | 120-III-1-6 | 120-III-1-12 |
| | 1.5 | 150-III-1-4 | 150-III-1-5 | 150-III-1-6 | 150-III-1-12 |
| Parameter 2: Synthesis Temperature (°C) | 0.5 | | | | |
| | 1 | 120-III-1.5-4 | 120-III-1.5-5 | 120-III-1.5-6 | 120-III-1.5-12 |
| | 1.5 | | | | |

Desired concentration of variable iron (III) chloride and 0.56g (1 mmole) of sodium nitrate were dissolved in 30 mL of distilled water inside an autoclave's Teflon capsule followed by addition of 80 μ L of hydrochloric acid. After several minutes of ultrasonic dispersing, a carbon felt, which acts as current collector was fully dipped into the solution. The autoclave with its Teflon capsule inside was then subsequently placed and heated in an oven at the desired temperature and time. After cooling down for 2 hours, the carbon felt was taken out from the solution, washed carefully with distilled water, and eventually dried at 70°C overnight in the oven. This procedure as illustrated in Figure 1 is repeated for all the 28 samples with their corresponding parameter.

2.2 Annealing

The as-prepared sample was calcined in a quartz tube at 400°C for 2 hours with a heating rate of 10°C min⁻¹ in Ar atmosphere.

2.3 Sample Characterizations

JOEL JSM-7600F scanning electron microscope was employed to examine the morphology of the sample. The crystal structure phases of the samples were characterised by Shimadzu X-ray diffraction (Cu-K α , $\lambda = 1.5406 \text{ \AA}$) from 5° to 80° at a step size of 0.02 s⁻¹.

2.3 Electrochemical Measurements

To test the anode performance of synthesised materials, CR 2025 coin cells were made using Celgard 2400 as the separator and the electrolyte was 1 M LiPF₆ in 1:1 mixture of ethylene carbonate and diethyl carbonate. The coin cells were assembled inside an argon-filled glove box with oxygen and water contents below 1 and 0.1 ppm, respectively. Li-metal was used as the counter and reference electrode. The working electrode was fabricated by the active material (iron oxide) on the carbon felt. Galvanostatic charging and discharging tests were conducted using a battery tester (1470E Eight Channel Potentiostat/Galvanostat) at different current densities at room temperature. Cyclic voltammetry was performed using an electrochemical workstation (CHI 660C) from 1 mV to 3 V at a scanning rate of 0.2 mV s⁻¹. Electrochemical impedance spectroscopy was carried out at the scan mode of 10 mV s⁻¹.

3. Results and Discussions

3.1 Scanning Electron Microscopy

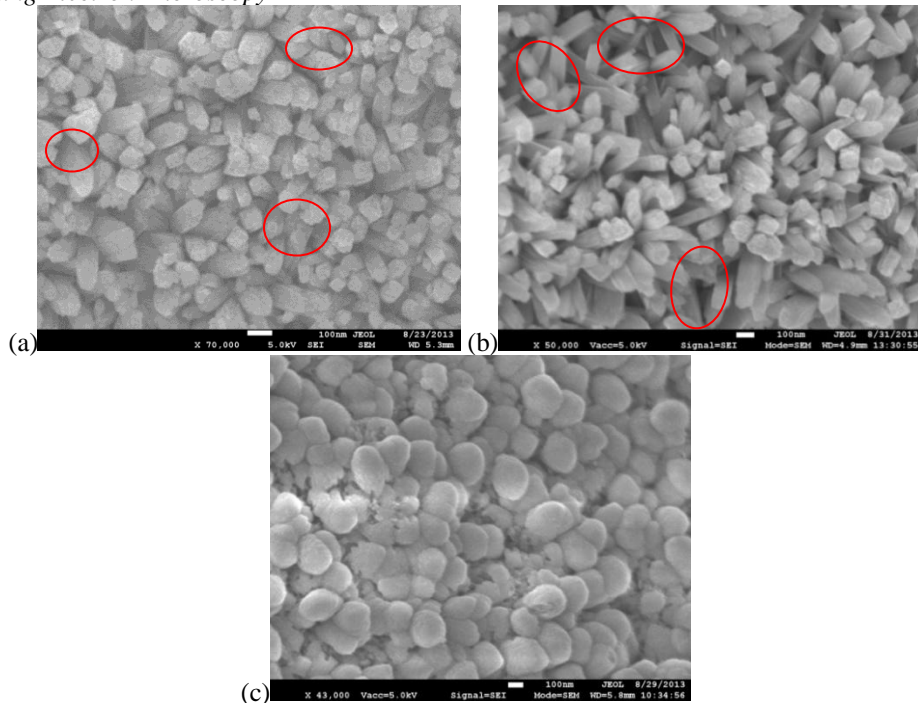


Figure 2: (a) *Nanodots morphology NPs (b) Nanorods morphology NPs; (c) Nanospheres morphology NPs

Table 2: Morphologies of NPs observed in samples with varying synthesis time, temperature and concentration of iron (III) chloride

| Samples | NPs' Morphology |
|----------------|----------------------------------|
| 100-III-1-4 | Nanorods & Nanodots |
| 100-III-1-5 | Nanospheres |
| 100-III-1-6 | Nanospheres |
| 100-III-1-12 | Nanospheres |
| 120-III-0.5-3 | Nanorods & Nanodots |
| 120-III-0.5-4 | Nanorods & Nanodots |
| 120-III-0.5-5 | Nanospheres |
| 120-III-0.5-6 | Nanospheres |
| 120-III-0.5-12 | Nanospheres |
| 120-III-1-3 | Nanorods & Nanodots |
| 120-III-1-4 | Nanorods |
| 120-III-1-5 | Nanorods, Nanodots & Nanospheres |
| 120-III-1-6 | Nanospheres |
| 120-III-1-12 | Nanospheres |
| 120-III-1.5-3 | Nanorods & Nanodots |
| 120-III-1.5-4 | Nanorods |
| 120-III-1.5-5 | Nanorods, Nanodots & Nanospheres |
| 120-III-1.5-6 | Nanorods & Nanospheres |
| 120-III-1.5-12 | Nanospheres |
| 150-III-0.5-4 | Nanorods & Nanodots |
| 150-III-0.5-5 | Nanospheres |
| 150-III-0.5-6 | Nanospheres |
| 150-III-0.5-12 | Nanospheres |
| 150-III-1-3 | Nanorods & Nanodots |
| 150-III-1-4 | Nanorods & Nanodots |
| 150-III-1-5 | Nanorods, Nanodots & Nanospheres |
| 150-III-1-6 | Nanorods & Nanospheres |
| 150-III-1-12 | Nanospheres |

*For simplicity purpose, we classified them as “nanodots”. To be more precise, they should be termed as nanorods with shorter length, or nanorods with lower aspect ratio.

3.1.1 Morphology

Through SEM analysis, iron oxide nanoparticles (NPs) of three morphologies were being produced. These morphologies include *nanodots, nanorods and nanospheres which are illustrated in Figure 2 and summarised in Table 2.

3.1.2 Size/Dimension

Table 3: Dimension range of NPs observed in samples with varying synthesis time, temperature and concentration of iron (III) chloride

| Samples | NPs' Dimension Range (nm) |
|----------------|---------------------------|
| 100-III-1-4 | Small & Medium-sized NPs |
| 100-III-1-5 | Small & Medium-sized NPs |
| 100-III-1-6 | Medium-sized & Large NPs |
| 100-III-1-12 | Medium-sized & Large NPs |
| 120-III-0.5-3 | Small NPs |
| 120-III-0.5-4 | Small NPs |
| 120-III-0.5-5 | Small NPs |
| 120-III-0.5-6 | Small & Medium-sized NPs |
| 120-III-0.5-12 | Medium-sized NPs |
| 120-III-1-3 | Small NPs |
| 120-III-1-4 | Small NPs |
| 120-III-1-5 | Small & Medium-sized NPs |
| 120-III-1-6 | Medium-sized & Large NPs |
| 120-III-1-12 | Medium-sized & Large NPs |
| 120-III-1.5-3 | Small NPs |
| 120-III-1.5-4 | Small & Medium-sized NPs |
| 120-III-1.5-5 | Medium-sized NPs |
| 120-III-1.5-6 | Medium-sized & Large NPs |
| 120-III-1.5-12 | Large NPs |
| 150-III-0.5-4 | Small NPs |
| 150-III-0.5-5 | Small & Medium-sized NPs |
| 150-III-0.5-6 | Medium-sized & Large NPs |
| 150-III-0.5-12 | Large NPs |
| 150-III-1-3 | Small NPs |
| Samples | NPs' Dimension Range (nm) |
| 150-III-1-4 | Small & Medium-sized NPs |
| 150-III-1-5 | Medium-sized & Large NPs |
| 150-III-1-6 | Medium-sized & Large NPs |
| 150-III-1-12 | Large NPs |

The size of iron oxide NPs formed was categorized into three ranges: small NPs (<200nm), medium-sized NPs (200-400nm) and large NPs (>400nm). The estimated size range of NPs was determined by measuring the largest as well as the smallest NPs in an SEM image in the aids of dimension scale shown at the bottom of image. For nanorods, the length was taken into account. On the other hand, nanodots and nanospheres were measured in the aspect of diameter. Refer to Table 3 below.

In conclusion, the iron oxide NPs with nanorod morphology and within a size range of 200nm or less are preferable in terms of electrochemical performance. These NPs possess the largest possible surface area for simultaneous lithium ion insertion provided the volume of NPs is the same. Large surface area of NPs permits:

- i. A high contact area with the electrolyte and hence a high lithium-ion flux across the interface.
- ii. Shorter distance for lithium-ion transport within the particles.

Due to these reasons, anode with smaller NPs tends to conduct a higher capacity when compared to NPs with NPs of larger dimension.

3.1.3. Parameters' Effects on NPs

3.1.3.1 Synthesis Time

From the SEM images, it was observed that a shorter synthesis time results in the formation of rod-like and polygonal NPs. As the synthesis time increases, NPs formed are typically found in spherical structure. The trend where a shorter synthesis time led to nanorods and polygonal NPs can be observed from the samples which were produced at a synthesis time of 4 hours or less. The presence of nanorods and irregular NPs was clearly visible in SEM images of these 10 samples while spherical NPs were not noticeable.

Spherical NPs started to appear on the samples when the synthesis time increased to 5 hours. In contrast, polygonal NPs were hardly found or totally vanished in these samples. As the synthesis time increased from this point to 6 hours, the amount of spherical NPs increased and nanorods were getting lesser. When the synthesis time was raised to 12 hours, all of the samples were entirely composed of spherical NPs. It can be seen that a short synthesis time led to the formation of favourable nanorod morphology.

Generally, the dimension of NPs formed increased proportionally with the increase in synthesis time. This trend can be well observed from parameters set: 150-III-1-3, 150-III-1-4, 150-III-1-5, 150-III-1-6 and 150-III-1-12. At constant temperature, types and concentration of iron chloride, the NPs were growing larger when the synthesis time increased. On the sample 150-III-1-3, NPs were formed in a range of 50-150 nm. In contrast, the NPs on the sample 150-III-1-12 were oversized in terms of nanoscale, whereby the range was 500-1300 nm. It can be seen that decreased synthesis time caused smaller NPs of desirable scale to be formed.

3.1.3.2 Synthesis Temperature

According to SEM images, there was no observable trend stating at different temperature, NPs of different morphologies were synthesized. An increasing temperature led to a higher retention of nanorods and polygonal NPs after longer synthesis time. This was deduced by comparing the sample products of 1mmol iron chloride at different temperatures. After processing at temperature of 100°C, nanorods can only be found on the sample experiencing 4 hours synthesis time. The rest was merely consisted of spherical NPs. When the processing temperature increased to 120°C, nanorods were observed on 4-hour and 5-hour samples. This structure of NPs existed on 4-hour, 5hour and 6-hour sample when the temperature further rose to 150°C. it was found that an increase in temperature resulted in higher nanorods formation possibility.

It was inferred that the dimension growth of NPs was accelerated when the temperature rose. This trend can be observed from the change in NPs size of 0.5mmol iron chloride samples. At 120°C, the NPs formed on the anode samples were either considered small or medium-sized, with dimension up to 400nm. Only small NPs were observed on 3-hour, 4-hour and 5-hour samples and no large NPs exceeding 400nm was found on 12-hour sample. On the other hand, medium-sized NPs were observed from 5-hour sample when it went through a processing temperature of 150°C. Furthermore, large NPs which have size of 400nm and above started to be formed on 6-hour sample. However, this trend was not observed when other parameters were used. This may due to more dominating effect of synthesis time and iron chloride concentration over the temperature parameter which as a result prevented this trend from being significantly observed. It was found that dimension of NPs decreased at lower synthesis temperature.

3.1.4 Concentration of Iron (III) Chloride

3.1.4.1 Concentration effect on Morphology

There was no trend showing NPs of different morphologies were produced when concentration of iron chloride varied. According to the SEM images, it was discovered that at higher FeCl_3 concentration, the nanorod NPs stood a greater chance to be fabricated. This was clearly showed by comparing the morphology of NPs formed on the basis of varying FeCl_3 concentration. When 0.5mmol of FeCl_3 was used, nanorod NPs were only presented on the 3 hours and 4 hours samples. In contrast, upon the addition of 1.5mmol of FeCl_3 , nanorod NPs were found on the samples with synthesis time of 3 to 6 hours. It can be seen that nanorod NPs were more likely to be produced at a higher iron (III) chloride concentration.

3.1.4.2 Concentration effect on Dimension

Similarly, iron chloride concentration did not alter the size of NPs drastically. Nevertheless, it was observed that NPs enlarged faster when iron chloride concentration increased. When 0.5mmol of iron chloride was added to undergo 3 and 4 hours synthesis process, the NPs formed on the anode possessed dimension of lower than 200nm. On the other hand, medium-sized NPs where the dimension range is 200-400nm started to be formed on 4-hour-samples when iron chloride concentration was 1.0mmol and 1.5mmol. It was found that NPs were growing smaller at a faster rate when iron (III) chloride concentration decreased.

Table 4: Variables requirement to obtain NPs of desirable morphology and size

| Variables | Desirable Morphology (Nanorods) | Desirable Size (Small: <200nm) |
|-----------------------------------|------------------------------------|-----------------------------------|
| Synthesis Time | Short | Short |
| Synthesis Temperature | High | Low |
| Iron (III) Chloride Concentration | High | Low |

From Table 4 as shown above, it can be discovered that a short synthesis time of 4 hours or less is desirable. 4 hours synthesis time was chosen over 3 hours as the optimum condition because the previous “trial” synthesis by using iron (II) chloride at 3 hours produced samples which exhibited an undesirable NPs morphology.

On the other hand, the other two variables: synthesis temperature and iron (III) chloride concentration yielded contradict results on morphology and dimension. After further discussion with supervisor, we decided to select “mid-range” of each of these variables as optimum conditions to strike a balance between morphology and dimension. Hence, a synthesis temperature of 120°C (instead of 100°C and 150°C) and an iron (III) chloride concentration of 1mmol (instead of 0.5mmol and 1.5mmol) were chosen as optimum. With these optimum formulations chosen, desired nanorods with dimension of within 200nm are able to be produced.

3.1.5 Annealing

Sample synthesised at optimum formulation was annealing under a condition of 400°C for 2 hours and the outcome was then examined via SEM. For the SEM images (Figure 3), it was ascertained that the size of NPs on the annealed sample were slightly reduced to 50-200nm while the morphology of NPs still retained. It was found that annealing enhances the dimension of NPs without changing their morphology.

As shown In Figure 4(b), all the diffraction peaks of sample 120-III-1-4 can be indexed to the orthorhombic iron oxide hydrate ($\text{Fe}_2\text{O}_3 \cdot \text{H}_2\text{O}$). In addition, the distinct broad peak at $\sim 26^\circ$ indicated the carbon material. Studies revealed that water content tends to react with lithium and thus, affecting the capacity of the battery. So, we decided to anneal the sample as to remove the water content in crystal lattice completely. After annealing, it can be observed that the characteristic peaks became sharper (smaller full width of half maximum (FWHM) than the $\text{Fe}_2\text{O}_3 \cdot \text{H}_2\text{O}$), indicating that the crystallinity of the annealed sample was enhanced significantly (Figure 5). Diffraction peaks emerged at 33.1° , 35.6° , 40.8° , 49.5° , 54.1° , 57.6° , 62.4° and 64.0° can be indexed to the (104), (110), (113), (024), (116), (018), (214) and (300) crystal planes of commercial rhombohedral hematite ($\alpha\text{-Fe}_2\text{O}_3$), demonstrating the probability of transforming the hydrated form of Fe_2O_3 to its pure phase. Again, the distinct peak at $\sim 26^\circ$ is indicative of the carbon material.

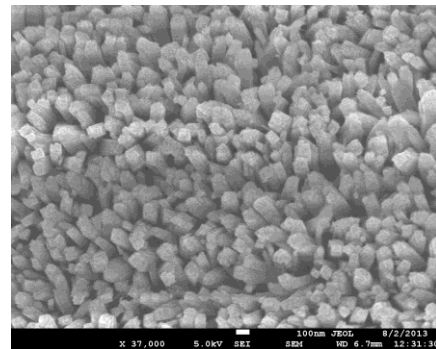


Figure 3: SEM image of the annealed sample

3.2 X-ray Diffraction (XRD) Analysis

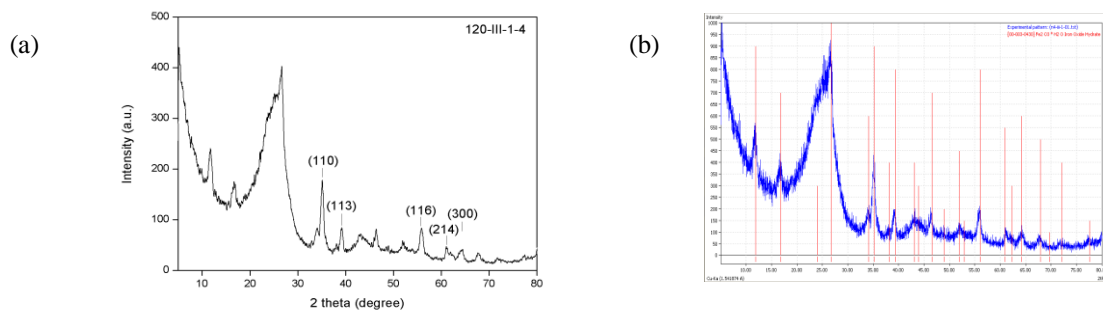


Figure 4: (a) XRD pattern of sample 120-III-1-4 (b) “Matching” with XRD analysis software

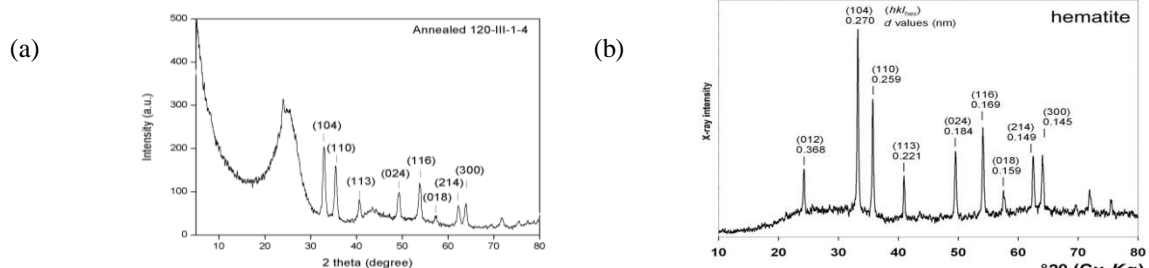


Figure 5: (a) XRD pattern of sample 120-III-1-4 after annealing (b) XRD pattern of commercial hematite sample

3.3 Cyclic Voltammetry (CV) Test

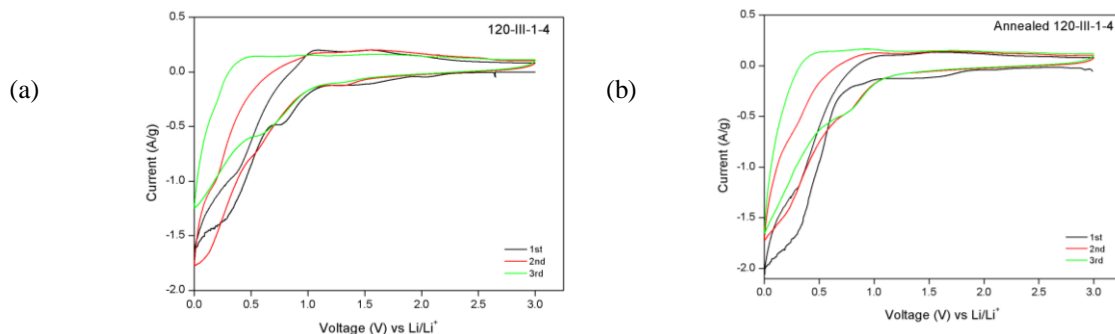


Figure 6: (a) Cyclic voltammogram curves of sample 120-III-1-4 (b) Cyclic voltammogram curves of sample 120-III-1-4 after annealing

Figure 6(a) shows the CV curves of sample 120-III-1-4 in the first three cycles in the voltage range from 3 to 0.001 V at a scan rate of 0.2 mV s⁻¹. From the CV curves, cathodic peaks located at 2.1 V and 1.58 V could be attributed to the intercalation of lithium before the reduction of iron oxide NPs. These two peaks disappeared in the subsequently cycles, indicating their irreversibility in nature. In addition, a peak located at 0.83 V represent the conversion of Fe³⁺ to Fe²⁺ and continue reduction of Fe²⁺ to Fe⁰. In the anodic scan, the oxidation peaks at 1.1 and 1.58 V correspond to the oxidation of Fe⁰ to Fe²⁺ and Fe²⁺ to Fe₂O₃, respectively. The presented peaks match the theory of reduction and oxidation peaks of the iron oxide versus lithium reported in the literature. However, in the following second and third cycles, the cathodic peak and anodic peaks with reduced peaks intensity become indistinguishable. The reason is the certain irreversibility of the redox reactions during charging and discharging. Figure 6(b) demonstrates the CV curves of the annealed sample 120-III-1-4. It shows similar voltage locations of cathodic and anodic peaks with sample 120-III-1-4 because the annealing process only removes the crystalline water from the iron-oxide NPs but does not change its phase. Hence, the cathodic and anodic peaks are remaining at the same voltage point.

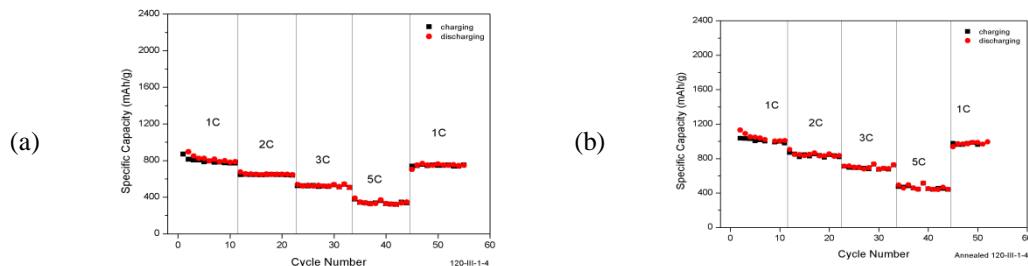


Figure 7: (a) Cycling performance chart of sample 120-III-1-4 (b) Cycling performance chart of sample 120-III-1-4 after annealing

The cycling performance chart 7(a) is obtained from the sample of 120-III-1-4 at 1 C. The sample show initial discharge specific capacities of 869, 813 and 805 mAh/g, and decreases to 754mAh/g at the 55th cycle at a low current density of 1 C. After 55 cycles, the capacity of the coin cell is still able to maintain 87% of its original capacity. It is considered as good and stable performance.

$$\begin{aligned} \text{\% of retained capacity after 55th cycles} &= \frac{\text{Capacity}_{55}}{\text{Capacity}_1} \times 100\% \\ &= \frac{754}{869} \times 100\% \\ &= 87\% \end{aligned}$$

Under low current density charging and discharging, the cyclic performances show a good stability up to 60 cycles which maintain the specific capacity around 800mAh/g. The SEM results revealed that the nanorods structure of the iron oxide NPs was the main reason that caused the excellent stability of the coin cell. The underlying reason is because of the high surface area of the active materials for lithium ions intercalation. On the other hand, long reaction time tends to cause the hydrothermal synthesis form bigger particles in sphere structure which can be observed from SEM results. The formations of large sphere particles greatly affect the capacity and stability performance of the coin cell.

When the current rate is increased from 1 C to 5 C with 1 C interval value, there is a decreasing value of discharge-charge specific capacities as show in the figures above. There were 11 charging-discharging cycles at each different current density for the coin cell testing. Hence, there are a total of at least 55 cycles for the sample. The higher current density used for measurement will decrease the specific capacity of the cell because the rate of conversion reaction (iron oxide NPs) occurs at the electrode is not able to keep pace with the charge/discharge rate. In this scenario, the capacity contributed from the redox reaction of the active materials becomes the determining factor that limits the specific capacity of a coin cell.

The sample exhibits excellent cycling stability because of nano-dimension of hydrated Fe₂O₃ nanorods that give rises to specific surface area. In order to obtain better rate performance, annealing process was conducted to

remove all the water molecules within the crystal lattice without sacrificing their uniformity and initial morphology. Figure 7(b) shows 55 cycles cycling performance chart of annealed 120-III-1-4 sample. After annealing, the sample was carried out CV test with the same parameters and conditions. The discharge specific capacities of the samples in the first 3 cycles are 1183, 1111, and 1093 mAh/g. At the 55th cycle, the annealed sample gives a discharge specific capacity of 1010 mAh/g which retains 85% of its original specific capacity.

$$\begin{aligned} \text{\% of retained capacity after 55th cycles} &= \frac{\text{Capacity}_{55}}{\text{Capacity}_1} \times 100\% \\ &= \frac{1010}{1183} \times 100\% \\ &= 85\% \end{aligned}$$

From the preliminary results and analyses, the annealed product gives an improved performance in term of higher specific capacity and good charging-discharging coin cell stability.

3.4 Electrochemical Impedance Spectroscopy (EIS)

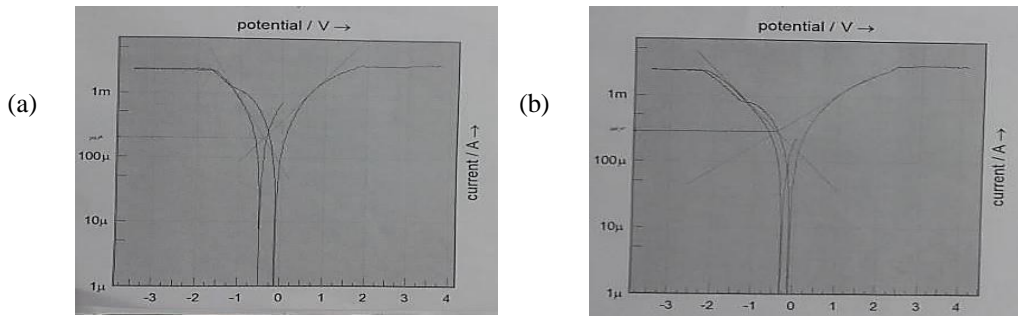


Figure 8: (a) EIS result of sample 120-III-1-4 (b) EIS result of conventional coin cell

Due to time constraint, we only managed to investigate the corrosion rate of battery produced from the optimum formulation (120-III-1-4). The annealed sample is still undergoing CV test which required longer testing time. However, we believed that annealed sample should be able to give greater corrosion resistance as the water molecules in the crystal lattice can be removed completely by means of annealing. Conventional graphite anode material plays the role of reference during this EIS test for comparison purpose. Based on the EIS results, the optimised battery has an average corrosion rate of **7 mm/yr** and conventional lithium ion battery shows a higher average corrosion rate of **10 mm/yr**. These corrosion rate results may seem high because we are simulating the worst case scenario whereby the whole battery is completely immersed in tap water

$$\text{Corrosion Rate} = K \cdot \frac{a \cdot i_{corr}}{n \cdot D}$$

- a : atomic weight
- i_{corr} : corrosion current density, $\mu\text{A}/\text{mm}^2$
- n : number of electrons lost (valency change)
- D : density, g/cm^3
- K : a constant depending on the unit of corrosion rate

| Unit of Corrosion Rate | K Value |
|-------------------------|---------|
| mpy | 0.129 |
| $\mu\text{m}/\text{yr}$ | 3.27 |
| Mm/yr | 0.00327 |

The values of parameters are as below:

$$K = 0.00327 \text{ mm/yr} \quad D = 2.7 \text{ g/cm}^3 \quad n = 3$$

$$a = 27 \text{ g/mol} \quad \text{Area of coin cell} = 314.16 \text{ mm}^2$$

Figure 9: Equation for calculating corrosion rate

Current density of samples, μA :

| | 1 | 2 |
|--------------------------------------|-------------------|-------------------|
| Hydrated Fe_2O_3 NPs | 200 μA | 180 μA |
| Graphite | 300 μA | 250 μA |

i_{corr} of samples:

| | 1 | 2 |
|--------------------------------------|---------------------------------|---------------------------------|
| Hydrated Fe_2O_3 NPs | 0.637 $\mu\text{A}/\text{mm}^2$ | 0.573 $\mu\text{A}/\text{mm}^2$ |
| Graphite | 0.955 $\mu\text{A}/\text{mm}^2$ | 0.796 $\mu\text{A}/\text{mm}^2$ |

Corrosion rate:

| | 1 | 2 | Average |
|--------------------------------------|-------------|------------|----------|
| Hydrated Fe_2O_3 NPs | 6.94 mm/yr | 6.25 mm/yr | 7 mm/yr |
| Graphite | 10.41 mm/yr | 8.68 mm/yr | 10 mm/yr |

The main reason of hydrated Fe_2O_3 NPs has a lower corrosion rate is due to the formation of protective passivation layer. The layer protects the anode from reacting with the surrounding oxygen. On the other hand, graphite anode is reactive and it tends to form a weak, unstable porous layer, known as solid electrolyte interphase (SEI). During charging and discharging, the SEI will partially dissolve into the electrolyte which causes the corrosion of anode and reduction of insertion places for electron ions. Hence, the corrosion rate of LIB using graphite anode is greater.

4. Conclusion

In our approach to synthesise a ‘greener’ anode material for battery, it was observed that the optimised sample was made by using 120°C, Fe (III) as iron source, 1 mmol of iron source, and 4 hours. The optimised anode sample demonstrated the following properties:

- i. The sample, 120-III-1-4 has a hydrated hematite crystal structure, $(\text{Fe}_2\text{O}_3 \cdot \text{H}_2\text{O})$.
- ii. The formation of hydrated hematite crystal structure, $(\text{Fe}_2\text{O}_3 \cdot \text{H}_2\text{O})$ is arranged in nanorods morphology which can perform excellent cycle and rate performance as the long nanorods could ensure many fast and convenient electron transport pathway, thus enhancing the electronic conductivity leading to improved electrochemical performance of higher specific capacity and good charging-discharging stability. The in-situ growth of $\text{Fe}_2\text{O}_3 \cdot \text{H}_2\text{O}$ on carbon felt could ensure fast electron transport pathway between the active materials and the current collector, leading to improved electrochemical performance.
- iii. The corrosion rate of Fe_2O_3 NPs is lower as compared to graphite anode material used in conventional LIB.

Furthermore, it was found that the water content in the crystal lattice can be removed completely by means of annealing at 400°C for 2 hours under argon atmosphere. This demonstrates the probability of transforming the hydrated form of Fe_2O_3 to its pure phase. The annealed sample improves crystallinity of iron oxide nanoparticles which leads to enhance the overall electrochemical performance of battery in term of rate performance and capacity.

5. References

- [1] Bruce, P. G., Scrosati, B. and Tarascon, J. 2008. Nanomaterials for Rechargeable Lithium Batteries. *Angew. Chem. Int. Ed.*, (47), pp. 2930-2946. Available from: doi: 10.1002/anie.200702505.
- [2] Mohammed M. Rahman, Sher Bahadar Khan, Aslam Jamal, Mohd Faisal and Abdullah M. Aisiri (2011). Iron Oxide Nanoparticles, Nanomaterials, Prof. Mohammed Rahman (Ed.), ISBN: 978-953-307-913-4, InTech, Available from: <http://www.intechopen.com/books/nanomaterials/iron-oxide-nanoparticles>
- [3] Wang, J., Li, L., Chui, L. W., Sun, L., Shen, Z. and Madhavi, S. 2013. Controlled synthesis of a-FeOOH nanorods and their transformation to mesoporous a- Fe_2O_3 , $\text{Fe}_3\text{O}_4 @ \text{C}$ nanorods as anodes for lithium ion batteries. *RSC Advances*, (3), pp. 15316-15326. Available from: doi: 10.1039/c3ra41886c.
- [4] PSS Particle Sizing Systems. 2012. *Ostwald Ripening*. [online] Available at: <http://pssnicomp.com/definitions/ostwald-ripening/>

Tin-lead Alloy/Carbon Polymeric Composites with High Electrical Conductivity

Yongzheng Pan*

Institute of Materials Research and Engineering (IMRE),
Agency for Science, Technology and Research (A*STAR),
3 Research Link, 11760, Republic of Singapore
E-mail: pany@imre.a-star.edu.sg

Abstract: Tin-lead alloy (Sn-Pb) featured with a wide melting range was used to prepare polymeric composites. Sn-Pb/polypropylene (PP) composites and Sn-Pb/conductive carbon/PP (Sn-Pb/Carbon/PP) composites were fabricated through melt mixing. Sn-Pb (20/80) and Sn-Pb (40/60) were used to study the impact of Sn-Pb component and processing temperature on electrical conductivity of Sn-Pb/PP composites. It was found that both of them had significant effect on the achievement of high electrical conductivity. Based on the results of the effect of molding temperature on electrical conductivity, it was proved that the viscosity of Sn-Pb particles at the mixing temperature was the key issue to form long-range conducting paths. This approach was applied in preparation of Sn-Pb (20/80)/Carbon/PP composites with high electrical conductivity. Two conductive carbons used were carbon black (CCB) and carbon nanotubes (CNTs). Those ternary composites were high electrically conductive and injection moldable. The conductivity of Sn-Pb/CNT/PP achieved $10 \text{ S}\cdot\text{cm}^{-1}$ with 14 vol.-% of Sn-Pb and it was 25 vol.-% for Sn-Pb/CCB/PP composites. The current FreedomCAR target for bipolar plates of $100 \text{ S}\cdot\text{cm}^{-1}$ was met with 28 and 29 vol.-% of Sn-Pb for Sn-Pb/CNT/PP and Sn-Pb/CCB/PP, respectively.

Keywords: High electrical conductivity; Tin-lead polymeric composites; Injection molding; Melting range.

1. Introduction

When an electrically conducting material is dispersed in sufficient quantity in a insulated polymeric matrix, an electrically conductive composite will be formed.[1] Since the first experimental result was published decades ago, unique properties of such polymeric composites have made them adapted to a variety of applications, including electrostatic dissipation, electromagnetic interference shielding, conductive adhesives and circuit elements, according to their electrical conductivity and temperature coefficient of resistance. Polymeric composites with high electrical conductivity ($>10 \text{ S}\cdot\text{cm}^{-1}$) are applicable as bipolar plates of polymer electrolyte membrane (PEM) fuel cells.[2] PEM fuel cell is an electrochemical device that produces electricity by separating the fuel via a catalyst. The protons flow through a membrane and combine with oxygen to regenerate water with the help of the catalyst used while the electrons flow from the anode to the cathode to create electricity.[3] Since the fuel reacts electrochemically instead of combustion, PEM fuel cell is found to be potentially more efficient than the conventional power plants and may offer one of the most lucrative and clean possibilities for future power sources.[4] As one of the key components of PEM fuel cell, the majority of fuel cell bipolar plates have been fabricated by stainless steel or graphite.[5] However, the cost of these plates is quite high, principally due to the costly gas channel machining step.

Many high electrically conductive (HEC) composites based on thermoplastics have been developed for PEM fuel cell bipolar plates, because of their potential advantages in lower cost, lower weight and greater ease of manufacture than the traditional plates. Graphite/polypropylene(PP), graphite/carbon black (CB)/polyaniline/PP, S316L stainless steel alloy fibers/nylon 6, ternary-layered metalliclic carbide/polyvinylidene fluoride(PVDF), CB/flake graphite (GR)/silver coated glass particles/carbon nanotubes (CNTs)/low-viscosity polyethylene terephthalate (PET), CB/GR/carbon fibers/polyphenylene sulfide (PPS)/PP, CNT/PET/PVDF, GR/PPS and CNT coated 304 stainless steel/PP [3-16] have been reported and all of them showed high electrical conductivities in the range from 10 to $100 \text{ S}\cdot\text{cm}^{-1}$. In order to achieve high conductivity, the filler concentration in those composites had to be high (usually 50~70 vol.-%) and greatly exceeded percolation threshold. [17] Due to the high loading and the resulting poor flow properties, compression molding rather than injection molding has been used for those composites [3, 9, 12, 13, 16]. As compared with compression molding, injection molding is more promising, cost

effective and suitable for industrial scale production. [18] Our present work was hence focused on HEC polymeric composites that can be injection-molded.

Injection molding requires the processed composites with low melt viscosity. To reduce the high melt viscosity caused by high filler loading, one essential kind of fillers is needed, which is has low melt viscosity at the mixing temperature and exist as solid with high electrical conductivity at the working temperature. Low-melting-point (LMP) metallic alloys, such as In-Bi, Sn-Pb, Bi-Sn and Sn-Cu, are one kind of important candidates for this material. However, Sn-Pb (60/40) alloy (60 wt.-% Sn and 40 wt.-% Pb)/polymer composites has been reported in the literatures and their electrical conductivity was not high. Sn-Pb/polystyrene composites just attained an electrical conductivity of $0.01 \text{ S}\cdot\text{cm}^{-1}$ with 35 vol.-% of Sn-Pb (60/40). [19] The electrical conductivity of Sn-Pb/high density polyethylene composites was $0.5 \text{ S}\cdot\text{cm}^{-1}$ with 45 vol.-% of Sn-Pb (60/40). [20] It was because that those Sn-Pb (60/40) particles were discretely dispersed in the polymeric matrices and could not efficiently form a long-range conductive network. The conductivity of the composites was limited by the high resistance of polymers between neighbor alloy particles.

To increase electrical conductivity of LMP metallic alloy/polymer composites to $10 \text{ S}\cdot\text{cm}^{-1}$ and above for potential applications in the field of PEM fuel cells, a metallic alloy composite system have been developed. In this system, the metallic alloy have such a wide melting range that it is practicable for itself to form a stable solid-liquid mixture when being mixed with other materials and the liquid phase will serve as a solder to connect neighbor alloy particles to form long-range high conductive channels. In the present study, we verified this approach through the successful preparation of HEC Sn-Pb/polypropylene (Sn-Pb/PP) composites using Sn-Pb (40/60) and Sn-Pb (20/80) as the conducting fillers, which have melting ranges from 183 to 240 °C and from 183 to 265 °C, respectively. Hence, we applied this approach in preparation of Sn-Pb (20/80)/conductive carbon/PP composites for PEM fuel cell bipolar plates. It turned out that those ternary composites were high electrically conductive and injection moldable. In addition, the effect of Sn-Pb loading on the mechanical properties and the corrosion resistance of Sn-Pb(20/80)/Carbon/PP composites were also tested.

2. Experimental

2.1. Materials

Polypropylene (PP, MB3020-01) was purchased from Aldrich with a melt index of 4.0 g/10 min (230°C/2.16kg). Tin-lead alloy (Sn-Pb) solder wires (20/80) were purchased from Sellery Tools Pte Ltd and Sn-Pb solder wires (40/60) were purchased from RS Components Pte Ltd. Both of them were cut into small pieces and purified by washing using acetone to remove the rosin core. Conductive carbon black/polypropylene composite (CCBPP) was purchased from Iljin Nano Tech (Korea) with a weight ratio of 70/30(volume ratio 83.9/16.1). Carbon nanotube/polypropylene composite (CNTPP, MB3020-01) was purchased from Hyperion Catalysis (USA) with a weight ratio of 80/20(volume ratio 83.9/16.1).

2.2. Preparation of Sn-Pb/PP composites

The detailed formulas for preparing electrically conductive Sn-Pb/PP composites are shown in Table 1. The Sn-Pb (20/80)/PP composites were prepared by melt mixing at 220°C in a HAAKE MiniLab (Thermo Scientific) at a screw speed of 80 rpm. The Sn-Pb (40/60)/PP composites were prepared at 190 °C at the same screw speed. Injection molding was performed on a HAAKE mini-Jet (Thermo Scientific) and the injection molding conditions are shown in Table 1.

Table 1. Injection Molding Condition.

| | <i>Sn-Pb/PP</i> | <i>Sn-Pb(20/80)/Carbon/PP</i> |
|------------------------|-----------------|-------------------------------|
| Melt Temperature/°C | 250 | 250 |
| Mold Temperature/°C | 70 | 100 |
| Injection Pressure/MPa | 850 | 850 |
| Injection Duration/Sec | 10 | 10 |
| Post Pressure/MPa | 300 | 500 |
| Post Duration/Sec | 10 | 10 |

2.3. Preparation of Sn-Pb(20/80)/Carbon/PP composites

The detailed formulations for preparing electrical conductive composites of Sn-Pb(20/80)/Carbon/PP were shown in Table 2. Sn-Pb(20/80)/Carbon/PP composites were fabricated by melt mixing at 220°C in the HAAKE

MiniLab at a screw speed of 60 rpm. Injection molding was performed on the HAAKE mini-jet and the injection molding conditions are shown in Table 1.

2.3. Characterization Techniques.

The densities of PP, alloys and composites were measured on a Precisa 180A electronic balance (Precisa Balances) using the buoyancy method with ethanol as the vehicle at 25 °C. The fractured surfaces of composites were coated with a thin layer of gold and observed by a JSM-5600LV scanning electron microscopy (SEM, JEOL). The volume electrical conductivity was acquired using a Fluke 110 digital multimeter (Fluke). The size of rectangle samples was 35.0 mm×5.0 mm×1.7mm with both ends coated with the silver conductive adhesive. The thermal behaviors of the samples were measured using a DSC7 differential scanning calorimeter (DSC, PerkinElmer). The samples were heated rapidly from room temperature to 300°C at a rate of 50 °C/min and held for 1 min to eliminate the thermal history. Subsequently, the samples were cooled to -30 °C at a rate of 10°C/min and then were heated to 300°C at the same rate. The crystallization temperature (T_c) and the melting temperature (T_m) were obtained from the cooling thermogram and the second-heating thermogram, respectively. The crystallization and melting enthalpies (ΔH_c and ΔH_m) of PP were determined from the enthalpies of composites obtained from DSC, which were divided by the weight percent of PP in the composites. Mechanical tests were carried out on an INSTRON 5569 universal testing machine (Instron) at room temperature. The test speeds were 50 mm/min and 1 mm/min for tensile and flexural tests (three-point flexure fixture with a support span of 32 mm), respectively. The size of dumb-bell shaped specimens was designed according to ASTM D638 test method and the rectangle specimen for flexural test had a size of 35.0 mm×5.0 mm×1.7mm. Corrosion rate studies of composites were conducted in 0.1M H₂SO₄ (pH ~3) electrolyte to simulate the fuel cell acidic environment [27].

3. Results and discussion

3.1. Sn-Pb/PP composites

Table 2. Physical properties of Sn-Pb/PP composites.

| Samples | PP/Sn-Pb | | Density (g·cm ⁻³) | Tensile Strength /MPa | Flexural Strength /MPa | Electrical Conductivity (S·cm ⁻¹) |
|--------------|-----------------|-----------------|----------------------------------|-----------------------------|------------------------------|--|
| | Weight Ratio | Volume Ratio | | | | |
| PP | - | - | 0.9 | 35.6 | 52.3 | 10 ⁻¹⁷ [21] |
| Sn-Pb(20/80) | - | - | 10.2 | - | - | 1.0×10 ⁵ |
| PP20-1 | 50/50 | 92/8 | 1.7 | 31.7 | 45.3 | <7.5×10 ⁻⁷ |
| PP20-2 | 31/69 | 84/16 | 2.3 | 27.9 | 33.2 | 7.4×10 ⁻³ |
| PP20-3 | 16/84 | 68/32 | 3.8 | 23.3 | 32.5 | 53 |
| Sn-Pb(40/60) | - | - | 9.3 | - | - | 1.0×10 ⁵ |
| PP40-1 | 53/47 | 92/8 | 1.5 | 35.3 | 43.1 | <7.5×10 ⁻⁷ |
| PP40-2 | 36/64 | 85/15 | 2.2 | 31.5 | 42.5 | <7.5×10 ⁻⁷ |
| PP40-3 | 19/81 | 70/30 | 3.3 | 29 | 41.7 | 4.2 |

3.1.1. Electrical conductivity of Sn-Pb/PP composites

The electrical conductivity of Sn-Pb/PP composites molded at 250 °C is shown in Table 2. The conductivity of neat PP was at the level of 10⁻¹⁷ S·cm⁻¹ [21] and the conductivity of PP20-1 was lower than the measurable range of our ohmmeter (7.5×10⁻⁷ S·cm⁻¹). With increasing the loading of Sn-Pb (20/80), the conductivity increased dramatically. For PP20-2, the conductivity was 7.4×10⁻³ S·cm⁻¹. With increasing Sn-Pb (20/80) loading to 32 vol.-%, the conductivity exceeded 10 S·cm⁻¹ and reached 53 S·cm⁻¹, which was an increase by 18 orders of magnitude from that of neat PP. Similar dramatic improvement was also observed for Sn-Pb (40/60)/PP composites. The conductivity of PP40-3 achieved 4.2 S·cm⁻¹. The conducting mechanism of composites involves the mutual contact of conductive fillers in the matrix and the formation of long-range conductive channels. Figure 1 shows the phase structures of Sn-Pb/PP composites with various loadings of Sn-Pb. The bright areas in SEM images state for the Sn-Pb particles. From Figure 1(a-c), it can be seen that the average size of Sn-Pb particles maintained around 50 μm, while the density of Sn-Pb particles gradually increased with increasing the loading of Sn-Pb (20/80). Apparently, with the density of Sn-Pb particles increased, Sn-Pb phase occupied more space in the composites and form a continuous conductive network, which resulted in the significant increase in electrical conductivity. For Sn-Pb (40/60)/PP composites, as shown in Figure 1 (d-f), the average size of Sn-Pb particles increased with increasing the loading of Sn-Pb (40/60). Small Sn-Pb particles merged into discrete big ones instead of forming a long-range

conductive network. Therefore, the electrical conductivity of PP40-3 molded at 250 °C was much lower than that of PP20-3.

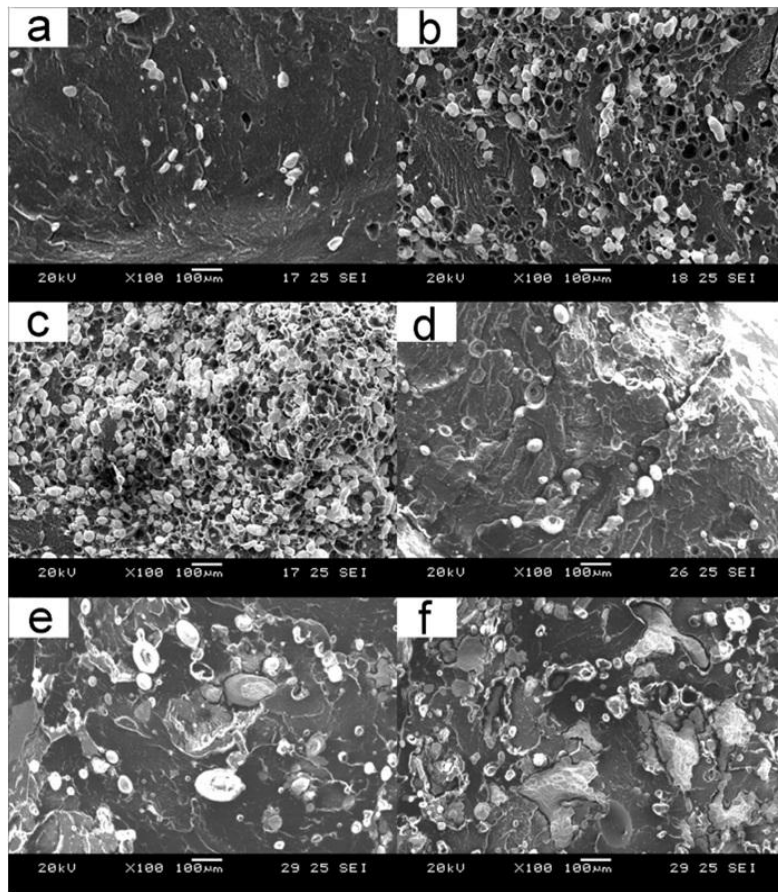


Figure 1. SEM images of Sn-Pb/PP composites molded at 250 °C: a) PP20-1, b) PP20-2, c) PP20-3, d) PP40-1, e) PP40-2, and f) PP40-3

3.1.2. Mechanical properties of Sn-Pb/PP composites

The values of tensile and flexural strengths of Sn-Pb/PP composites are shown in Table 2. It can be seen that the tensile and flexural strengths of neat PP were 36 MPa and 50 MPa, respectively. With increasing the loading of Sn-Pb (20/80), tensile and flexural strengths of Sn-Pb/PP composites decreased gradually and reached 23 MPa and 33 MPa at 32 vol.-% of Sn-Pb (20/80), dropping by 34.5% and 37.9%, respectively. The same trend was observed for Sn-Pb (40/60)/PP composites. At the loading of 30 vol.-%, tensile and flexural strengths dropped by 18.5% and 20.2%, respectively. The decrease in mechanical properties was due to the poor compatibility between PP and Sn-Pb alloys. From Figure 1, it can be observed that there was almost no adherence between two phases, which impaired the tensile and flexural strengths of materials.

3.1.3. Effect of molding temperature on electrical conductivity

Figure 2 shows the electrical conductivity of PP40-3 molded at three different temperatures: 190, 210 and 250 °C. The other injection molding conditions were same. It can be seen that PP40-3 molded at 210 °C had the highest conductivity of $90 \text{ S}\cdot\text{cm}^{-1}$ among those three samples, which was even higher than that of PP20-3 molded at 250 °C ($53 \text{ S}\cdot\text{cm}^{-1}$). It is well known that the formation of long-range conductive paths is the determinant for achieving high conductivity of HEC polymeric composites. From SEM images of PP40-3 as prepared by melting mixed and PP40-3 molded at three different temperatures (Figure 3), it can be seen that the structure changed significantly after injection molding. Sn-Pb particles of PP40-3 molded at 190 °C and 250 °C remained discretely dispersed in the matrix and there still was no apparent formation of long-range conductive paths. For PP40-3 molded at 210 °C, the

particles of Sn-Pb formed a continuous network, which contributed to the increase of electrical conductivity. This indicated that the molding temperature has a significant effect on the phase structures of composites. A scheme was suggested in Figure 4 to explain the formation of different phase structures induced by the temperature. From the phase diagram of Sn-Pb alloy, it can be known that the fraction of liquid phase for Sn-Pb (40/60) increase from 50% to 65.5% with increasing the temperature from 190 to 210 °C and the alloy becomes completely liquid at 250 °C.

The viscosity of Sn-Pb particles would decrease with increasing the fraction of liquid phase and there was a gradual change from very high viscosity (solid) to very low viscosity (liquid) in a temperature window, which was the melting range. Two particles would retain separated or be stuck together when they collided. The shape of the resultant particles depended on the viscosity of each particle. With increasing the temperature, they would be discrete particles (as illustrated in Figure 3(b)), chains formed from stuck particles soldered by liquid phase (as illustrated in Figure 3(c)), or even big discrete particles formed by small droplets' merging (as illustrated in Figure 3(d)). The resistance between neighbor discrete conductive particles was very large. This explains why high electrical conductivity could hardly be achieved by adding conductive solid powders (an example of extremely high viscosity) even with a high loading in the literatures. [19,20,22,23] Therefore, in order to prepare polymeric composites with high electrical conductivity, the conductive fillers must have a melting range and be able to form a stable solid-liquid mixture when mixed with polymers.

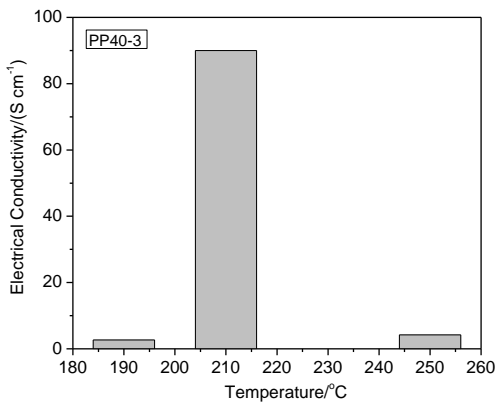


Figure 2. Electrical conductivity of PP40-3 obtained at three molding temperature.

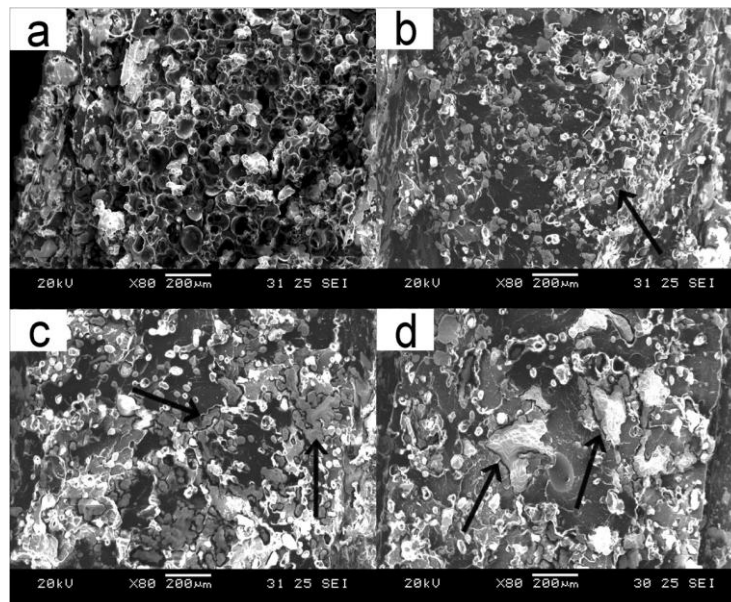


Figure 3. SEM images of PP40-3 as melting mixed (a) and PP40-3 molded at 190 °C (b), 210 °C (c) and 250 °C (d).

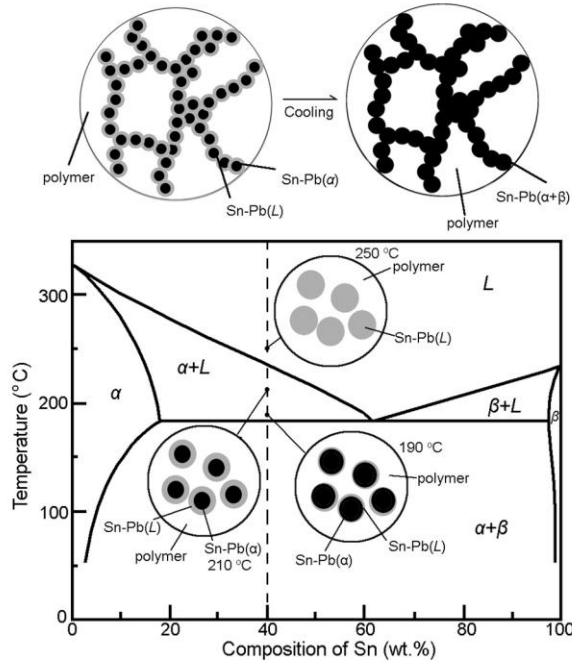


Figure 4. Formation of a conducting network of Sn-Pb particles soldered by liquid phase.

3.2. Sn-Pb(20/80)/Carbon/PP composites

Table 3. Physical properties of Sn-Pb(20/80)/Carbon/PP composites.

| Samples | CarbonPP/Sn-Pb | | Bulk Density /g cm ⁻³ | Tensile Strength /MPa | Flexural Strength /MPa |
|---------|----------------|--------------|-------------------------------------|--------------------------|---------------------------|
| | Weight Ratio | Volume Ratio | | | |
| CCBPP | - | - | 1.0 | 27.8 | 43.8 |
| CCBPP1 | 1/2 | 83.3/16.7 | 2.5 | 22.1 | 38.6 |
| CCBPP2 | 1/3 | 76.9/23.1 | 3.3 | 20.8 | 36.7 |
| CCBPP3 | 1/4 | 71.4/28.6 | 3.8 | 19.9 | 29.4 |
| CCBPP4 | 1/5 | 66.7/33.3 | 4.4 | 16.7 | 25.5 |
| CNTPP | - | - | 1.0 | 39.7 | 64.1 |
| CNTPP1 | 1/0.53 | 95/5 | 1.6 | 38.0 | 55.0 |
| CNTPP2 | 1/1.1 | 90/10 | 2.1 | 34.6 | 54.9 |
| CNTPP3 | 1/2.5 | 80/20 | 3.1 | 29.1 | 40.9 |
| CNTPP4 | 1/4.3 | 70/30 | 3.9 | 22.3 | 37.4 |

Polymeric composites prepared by this kind of conductive fillers could be easily injection-molded and possessed a high electrical conductivity. These properties offered a potential application in PEM fuel cell bipolar plates. To increase the conductivity of matrices, conductive carbon PP master batches were used to mix with Sn-Pb(20/80) and the potential of the composites for PEM fuel cell application was examined.

3.2.1. Electrical conductivity of Sn-Pb(20/80)/Carbon/PP composites

The electrical conductivity of Sn-Pb(20/80)/Carbon/PP composites is shown in Figure 5. It can be seen that the conductivity of CCBPP and CNTPP was 0.3 and 2.5 S·cm⁻¹, respectively. With increasing the Sn-Pb loading from 5 to 30 vol.-%, the conductivity of Sn-Pb/CNT/PP increased gradually from 2.9 to 190 S·cm⁻¹, and the conductivity of Sn-Pb/CCB/PP increased gradually from 0.55 to 550 S·cm⁻¹ with increasing the Sn-Pb loading from 18.2 to 33.3 vol.-%. With 14 vol.-% of Sn-Pb, the conductivity of Sn-Pb/CNT/PP achieved 10 S·cm⁻¹, the lowest electrical requirement for PEMFC bipolar plates, [2] For Sn-Pb/CCB/PP composites, it needed 25 vol.-% of Sn-Pb to reach the same value. The current FreedomCAR target for bipolar plates was 100 S·cm⁻¹, [5] and it was met with 28 and

29 vol.-% of Sn-Pb for Sn-Pb/CNT/PP and Sn-Pb/CCB/PP, respectively. In comparison with Sn-Pb/CCB/PP, Sn-Pb/CNT/PP had a much higher conductivity and could meet the electrical requirement with less Sn-Pb. Figure 6 shows phase structures of Sn-Pb(20/80)/Carbon/PP composites with various loadings of Sn-Pb. The bright phase in SEM images is the Sn-Pb phase. It can be seen from Figure 6(a-d) that the average size of Sn-Pb particles was around 40 μm and the density of Sn-Pb particles increased with increasing the loading of Sn-Pb. Apparently, with the density of Sn-Pb particles increased, Sn-Pb particles were able to contact with each other and form a conductive network, which resulted in the dramatic increasing of the conductivity. For Sn-Pb/CNT/PP, as shown in Figure 6(e-h), the average size of Sn-Pb particles was also around 40 μm . Likewise, with increasing the loading of Sn-Pb, Sn-Pb particles contacted with each other and formed a long-range conductive channels soldered by liquid phase in them.

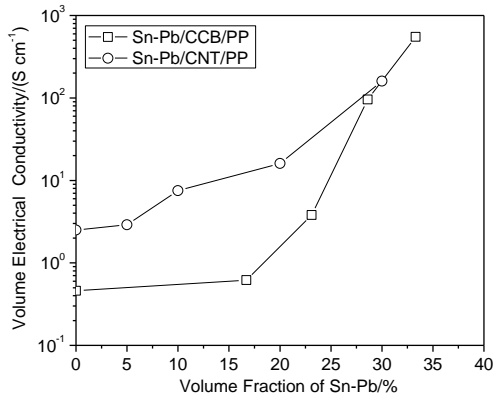


Figure 5. Electrical conductivity of Sn-Pb/CCB/PP and Sn-Pb/CNT/PP composites.

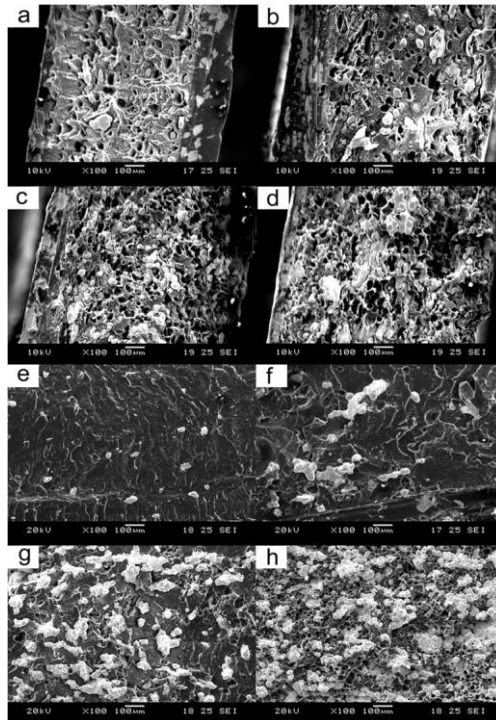


Figure 6. SEM images of Sn-Pb(20/80)/Carbon/PP composites: a) CCBPP1, b) CCBPP2, c) CCBPP3, d) CCBPP4 and e) CNTPP1, f) CNTPP2, g) CNTPP3 and h) CNTPP4.

3.2.2. Mechanical properties of Sn-Pb(20/80)/Carbon/PP composites

The values of tensile strength, elongation at break and flexural strength of Sn-Pb(20/80)/Carbon/PP composites are summarized in Table 3. The tensile and flexural strengths of CCBPP were 27.8 MPa and 43.8MPa, respectively, and they were 39.7 MPa and 64.1 MPa for CNTPP. It can be seen that with increasing the Sn-Pb loading, tensile strength and flexural strength of Sn-Pb(20/80)/Carbon/PP decreased gradually. The tensile and flexural strengths of Sn-Pb/CCB/PP with 33.3 vol.-% of Sn-Pb were 16.7 MPa and 25.5 MPa, respectively. For Sn-Pb/CNT/PP with 30 vol.-% of Sn-Pb, their values were 22.3 MPa and 37.4 MPa, respectively. , Because of the better mechanical properties of raw CNTPP, Sn-Pb/CNT/PP exhibited better mechanical properties than Sn-Pb/CCB/PP Due to the poor mechanical properties of raw CNTPP and CCBPP, the tensile strength and flexural strength of Sn-Pb(20/80)/Carbon/PP composites did not meet the rigorous mechanical targets of current FreedomCAR target for bipolar plates (flexural strength >59 MPa and tensile strength >41 MPa) [5]. However, these conductive composites were strong enough and should not break under normal cell assembling and operating conditions of PEM fuel cell. The mechanical properties can be improved by choosing better carbon filled PP composites.

4. Conclusion

Tin-lead alloy (Sn-Pb) featured with a wide melting range was used to prepare highly conductive polymeric composites. Sn-Pb/polypropylene (PP) composites and Sn-Pb/conductive carbon/PP (Sn-Pb/Carbon/PP) composites were obtained through melt mixing. Sn-Pb (20/80) and Sn-Pb (40/60) were used to study the impact of Sn-Pb component and processing temperature on electrical conductivity of Sn-Pb/PP composites. It was found that both of them had significant effect on the achievement of high electrical conductivity. With increasing the loading of Sn-Pb, the electrical conductivity increased dramatically. Based on the results of the effect of molding temperature on electrical conductivity, it was proved that the viscosity of Sn-Pb particles at the mixing temperature was the key issue to form long-range conducting paths soldered by liquid phase in Sn-Pb particles. Therefore, in order to prepare polymeric composites with high electrical conductivity, the conductive fillers must have a melting range and be able to form a stable solid-liquid mixture when mixed with other materials. This approach was applied in preparation of Sn-Pb (20/80)/Carbon/PP composites for PEM fuel cell bipolar plates. Two conductive carbons used were conductive carbon black (CCB) and carbon nanotubes (CNTs). Those ternary composites were high electrically conductive and injection moldable. The conductivity of Sn-Pb/CNT/PP and Sn-Pb/CCB/PP composites achieved $10 \text{ S}\cdot\text{cm}^{-1}$ with 14 vol.-% 25 vol.-%, respectively. The current FreedomCAR target for bipolar plates of $100 \text{ S}\cdot\text{cm}^{-1}$ was met with 28 and 29 vol.-% of Sn-Pb for Sn-Pb/CNT/PP and Sn-Pb/CCB/PP, respectively. With increasing the loading of Sn-Pb, tensile and flexural strengths of Sn-Pb/Carbon/PP composites decreased gradually due to the poor compatibility between PP and Sn-Pb. Corrosion resistance of Sn-Pb(20/80)/Carbon/PP composites were tested and corrosion process of Sn-Pb was depressed in CCBPP and CNTPP in comparison with bulk Sn-Pb.

Acknowledgement

This work was supported by the A*STAR SERC Grant (No. 0721010018), Singapore.

5. References

- [1] Strümpler R and Glatz-Reichenbach J. Conducting polymer composites. *J Electroceramics* 1999; 3(4): 329-346.
- [2] Wilson MS and Busick DN. Composite bipolar plate for electrochemical cells. US patent 6248467, 2001.
- [3] Salwan S. Dihrab, K. Sopian, M.A. Alghoul, M.Y. Sulaiman *Renewable and Sustainable Energy Reviews* 13 (2009) 1663–1668.
- [4] H. Tawfik, Y. Hunga, D. Mahajan ,*Journal of Power Sources* 163 (2007) 755–767.
- [5] B. D. Cunningham, J. Huang,D. G. Baird *International Materials Reviews* 2007(52):1-13.
- [3] Müller A, Kauranen P, Von Ganski A, Hell B. Injection moulding of graphite composite bipolar plates. *Journal of Power Sources* 2006; 154(2):467-471.
- [4] Wang Y. Conductive thermoplastic composite blends for flow field plates for use in polymer electrolyte membrane fuel cell (PEMFC), M.S. Thesis., University of Waterloo, Ontario, Canada, 2006.
- [5] Vielstich W, Gasteiger HA, Lamm A.editor. *Handbook of fuel cells-fundamentals, technology and applications*. New York: John Wiley & Sons, Inc: 2003. p.274.
- [6] Dweiri R and Sahari J. Electrical properties of carbon-based polypropylene composites for bipolar plates in polymer electrolyte membrane fuel cell (PEMFC). *Journal of Power Sources* 2007; 171(2) 424-432.

- [7] Yeetsorn R, Fowler M, Tzoganakis C, Yuhua W, Taylor M. Polypropylene composites for polymer electrolyte membrane fuel cell bipolar plates. *Macromol Symp* 2008; 264(1): 34-43.
- [8] Greenwood P, Chen R, Thring RH. Polyethylene-carbon material for polymer electrolyte membrane fuel cell bipolar plates. *Proc IMechE Part L: J Materclas: Dsign and Application*. 2008; 222(3):197-208.
- [9] Kuo JK and Chen CK. A novel Nylon-6-S316L fiber compound material for injection molded PEM fuel cell bipolar plates. *J Power Sources* 2006; 162(1): 207-214.
- [10] Zhu B, Mei B, Shen C, Yuan R. Study on the electrical and mechanical properties of polyvinylidene fluoroide/titanium silicon carbide composite bipolar plates. *Journal of Power Sources* 2006; 161(2): 997-1001.
- [11] Bouatia S, Mighri F, Bousmina M. Development and characterisation of electrically conductive polymeric-based blends for proton exchange membrane fuel cell bipolar plates. *Fuel Cell* 2008; 8(2):120-128.
- [12] Mighri F, Huneault MA, Champagne M F. Electrically conductive thermoplastic blends for injection and compression molding of bipolar plates in the fuel cell application. *Polym Eng Sci* 2004; 44(9): 1755-1765.
- [13] Wu M and Shaw LL. On the improved properties of injection-molded, carbon nanotube-filled PET/PVDF blends. *J Power Sources* 2004; 136(1): 37-44.
- [14] Huang J, Baird DG, McGrath JE. Development of fuel cell bipolar plates from graphite filled wet-lay thermoplastic composite materials. *J Power Sources* 2005; 150(1): 110-119.
- [15] Lee YB, Lee CH, Lim DS. The electrical and corrosion properties of carbon nanotube coated 304 stainless steel/polymer composite as PEM fuel cell bipolar plates. *International Journal of Hydrogen Energy* 2009; 34(24): 9781-9787.
- [16] Sorensen IW. High conducting polymer-metalllic alloy blends. US Patent 4557857, 1985.
- [17] Sichel EK, editor. Carbon black-polymer composites. New York: Marcel Dekker: 1982.
- [18] Ledjeff-Hey K, Kalk T, Mahlendorf F, Niemzig O, Trautmann A, Roes J. Portable PEFC generator with propane as fuel. *J Power Sources* 2000; 86(1-2): 166-172.
- [19] Zhang X W, Pan Y, Shen L, Zheng Q, Yi X S. A novel low-melting-point alloy-loaded polymer composite. I. Effect of processing temperature on the electrical properties and morphology. *J Appl Polym Sci* 2000; 77(5): 1044-1050.
- [20] Zhang XW, Pan Y, Zheng Q, Yi XS. A new polymer composite thermistor having double PTC transitions. *J Appl Polym Sci* 2000; 78(2): 424-429.
- [21] King JA, Johnson BA, Via MD, Ciarkowski CJ. Electrical conductivity of carbon-filled polypropylene-based resins. *Journal of Applied Polymer Science* 2009; 112(1): 425-433.
- [22] Mamunya YP, Davydenko VV, Pissis P, Lebedev EV. Electrical and thermal conductivity of polymers filled with metallic powders. *European Polymer Journal* 2002; 38 (9): 1887-1897.
- [23] Yu J, Wang N, Ma X. Fabrication and characterization of poly(lactic acid)/acetyl tributyl citrate/carbon black as conductive polymer composites. *Biomacromolecules* 2008; 9(3): 1050-1057.
- [24] Purnima D, Maiti SN, Gupta AK. Interfacial adhesion through maleic anhydride grafting of EPDM in PP/EPDM blend. *J Appl Polym Sci* 2006; 102 (6): 5528-5532.

Dr. PAN Yongzheng was working in Institute of Materials Research & Engineering, A*Star, Singapore as a Scientist I when submitting this paper. He is currently working with RTP Company, a global compounder of custom engineered thermoplastics, as a product development engineer. His expertise is developing conductive thermoplastic composites as well as products applied in medical devices. He obtained his Ph.D degree from Nanyang Technological University on 2012.

Film for Filtering Infra-Red Radiation from the Sunlight

¹Kang Semi, ¹Kim Jee Hyun, ¹Murali Krishnaswamy, ²Hong Han*

1: NUS High School of Mathematics and Science

2: Institute of Chemical and Engineering Sciences
1 Pesek Road, Jurong Island Singapore, 627833
Email: honghan@SCS-chem.com.sg

Abstract: Radical Polymerisation of 3 monomers, Poly(methyl methacrylate) (PMMA), Poly(acrylic acid) (PAA) and Poly (acrylonitrile) (PAN) was carried out using freeze-pump-thaw method to produce co polymer with enhanced mechanical property for blocking Mid Infrared (MIR) radiation. For blocking Far Infrared (FIR), pyrolysis of ammonia-trifluoroborane, H_3NB_3F was successfully carried out under high vacuum condition to produce polymeric aminodifluoroborane, $(H_2NB_2F)_n$. The polymers were made into film and the IR spectrometry was analysed by FTIR, and the effectiveness of polymer in real life situations was analysed by measuring temperature change of polymer coated test tubes, under exposure of sunlight, over period of 4 days with successful results. This functional polymer which absorbs IR while maintaining optical transparency can be applied to many applications.

Keywords: Radical Polymerisation; Infrared (MIR) radiation; film; sunlight.

1. Introduction

The solar radiation spectrum which reaches the earth is mainly the non ionising radiation because the highly ionising radiations are cancelled out by the earth's atmosphere. MIR (4000 cm^{-1} to 400 cm^{-1}) is where the thermal waves begin to produce heat and humans can feel the heat [8]. (For the definition of FIR and MIR, International Organization for Standardization (ISO) 20473 scheme was followed). Developing a film of novel functional polymer which absorbs infrared radiation (IR) range and maintain its optical transparency will have many applications. For an example, an elevated infrared absorption can filter heat radiation through window coated with films and keep a room cool in summer [1-4].

One of the most popular used window materials is glass. When The glass is mainly made up of silicate (MO_x/SiO_2) which has Infrared Spectra from 600 cm^{-1} to 400 cm^{-1} [5-7]. To effectively block the FIR (400 cm^{-1} to 10 cm^{-1}), which can penetrate several mm and is used for houses and premises heating, we synthesized and investigated inorganic polymer $(H_2NB_2F)_n$, which has high dipole moment. It was found to block IR range of 480 cm^{-1} to 10 cm^{-1} after running the polymer under Fourier Transform Infrared spectroscopy (FTIR). Co polymer was made to efficiently block the MIR by combining polymers which blocks different range of MIR and has suitable property to be made into film. The functional polymer coating for absorbing IR was evaluated in 'outdoor' condition in which it was exposed to sunlight. The graph of change in temperature over time showed lower temperature change initially compared to the control.

Meanwhile, Smart glass generally refers to glasses which can control the light transmission by switching its transparency electrically. $(H_2NB_2F)_n$ has phase behaviour and change in phases was observed at temperature around $130^\circ C$, in which the film made from Poly (vinylidene fluoride) (PVDF) and the polymer turned from white to transparent. Even though further analysis on this property was not carried out due to time constraint, we predict that this can be further developed by lowering the temperature of the phase change to near room temperature.

2. Experimental

2.1. Synthesis of polymers

2.1.1. Radical Polymerisation

Commercially available monomers, PMMA, PAA, PAN, Poly(acrylic acid–co–methyl methacrylate–co–acrylonitrile) (Poly(AA–co–MMA–co–AN) was synthesised using air-free technique, the freeze-pump-thaw method. Azobis(cycli hexanecarbonitrile) (ABCN) was used as initiator and dimethylformamide (DMF) was used as solvent. Inhibitor which comes with monomers to prevent undesired polymerisation was removed using Aluminium Oxide

(Al_2O_3) and syringe filters. Compared to applying 3 separate layers of film, creating co-polymer has increased mechanical property and is more feasible for application.

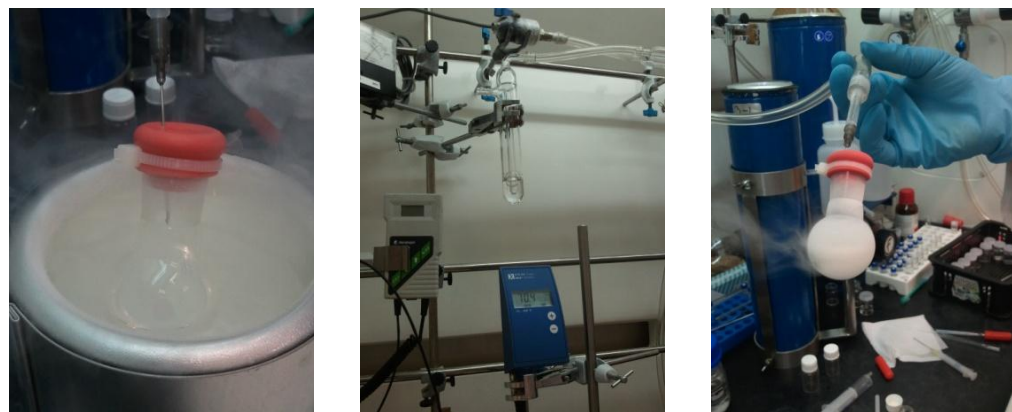
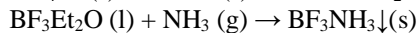
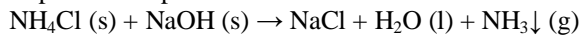


Figure 1. Free radical polymerization preparation

2.1.2. Synthesis of polymeric aminodifluoroborane

A) Preparation of precursor



Trifluoroboronetherate ($\text{BF}_3\text{Et}_2\text{O}$) which is water sensitive was completely sealed in two neck round bottom flask with toluene and was cooled to 0°C by surrounding the flask with ice with salt. NH_3 was produced by reacting Ammonium Chloride (NH_4Cl) with Sodium Hydroxide (NaOH). Balloons were attached to each of the flasks to assuage the increased pressure due to the reactions. The two set ups were connected such that NH_3 had to go through NaOH (s), which absorbs moisture, before reacting with $\text{BF}_3\text{Et}_2\text{O}$. Afterwards, BF_3NH_3 which was mixed with toluene was dried using filter paper and vacuum.

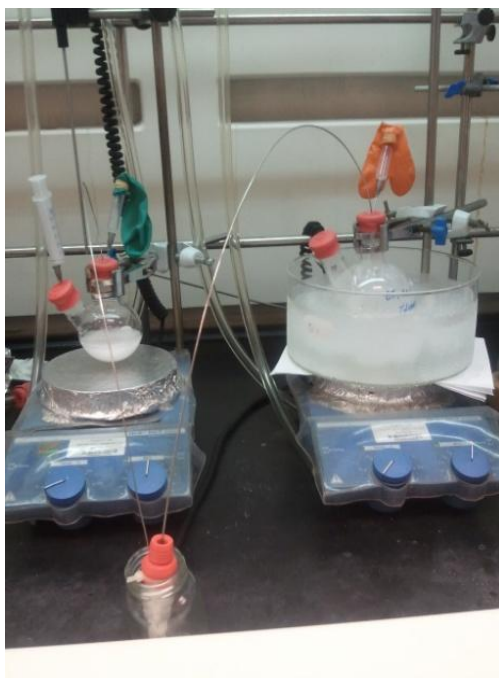


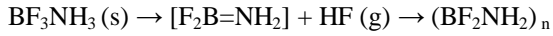
Figure 2. Device of the precursor preparation.

B) Polymerisation via pyrolysis



Figure 3. device of the polymerization.

Polymerisation of the precursor BF_3NH_3 was carried out via pyrolysis under high vacuum.



BF_3NH_3 was placed in a flask and was covered by fine sand to prevent sublimation. Then, it was heated at around 185°C which decomposed the bond and formed double bond between B and N, forming $\text{F}_2\text{B}=\text{NH}_2$ in transition state. The set up was kept at $2.0 \times 10^{-2}\tau$ to remove gaseous hydrogen fluoride (HF) to make the process irreversible and shift the equilibrium to the right. Afterwards, it was cooled at -196°C using liquid nitrogen to form -196°C .

2.2. Film Making

2.2.1. General film making methodology

Slides were washed with acetone and dried to ensure easier spreading of hydrophobic solutions across the surface. A drop of solution was dropped onto cover slide for films which are not waterproof and onto microscopic slide for films which are waterproof. Then, by using the flat side of the pipette, the solution was spread out evenly across the surface and heated on hot plate at average of 50°C for faster process of formation of film. After the films were formed, waterproof films were taken off the slide using water or other medium to become free standing films.

2.2.2. Aminodifluoroborane + PVDF film making

Homogeneous solutions were prepared dissolving Poly(vinylidene fluoride-co-hexafluoropropylene) (PVDF) polymer pallets in Dimethylformamide (DMA) at room temperature by magnetic stirring for about 24h, in 10% and 15% concentration. The polymeric aminodifluoroborane that we have synthesized previously was then added to each solution in 1:1 ratio. All of the procedures were carried out in a glove bag, which was sealed and purged with Nitrogen gas in order to vacate most moisture. After the solutions were prepared, a drop of each solution in respective concentrations was dropped onto a glass slide, and was spread evenly with the side of a glass pipette. Each glass slide coated with the polymer solution was then heated at 50°C for 5 minutes with a petri dish covering it on a hot plate, until the film turned milky white. Subsequently, the temperature was raised to $120^\circ\text{C} \sim 150^\circ\text{C}$ (depending on thickness of the coating) and the glass slides was heated until the coating appeared clear.

2.3. Outdoor Simulation

300ml of polymer solution (Refer to above step for detailed preparation methods) was prepared in 10% and 15% concentrations. With a synthetic paintbrush, the 10% polymer solution was evenly coated onto the outer surface of a clean test tube previously rinsed with acetone. The cylinder was then left to dry in room temperature for 30 minutes for it to completely dry. Subsequently, the test tube, then coated with thin milky white film, was reheated with a heat gun first in medium heat ($70 \sim 90^\circ\text{C}$) for 3 minutes and then in high heat ($100 \sim 120^\circ\text{C}$) until the film turns transparent and to make sure that the film was completely dried. These processes were repeated with the 15% solution and pure PVDF solution. 3 of each coated test tubes were produced respectively and each of them was

capped with a rubber septa. The 9 test tubes mentioned above and 3 clean test tubes were arranged on a test tube rack as shown Fig.3.3.1 with a temperature probe connected to each of them. The rack was then exposed to sunlight under the light chimney for three days and the change in the temperature of the atmosphere within each test tube was measured and recorded every 5 minutes for period of 2 days by the data logger connected to 3 laptops as shown in the picture below.

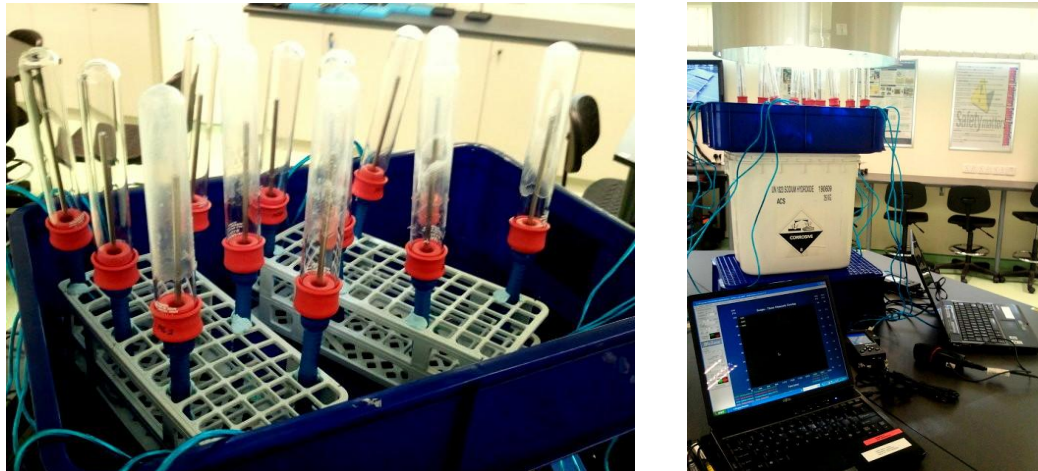


Figure 4. Device for evaluation of the IR filtering performance.

3. Results and Discussion

3.1. The IR Spectrometry

The infrared absorption behaviors of attained polymers were characterized using FTIR scanning spectrometry equipment. Other physical properties were listed in table 1.

Table 1. Summary of the physical properties of the attained polymers.

| Solution (film) | Transparency (film) | Viscosity of solution | Waterproof | IR Spectroscopy |
|-----------------|------------------------------------|-----------------------|------------|---------------------|
| PMMA | Transparent, smooth film | Ideal | Yes | see Appendix Fig.2a |
| PAA | Turns white then turns Transparent | High | No | see appendix Fig.2b |
| PBA | Rough surfaces | | No | see appendix Fig.2c |
| PtBA | white | Ideal | Yes | |

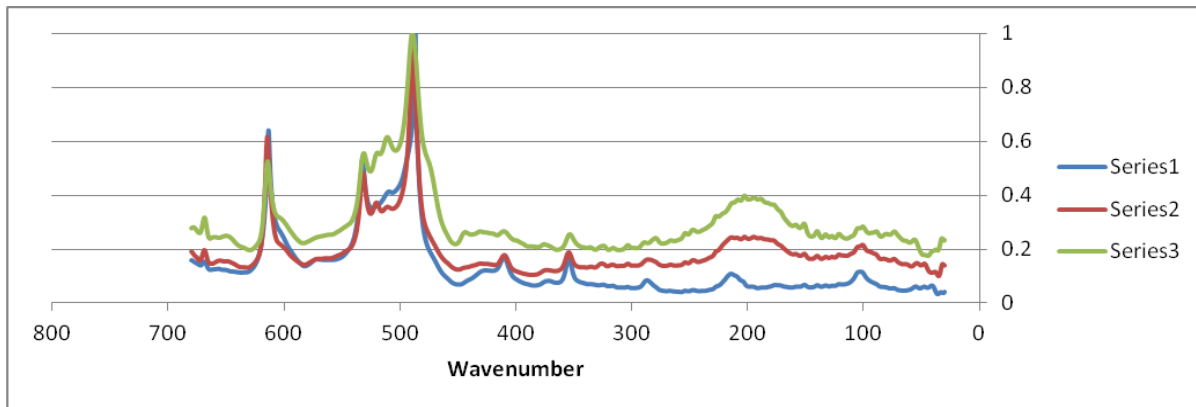


Figure 5. Series 1: PVDF, Series 2: PVDF + Polymer 10%, Series 3: PVDF + Polymer 15%

The IR Spectrometry of polymer BF_3NH_3 with PVDF was measured and was normalised according to the thickness of the films to compare the data of different recipes as shown in figure 5. The original graph which are not normalised can be found in Appendix Fig.1. It can be seen that the IR absorption increased with the content of BF_3NH_3 in PVDF.

3.2. Performance of IR filtration

The performance of IR filtering by the composite films was investigated carefully. The temperature inside the coated glass tube was recorded under the light radiation using a indoor light chamber. The spectra of the radiation light were designed to obtain very close simulation of the sunlight. The recorded curves of Temperature ($^{\circ}\text{C}$) against Time (minutes) were shown in figure 6.

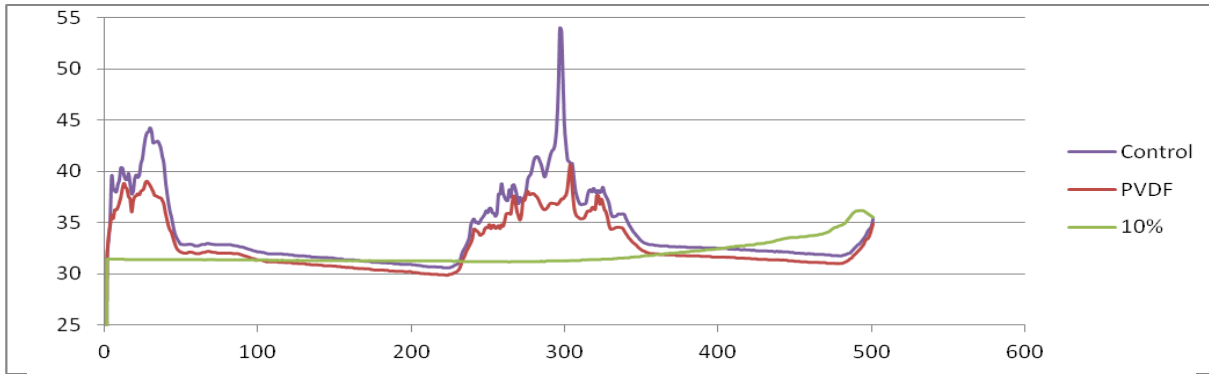


Figure 6. Curves of Temperature ($^{\circ}\text{C}$) against Time (minutes) of inside environment of the coated glass tub.

3.2 Discussion

3.2.1. IR absorption comparison

PAA contains C=O bond, C=C bond and OH bond. It has many absorption frequencies from both stretching and bending vibrations and has a broad range of absorption spectra with a sharp peak at wavenumber of 2400 cm^{-1} as shown in Fig.1.4. PMMA contains C=O bond and C=C bond and OCH₃ bond. It has many sharp peaks between the range of 2000 cm^{-1} to 1000 cm^{-1} and another one at 3000 cm^{-1} as shown in Appendix Fig.2. PAN has C≡N bond which has sharp absorption spectra from 2240 cm^{-1} to 2260 cm^{-1} . Creating co polymer which has combined absorption spectra will be effective and more feasible than coating a film of monomers three times. As shown in Appendix Fig.1., The polymer $(\text{H}_2\text{NB}_2\text{F})_n$ displays IR absorption range at 450 cm^{-1} to 20 cm^{-1} . By making the film thicker, we will be able to efficiently block out the FIR of the sunlight which contributes in heating considerably. Previously, $(\text{H}_2\text{NB}_2\text{F})_n$ has been made before [1] but the results were not as pure as the polymer we have attained.

3.2.2. Composite films

PVDF was added to the $(\text{H}_2\text{NB}_2\text{F})_n$ because of its durability and stability that is compatible with $(\text{H}_2\text{NB}_2\text{F})_n$ and will allow the resulting film to withstand extreme weather conditions. Also, it has 96% transmittance of visible spectra. Upon making the 10% and 15% solutions in DMF, it was observed that the optimal concentration of $(\text{H}_2\text{NB}_2\text{F})_n$ was 10%, as the 15% solution lacked the viscosity that allowed even coating of the solution in order to produce a homogeneous film. $(\text{H}_2\text{NB}_2\text{F})_n$ is also known to only dissolve partially in DMF, which may have contributed to such observation [2]. The film, when first casted on a glass surface, appeared milky white, and upon heating to about $120\text{--}150^{\circ}\text{C}$, turns transparent. This phenomenon is a result of our polymer solution's phase behavior. When a certain temperature is applied, it undergoes a phase change due to the change in energy that leads to a smaller particle size.

3.3. IR filtering performance

As observed from figure 6, the temperature change in the test tube coated with the 10% changed the least followed by 15%, PVDF and the control. This shows that the Aminodifluoroborane film had absorbed some of the infrared radiation as predicted. The film containing a higher concentration of Aminodifluoroborane absorbed infrared radiation less effectively; this is mostly probably due to the uneven application of the solution in the process of coating the test tubes, leaving loop holes. The low viscosity weakens the surface tension and encourages the liquid to form smaller bubbles onto the surface, instead of a uniform surface all around the tube. Thus, when dried,

the resulting film will not cover some patches of the test tube surface, from which the infrared radiation will penetrate and heighten the temperature of the atmosphere within.

4. Conclusion

By applying a thin layer film containing polymeric aminodifluoroborane on glass windows domestically or industrially, we can reduce the amount of IR passing through the windows, while allowing most visible light to penetrate. These results in less energy spent in cooling and lighting the interior. Also, when casted upon a solar cell and, the infrared radiation absorbing property of the film can prevent solar cells from heating up excessively and increasing its efficiency at the same time.

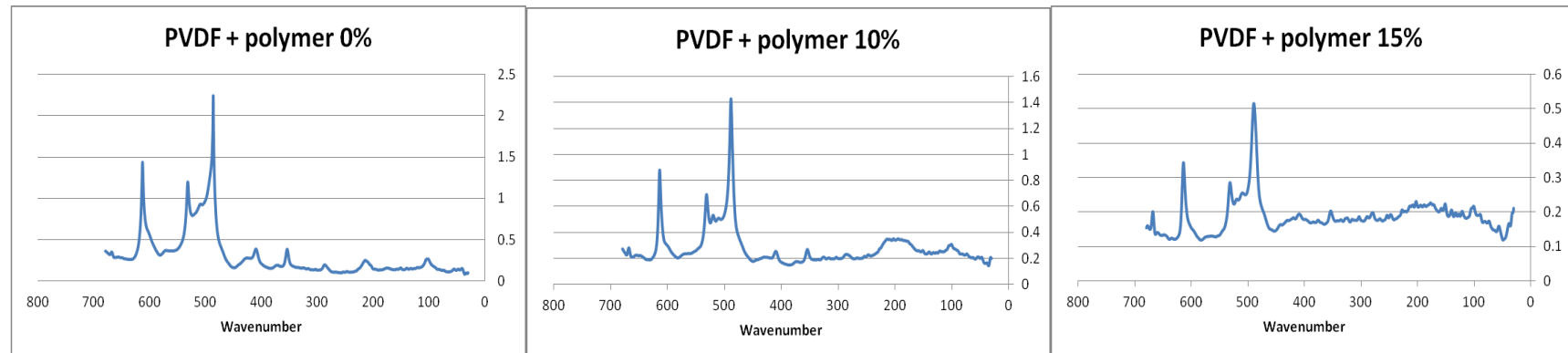
Although the temperature that causes phase change in the film that we have developed is high (120~150°C), further research may be carried out to lower the temperature, which will allow the opacity of the film to be controlled according to the temperature of the environment. Furthermore, the solubility of polymeric aminodifluoroborane in DMF can also be improved upon further research. It will allow production of polymeric aminodifluoroborane solution in higher concentrations and therefore, a more efficient film can be developed.

4. References

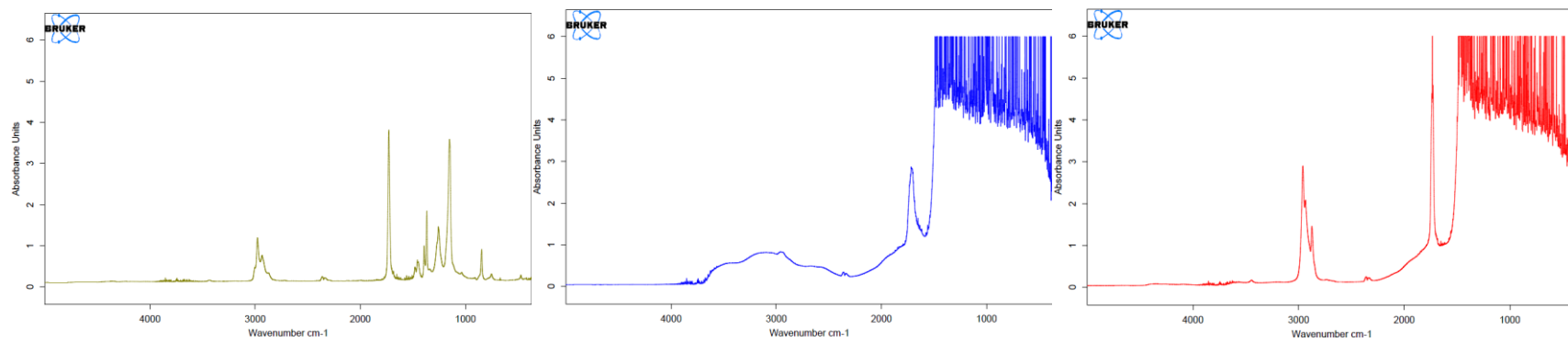
- [1] Rothgery, McGee, Pustacioglu, Inorganic Chemistry, Vol, 14 No.9 (1975) 236-2238
- [2] S.Y. Pusatchioglu, H.A. McGee, JR., A.L. Fricke, J.C. Hassler, Journal of Applied Polymer Science, Vol.21, (1977) 1561-1567
- [3] S.M. Nakhmanson, M.Buongiorno Nardelli, J. Bernholc, Physical Review Letters, Volume 92, Number (2004) 115504-1 – 115504-4
- [4] Udo Schwingerschlögl, Cosima Schuster, Raymond Frésard, Chemical Physics Letters 481 (2009) 62-67
- [5] Enrica Fontananova, Johannes C. Jansen, Alessandra Cristiano, Efrem Curcio, Enrice Drioli, Desalination 192 (2006) 190-197
- [6] André M. Gobin, Min Ho Lee, Naomi J. Halas, William D. James, Rebekah A. Drezek, Jennifer L. West, Nano Letters, Vol. 7, No. 7 (2007) 1929-1934
- [7] Reitzel J, Journal of Chemical Physics, Vol. 23, 2407-2409
- [8] http://www.gaiasaunas.com/about_infrared_energy1.html

Dr. Hong Han has been engaged in the work related to polymer research and development for more than 20 years. He obtained his Ph D from Peking University 1997 and worked in the institutes and university for more than 15year. Now he is working in an industry of polymer resin manufacturing as R&D manager.

Appendix: IR Spectroscopy of Absorption Units against Wavenumber (cm^{-1})



Appendix Fig.1. IR spectra of PVDF + Polymer (BF_2NH_2)_n



Appendix Fig.2. IR spectra of PMMA (free standing film); PAA (with glass) and; PBA (with glass).

Volatile Corrosion Inhibitor (VAPPRO 872)

S. W. Tong¹, L. Y. Yeo Geradine¹, X. L. Quek¹, T. A. Ho¹ and Moe Patrick²

¹Diploma in Materials Science
School of Chemical & Life Sciences
Singapore Polytechnic

²Magna International Pte Ltd Singapore

Abstract: The main objective of this collaborative project was to obtain an optimum formulation from the base formulation of VAPPRO 872, a commercial volatile corrosion inhibitor (VCI) product from Magna International Pte Ltd. Percentages of the corrosion inhibitor (CI) and calcium sulphonate (CS), type of kerosene and type of calcium sulphonate were varied, and the various formulated products were tested for its flammability and viscosity. The different formulations were each coated onto a metal test piece to further test for its corrosion rate using the Electrochemical Impedance Spectroscopy. The results showed that the optimum formulation with the best efficiency was 0.5% CI, 3% “old” CS, 19% mineral oil and 77.5% pure kerosene, with an efficiency of 89.14%. This was chosen because of its relatively high efficiency and reduced costs.

Keywords: volatile corrosion inhibitor; flammability; viscosity.

1. Introduction

Corrosion occurs when a material, usually metal, starts to weaken and its properties become less desirable. This is due to irreversible chemical reactions with the surroundings. Corrosion is a very common problem in many industries, where metals are used in their daily operations and when these machines fail, it costs a large sum of money to replace them. Hence, we are working on Vapro 872 (VCI) with the assistance from Magna International Pte Ltd.

Magna International specializes in corrosion preventive technology and cleaning surfactants, and they have developed an advanced and environmentally safe VCI known as Vapro, which stands for Vapor – Phase – Protection. This range is commonly used in the electronics and automotive industry, as well as in the military.

Vapro 872 is a VCI aerosol that is used in the disassembly and assembly of machines, pipes, valves, bolts and nuts etc. It works by penetrating into the metal to reduce corrosion or formation of rust, as well as allowing the moving parts to be lubricated continuously [1]

2. Experimental Section

2.1. Materials

Corrosion inhibitor (CI), both old and new calcium sulphonate (CS), odourless kerosene and mineral oil (MO) were kindly provided by Magna International Pte Ltd. Pure kerosene was purchased from the company, Sigma Aldrich.

2.2. Equipment

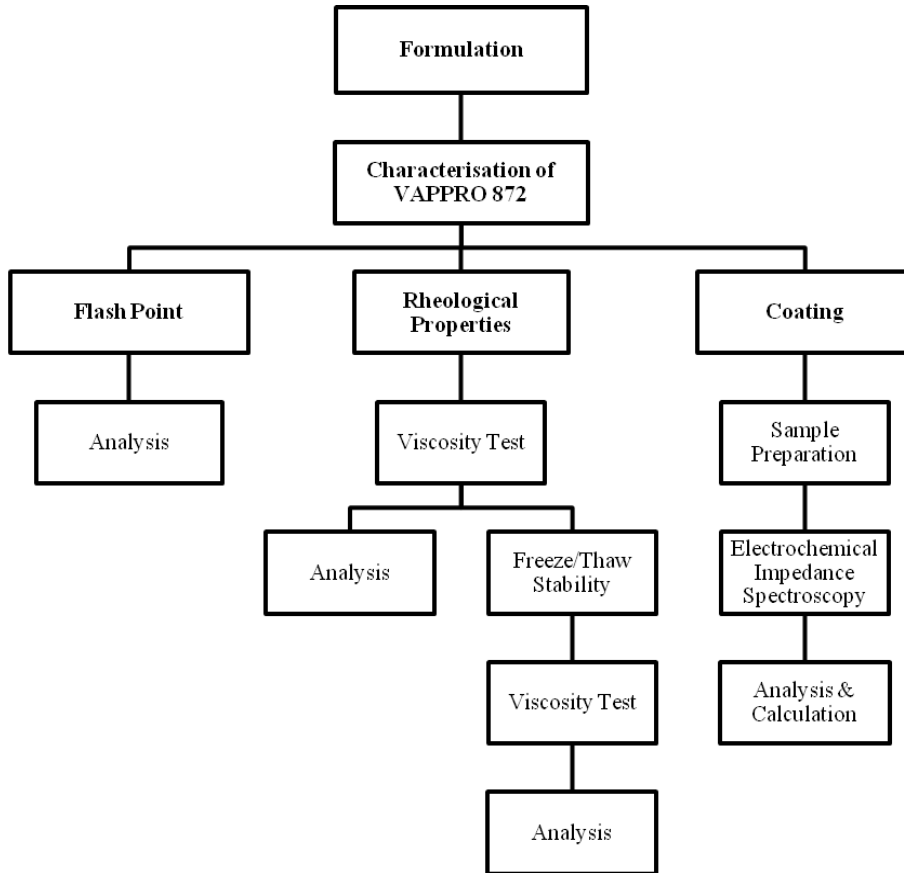
The equipment used to characterize the formulations were the Grabner MiniFlash Touch, to measure flash point, Brookfield DV-E Viscometer Model no. RVDVE230, to measure viscosity, and Zahner Zennium Electrochemical Impedance Spectroscopy (EIS) to measure corrosion rate of the metal test pieces.

2.3. Methods

2.3.1. Preparation of Formulations and Test Pieces

During formulation, different amounts of corrosion inhibitor, mineral oil, calcium sulphonate (old/new) and kerosene (odorless/pure) were weighed (in grams) and mixed uniformly with a magnetic stirrer. The formulations were decanted for at least 24 hours before testing or coating. The test pieces used are made of mild steel, measuring 10cm x 2.5cm. They were polished with abrasive paper to remove surface rust, washed with deionised water and wiped dry. It was fully immersed in 20 ml of the desired formulation, and left to dry at room temperature in the fume hood for 24 hours before undergoing EIS testing.

Figure 1: Overview of Experiments Conducted



2.3.2. Flash Point

After transferring 1 ml of the desired formulation into the cleaned sample holder of the machine, Grabner MiniFlash Touch. With reference to ASTM D 56 Standard Test Method for flash point [2], the following parameters were used while conducting the test:

- Ignition Interval: 1°C per
- Ignition Time: 15ms
- Air Ventilation: 0.6s
- Heating Rate: 5.5 °C per minute
- Starting Temperature: 30 °C

2.3.3. Rheological Properties

After undergoing a viscosity test using Brookfield Viscometer, with reference to ASTM D2243-95 Standard Test Method for Freeze-Thaw Resistance of Water-borne Coating [3], the formulations were stored in a freezer for 17 hours at -30°C, then 7 hours at room temperature. This cycle was repeated 3 times before running a viscosity test again.

2.3.4. Electrochemical Impedance Spectroscopy (EIS)

The EIS was set up with the corresponding electrodes:

- Auxiliary/counter electrode (CE) – Platinum Electrode
- Reference electrode (RE) - Calomel Electrode
- Working electrode (WE) – Test Piece

The coated test piece was submerged into tap water and the test carried out with the following parameters:

- Potential Voltage: 4V and -4V
- Current range: -2A and 2A
- Scan Rate: 10V/s
- Potentiostat: OFF
- Check Cell Connection: 3 electrodes
- Reference Electrode Potential: Calomel/sat.KCl

From the interception on the graphs produced, the corrosion current density was used obtained to calculate the corrosion rate, in mm/year, of the metal pieces using the following formula:

$$\text{Corrosion Rate} = K \frac{a \times i_{corr}}{n \times D}$$

Where a : atomic weight, i_{corr} : corrosion current density, $\mu\text{A}/\text{cm}^2$,
n : number of electrons lost (valence change), D : density, g/cm^3 K: a constant depending on the unit of corrosion rate

3. Results & Discussion

In order to study what effect each component has on the corrosion rate by varying the percentage of CI, percentage and type of CS and type of kerosene. In addition, the physical properties such as viscosity, flash point, and freeze thaw stability will be presented. Finally from all the above variations, an optimum formulation is deduced.

3.1. Our formulations

Refer to Table 1 for base formulation and Tables 2 and 3 for the varied formulation.

Table 1: Base Formulation

| Mineral Oil | CI | “Old” Calcium Sphonate (OCS) | Odorless Kerosene |
|-------------|----|------------------------------|-------------------|
| 19% | 1% | 3% | 77% |

Firstly, the only concentration of CI (CI1 – CI5) was varied. Following that pure kerosene replaced odorless kerosene and different concentration of CI (CI6 – CI10) was used.

Table 2: Different CI Concentration Used With Odorless Kerosene Base and Pure Kerosene Base

| | CI1 | CI2 | CI3 | CI4 | CI5 | CI6 | CI7 | CI8 | CI9 | CI10 |
|--------------|-----|------|-----|------|-----|-----|------|-----|------|------|
| % of CI used | 0.1 | 0.25 | 0.5 | 0.75 | 1.0 | 0.1 | 0.25 | 0.5 | 0.75 | 1.0 |

Table 3 illustrates the different variation of OCS and “new” Calcium Sulphonate (NCS) used.

Table 3: Different Percentages of OCS and NCS Used

| | OCS1 | OCS2 | OCS3 | NCS1 | NCS2 | NCS3 |
|---------------|------|------|------|------|------|------|
| % of OCS used | 1 | 3 | 9 | 1 | 3 | 9 |

3.1.1. Effect of CI Concentration (%) on Corrosion Rate Using Odorless Kerosene and Pure Kerosene

All corrosion rates were determined by means of EIS, and expressed as mm/year. However, it can be expressed as percentage efficiency (% efficiency) for a more accurate representation of the product’s effectiveness, which is given by:

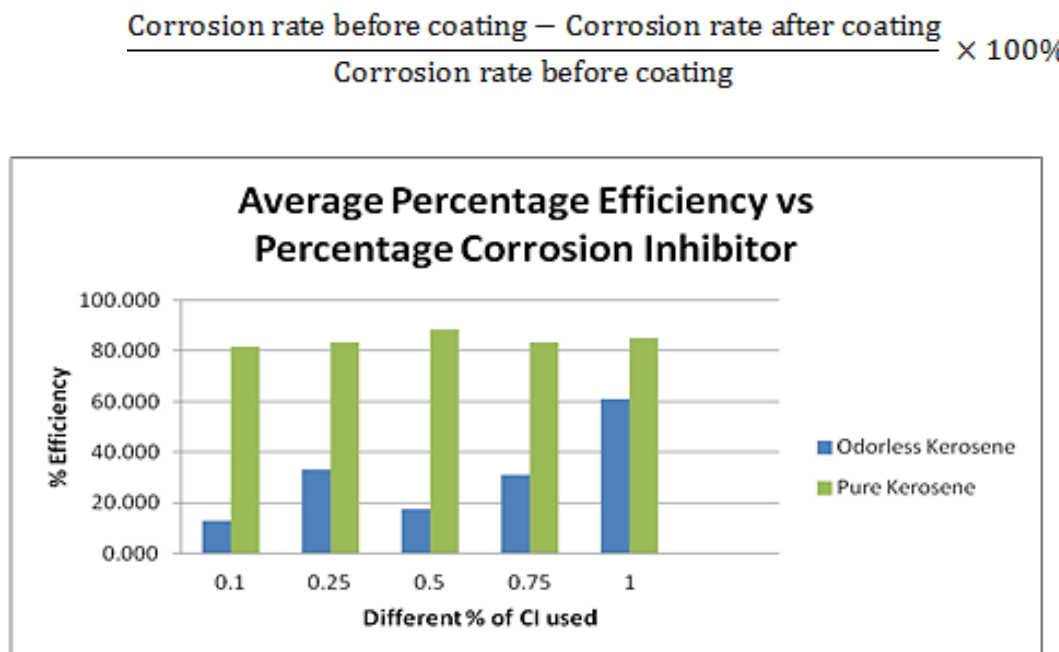


Figure 2: Comparison of Average % Efficiency and CI Concentration in terms of percentage with odorless kerosene and pure kerosene

From the Figure 4-1 above, it shows that 1% and 0.5% corrosion inhibitor yield the lowest corrosion rate (i.e., highest % efficiency) for odorless and pure kerosene respectively. Overall, pure kerosene shows more significant results in preventing corrosion as compared to odorless kerosene. Theoretically kerosene contains various compounds that give it its pungent and toxic smell. These compounds are olefins, H₂S, mercaptan, odourless or thiophenic sulphur compounds or nitrogenous compounds that vaporize easily at room temperature. Hence processing it via hydrodesulphurization or other methods of hydrotreatment allows certain amounts of the olefins, sulphurous and nitrogenous compounds to be removed, producing odourless kerosene. This could be the reason for the lower efficiency of odourless kerosene as certain compounds which are crucial for penetrating the metal piece, to prevent it from corroding, has been processed off and led to the higher average % efficiency of pure kerosene.

| CI1 | CI2 | CI3 | CI4 | CI5 | CI6 | CI7 | CI9 | CI10 | CI8 |
|---------|-----|-----|-----|-----|--------|-----|-----|------|-----|
| (Worst) | | | | | (Best) | | | | |

Figure 3: Increasing Average % Efficiency with Different Concentrations of CI Using Odorless and Pure Kerosene

However, due to different concentration of certain compounds contained inside pure kerosene, it shows that 0.5% CI result in the best average % efficiency for pure kerosene instead of following the trend (as the concentration of CI increases, the rate of corrosion decreases) which was reflected in odorless kerosene . Hence, the CI8 formulation is the best while CI1 is the worst (refer to the following Figure 3).

3.1.2. Effect of Type of CS and Its Concentration (%) on Corrosion Rate

Two batches of CS (OCS and NCS) were used. The new batch of CS (NCS) was observed to be finer and has a darker colour as compared to the old batch of CS (OCS). The quantity of new and old CS added to the pure kerosene formulation varies at 1%, 3% and 9% concentration level.

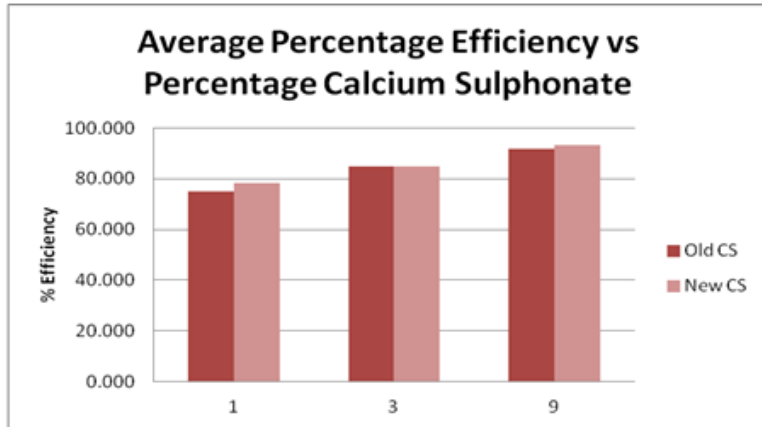


Figure 4: Comparison of Concentration of CS and Effectiveness between OCS and NCS in Reducing Corrosion Rate

The amount of CS was increased three fold in OCS3 and NCS3 while decreased three fold in OCS1 and NCS1 so as to compare the corrosion rate with the base formulation OCS2 and NCS2. The bar chart above displays the effectiveness of CS in reducing corrosion rate of the sample. By increasing % concentration of CS results in increasing average % efficiency of the sample. This is because of the better penetration ability of the CI and good wetting and adhesion to the metal's surface. No conclusion is drawn on which “type” of CS is better since at specific concentration (e.g. 1%), NCS shows better results in the average % efficiency but say otherwise when the concentration is 3%. Thus, the “ranking” chart based on CS’s effect on the corrosion rate is shown below:

| OCS1 | NCS1 | NCS2 | OCS2 | OCS3 | NCS3 |
|---------|------|------|--------|------|------|
| (Worst) | | | (Best) | | |

Figure 5: Increasing Average % Efficiency with Different Concentrations of Old and New CS Using Pure Kerosene

3.2. Optimum Formulation

3.2.1. Kerosene as Base Solvent

Figure 6 below is used to display the steps taken to deduce the optimum formulation. Firstly, the concentration of CI affecting the average % efficiency was studied using odourless and pure kerosene. The resulting formulation which gives the best average % efficiency was derived using pure kerosene. Using pure kerosene, a series of testing using different concentrations of OCS and NCS affecting the corrosion rate was conducted.

3.2.2. Biodiesel as Base Solvent

Since kerosene is classified as a flammable and volatile liquid, it poses direct and indirect threat to the human and the environment. It has varying toxicity depending on the method and duration of exposure besides potential fire hazards. Its volatile organic compound has an indirect impact contributing to ozone depletion and global warming due to the chlorofluorocarbons such as CF_3Cl and CCl_4 which has a very long shelf life in the atmosphere. Thus, the use of less volatile solvents may be seen as an alternative in improving the environment. However, it is difficult to replace a solvent as there are many aspects to be considered such as the hazardous process, compatibility with current raw materials and its by-products [4].

In recent years, biodiesel has gained popularity due to its availability, non-toxicity, and its biodegradability [5]. With this, it was taken into consideration to replace kerosene with biodiesel as the base solvent for Vapro 872 for its renewability and low vapour pressure. A detailed study has been carried out by another group of APLT (Advanced Diploma in Polymer Technology) students and it has been found that biodiesel can be used as a substitute base solvent for Vapro 872 and their optimum formulation has been used to compare with our optimum formulation. The metal pieces were both immersed in respective base formulations for one day before running EIS on them.

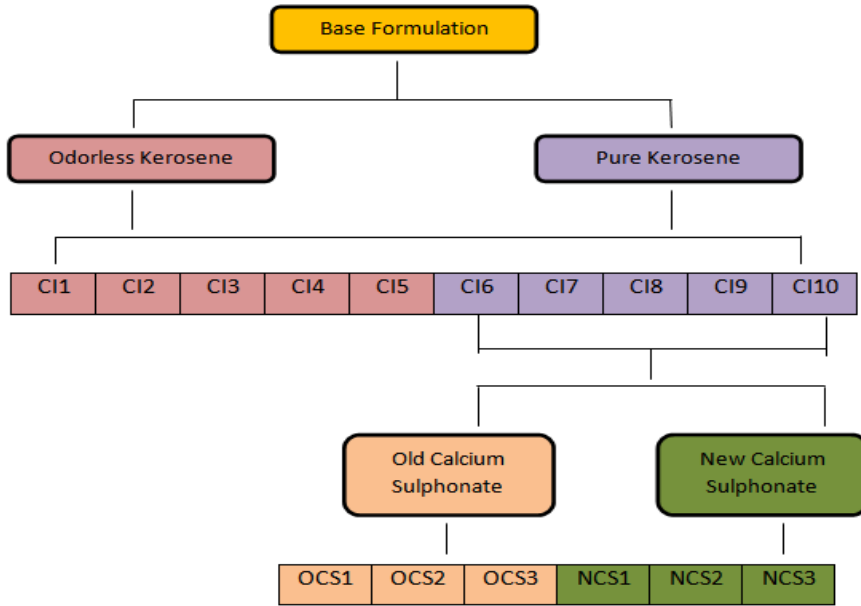


Figure 6: Deduction of Optimum Formulation from Best Average % Efficiency from Raw Materials

Table 8 shows the optimized formulation that has been deduced from this project.

| Mineral Oil | CI | OCS | Pure Kerosene |
|-------------|------|-----|---------------|
| 19% | 0.5% | 3% | 77.5% |

Table 9: Comparison between Raw Materials Used in Two Optimum Formulations Using Pure Kerosene and Biodiesel as Base Solvent

| | Mineral Oil | CI | CS | Base Solvent (Pure Kerosene/Biodiesel) |
|-------------------------------------|-------------|-----|----|---|
| Optimum formulation (Pure Kerosene) | 19% | 3% | 1% | 77% |
| Optimum formulation (Biodiesel) | 19% | 10% | 9% | 62% |

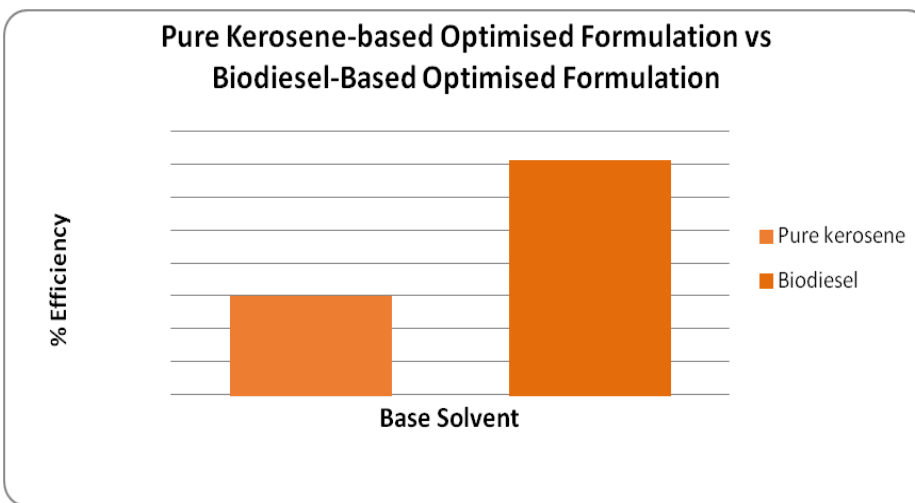


Figure 7: Comparison of the Effectiveness between Pure Kerosene and Biodiesel in Reducing Corrosion Rate

Based on the Figure 7 above, it shows that biodiesel has better average % efficiency than that of pure kerosene. However, biodiesel-based formulation does not comprise of the same concentration of other raw materials. For example, our group used 1% CI and the APLT group uses 10% CI to achieve above average % efficiency. Since the difference between the average % efficiency achieved by the APLT students and our group is not as significant (a difference of 4%) and considering the amount of CI used was tenfold for biodiesel based formulation, it can be concluded that pure kerosene-based optimum formulation could be better than biodiesel-based formulation.

3.3. Physical Properties

Three physical properties, viscosity, flash point and freeze-thaw of our formulated product were tested. The purpose of performing these tests was to check for any significant variation in physical properties if we alter the base formulation. For each formulation, three readings are taken for each set and the average readings were recorded. For all the tests, decanting technique was carried out so that the supernatant layer was used.

3.3.1. Viscosity

It is crucial to measure the viscosity for our product as it predicts the pumpability and pourability performance in a dipping or coating operation, or the ease with which it may be handled, processed or used. Viscosity is often the most susceptible way in finding out the changes in colour, density, stability, solid content and molecular weight.

Table 10: Viscosity for All Formulations

| Formulations | CI1 | CI2 | CI3 | CI4 | CI5 | CI6 | CI7 | CI8 | CI9 | CI10 |
|----------------------|------|------|------|------|------|------|------|------|------|------|
| Viscosity(cP) | 12.3 | 13.0 | 12.1 | 12.7 | 13.5 | 15.3 | 19.1 | 19.1 | 19.0 | 18.9 |
| <hr/> | | | | | | | | | | |
| Formulations | OCS1 | OCS2 | OCS3 | NCS1 | NCS2 | NCS3 | | | | |
| Viscosity(cP) | 16.8 | 18.9 | 17.8 | 16.0 | 18.9 | 17.6 | | | | |

Table 11: Viscosity after Freeze-thaw for All Formulations

| Formulations | CI1 | CI2 | CI3 | CI4 | CI5 | CI6 | CI7 | CI8 | CI9 | CI10 |
|----------------------|------|------|------|------|------|------|------|------|------|------|
| Viscosity(cP) | 15.7 | 12.1 | 12.9 | 17.1 | 19.1 | 20.8 | 20.8 | 18.3 | 19.0 | 15.3 |
| <hr/> | | | | | | | | | | |
| Formulations | OCS1 | OCS2 | OCS3 | NCS1 | NCS2 | NCS3 | | | | |
| Viscosity(cP) | 12.8 | 15.3 | 24.3 | 16.3 | 15.3 | 23.8 | | | | |
| Freeze-Thaw | | | | | | | | | | |

As shown in the Table 10 above, results range from 12.1cP to 19.1cP. Also, it is observed that there is an increase in viscosity for pure kerosene-based formulations as compared to odourless kerosene-based. This range is still acceptable when compared to Magna's original formulation of VAPPRO 872, and implies that the variations formulation are able to be made into an aerosol spray which can be easily applied and ejected from the spray nozzle without clogging or causing any blockages. However, the variation in the viscosity is not great and thus this factor will not have a significant effect on the performance of our product.

The deviations of the results of the viscosity test after freeze-thaw were not that significant, with a range of 12.3 cP -19.1cP before freeze-thaw (difference of 6.8cP) (refer to Table 10) to 12.1cP – 24.3 cP after freeze-thaw (difference of 12.2cP) (refer to Table 11). Nevertheless, one possible reason for the slight difference in viscosity after freeze-thaw could be due to the agglomeration of CS that was settled to the bottom. Despite vigorous shaking of the bottle, minute agglomerates of CS were still present. Still, the viscosity readings after freeze thaw are considered acceptable as the product is still flowable by (visual observation).

3.2.2. Flash Point

Table 12: Flash Point for All Formulations

| Formulations | CI1 | CI2 | CI3 | CI4 | CI5 | CI6 | CI7 | CI8 | CI9 | CI10 |
|-------------------------|------|------|------|------|------|------|-----|-----|-----|------|
| Flash Point / °C | 49 | 50 | 50 | 50 | 50 | 80 | 81 | 80 | 80 | 80 |
| Formulations | OCS1 | OCS2 | OCS3 | NCS1 | NCS2 | NCS3 | | | | |
| Flash Point / °C | 80 | 79 | 80 | 80 | 80 | 80 | | | | |

With reference to the Table 12 above, odourless kerosene-based formulations shows flash points ranging from 49°C to 50°C which is categorised under high to moderate hazard. However, pure kerosene based formulations result in a range of 79°C to 81°C for flash point which is a much safer alternative solvent to be used as compared to odourless kerosene since it has a lower potential for fire hazards, easier handling and storage.

3. Conclusion

From this project, the following can be concluded when comparing the various formulations:

- Changing the base solvent from odourless to pure kerosene had the most impact on the performance on VAPPRO 872.
- Type of CS has an insignificant effect on the performance of the VAPPRO 872.

It can also be concluded that the optimum formulation was CI8. This was due to:

- A decrease in CI without any changes in percentage of OCS as compared to the base formulation (VAPPRO 872), hence making the product more cost effective.
- High % efficiency of 88.3% and excellent corrosion resistance.
- A viscosity of 19.1cP, where it is flowable and easily applied.
- Flash point was 80°C, and is rated as a moderately low hazard product.

4. References

- [1] Magna: <http://www.magnachem.com.sg>
- [2] ASTM D 56 for Flash Point
- [3] ASTM D2243-95 Standard Test Method for Freeze-Thaw Resistance of Water-borne Coating
- [4] Dr. Chris Rayner: Green Solvents. Fundamentals and Industrial Applications, 2010. www.pinetwork.org/pubs/C_Rayner.ppt
- [5] Fengxian Qiu, Yihuai Li, Dongya Yang, Xiaohua Li and Ping Sun: Biodiesel production from mixed soybean oil and rapeseed oil. [Applied Energy](http://www.sciencedirect.com/science/article/pii/S0360531011003307), 88, 6, 2050–2055 (June 2011).

Optimisation and Characterisation of commercial water-based volatile corrosion inhibitor (VCI)

H. Y. Lim Bryan¹, S. B. Low Alex¹, T. M. Cheang¹, T. A. Ho¹ and Moe Patrick²

¹Diploma in Materials Science
School of Chemical & Life Sciences
Singapore Polytechnic

²Magna International Pte Ltd
Singapore

Abstract: Volatile corrosion inhibitor (VCI) provides excellent protection for metal surfaces. VCI molecules attach themselves to metal surfaces to form an invisible thin film (only a few molecules thick), thus keeping moisture at bay. Through this project, the characteristics and effectiveness of a commercially available water-based VCI (Vapour-Phase-Protection, VAPPRO 837C) will be evaluated. The main scope of the project is to characterise the rheological and corrosion reduction properties of the VAPPRO 837C with varying formulations and processing parameters (coating and drying times). Applying the VCI on the metal specimens is done by dip-coating. In addition, the corrosion reduction efficiency of the VCI is evaluated through the use of Electrochemical Impedance Spectroscopy to determine the corrosion rate of the uncoated and coated samples. The most effective VCI film was obtained from a 20% VAPPRO formulation using a coating time of 30min and a drying time of 24hr.

Keywords: corrosion inhibitor; Vapour-Phase-Protection; dip-coating.

1. Introduction

Corrosion refers to the degradation or deterioration of materials at the surface. It has always been problematic to metal constructs and tools as degradation or rusting of metals can lead to a weakening of mechanical properties, thereby weakening them. Replacing them outright is expensive and, with resources on Earth becoming more limited, problematic in the long run [2]. Thus, protecting metallic constructs from corrosion is desirable as it is cheaper than replacing the part entirely and prolongs the working life of the product in the field, with many methods to do so currently available such as galvanization and sacrificial metals. One of the most common methods is using volatile corrosion inhibitors (VCIs), which is what this study is about. They are a class of corrosion inhibiting compounds with a finite vapour pressure where the inhibitors are transported to the target metal through space to condense on the metal surface to form a protective film, lowering the corrosion rate of the metal itself. Factors that determine the efficiency of VCIs are the concentration of VCI compounds, the period of exposure and vapour pressure [3]. The main advantages are that it is easy to use and apply VCI onto the metal product and it is able to reach crevices, blind holes and other ‘difficult to reach’ areas. Limitations include being temporary films as they can be removed easily, are used at fairly low concentrations and a higher concentration is needed for the self-healing effect which could increase the cost of using it and corrosion protection may not be the only requirement, with others such as color limitation and film hardness needed. It is due to these factors that they are largely ignored in industrial maintenance coatings [7]. However, alongside corrosion-resistant materials and corrosion protection coatings, corrosion inhibitors are still researched and developed to further lower corrosion rates and to reduce the costs of corrosion [9].

Ammonia was used as a VCI compound to protect immersed and exposed parts of steam boiler circuits at the beginning of the 20th century. By the 1940s, less odorous, safer and more effective substances were used for protection. With more than 1000 types of VCI compounds known today, only a few are used as these are acceptably efficient, cost effective and environmentally friendly [3]. One type of inhibitor used in VCIs is salts of dicyclohexylamine such as dicyclohexyl ammonium nitrite (DCHN) and cyclohexylamine carbonate (CHC) [1]. The VCI provided by Magna International uses amine carboxylate as the inhibitor. It is a salt synthesized by neutralizing carboxylic acid with a blend of amines, with the number of carbon atoms ranging from 1 to 26, with corrosion inhibition increasing with the number of carbon. Other than corrosion inhibition, it is also used for boundary lubrication, emulsification and detergency [8].

Recently, there has been a shift in using water-based VCIs, which are less hazardous to human health and are environmentally friendly, as opposed to oil-based VCIs. By substituting the organic solvent with water as the transport medium, it would lower the levels of volatile organic compounds (VOCs) emitted by VCIs [4]. This study aims to deduce the concentration of the VCI provided by Magna International, Vapro 837C, that can offer the best corrosion protection and under what conditions can this be achieved. The effects of the concentration of inhibitors, coating time, drying time and temperature on its performance are studied and discussed.

Testing the effectiveness of corrosion protection in a laboratory include salt spray test, electrochemical impedance spectroscopy (EIS) and immersion testing. The EIS method was used in the study as it has the advantage of very short test times (about 20 minutes), although interpretation of the results takes some experience [6]. Using the DC polarization method and a three electrode arrangement, the corroding electrode (metal sample) potential and impedance can be measured with respect to the reference electrode, regardless of the counter electrode's nature. [5] However, EIS is limited when it comes to the high frequency regions, and the development of microelectrodes via photolithography can reach higher frequencies [6]. New robust and accurate reference electrodes to extend active corrosion protection to areas such as high-temperature systems are also being researched [9].

Viscosity tests were carried out in order to determine the rheological properties of the formulation. Rheological properties are important to understand how the formulated product will behave during storage and application.

2. Experimental Section

2.1. Preparation of metal samples

The metal samples were manually de-rusted by hand using 1200 grit abrasive paper. The samples were then washed under deionised water to remove debris from the de-rusting procedure. The dimensions of the metal samples were measured for purposes of calculating their surface area.

2.2. Determination of corrosion rate of uncoated metal samples

The Zahner Zennium Electrochemical Impedance Spectroscopy (EIS) was set up as follows:

- Blue/Black Working Electrode: Sample
- Green Black Reference Electrode: Calomel
- Red Counter Electrode: Platinum

The set-up of the EIS can be seen in Figure 2.2.1 shown below.

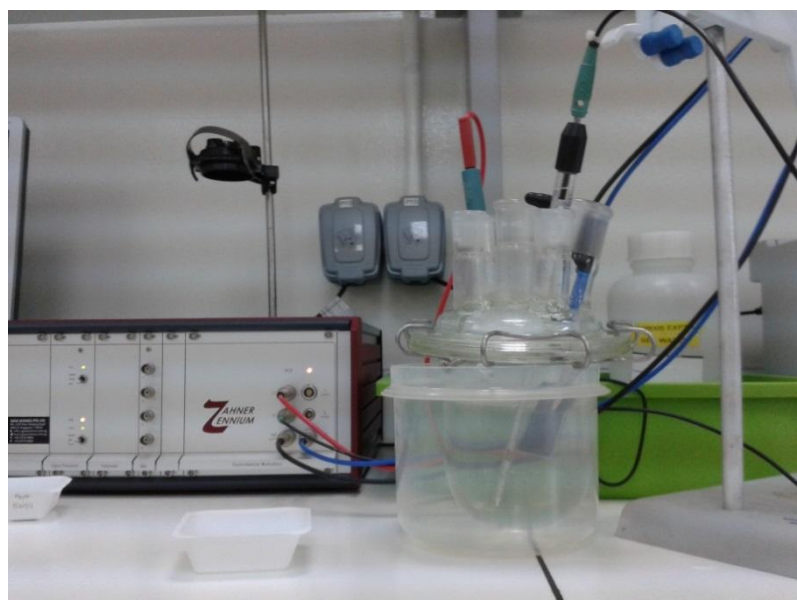


Figure 2.2.1: Set up of EIS with electrodes

The EIS programme was started and the IE/CV option was selected. The following parameters were then entered into the programme:

- Potential Voltage: 4V and -4V
- Current Range: -2A and 2A
- Scan Rate: 10mV/s
- Potentiostat: OFF
- Check Cell Connections: 3 Electrodes
- Reference Electrode Potential: Calomel/sat. KCL

The EIS glass jug was filled with tap water and the uncoated metal samples were attached to the crocodile clips on the blue and black working electrode. The test was then commenced by pressing the “start recording” button. After the test was completed, the tafel plot was then printed and the uncoated metal samples were then de-rusted again.

A pair of tangents was then drawn on the tafel plot as shown in Figure 2.2.2 and the current corresponding to the intersection of the tangents was used to obtain the corrosion current density.

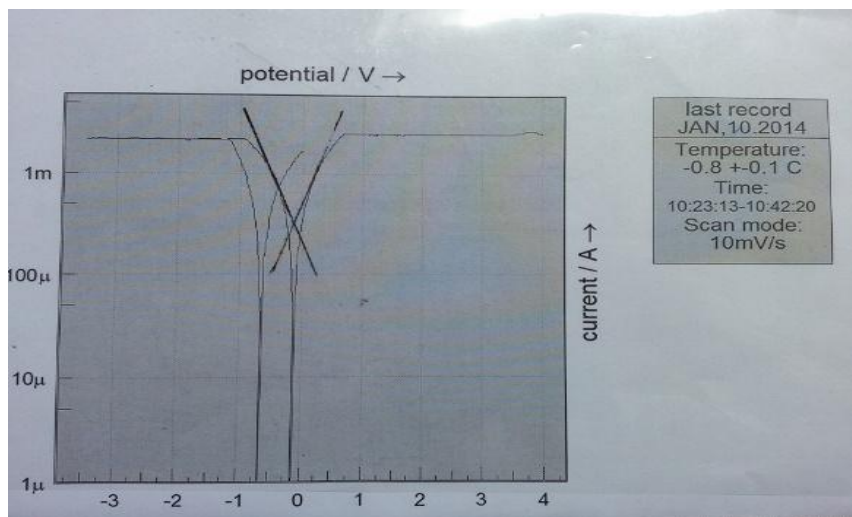


Figure 2.2.2: Tafel plot

The corrosion rate of the sample was then calculated using the following formula:

$$\text{Corrosion Rate} = k [(a \times i_{corr}) / (n \times D)]$$

Where ‘D’ is density of metal specimen, ‘a’ is atomic weight, ‘icorr’ is corrosion current density, ‘n’ is the number of electrons lost and ‘k’ is the constant, which depends on unit of corrosion rate, as listed below. For this project, the ‘k’ value applied was 0.00327mm/ μ A-cm-year.

2.3. Formulation of VAPPRO 837C

A clean blue cap bottle is first placed on an analytical balance and the reading was tare. The required mass of CORPPRO (inhibitor in concentrated form) was added to the bottle using a disposable dropper. After which the required volume of deionised water was added to the bottle. The contents of the bottle were then mixed at about 200rpm using a magnetic stir bar until the mixture had a uniform appearance. The bottles are then labelled and then left to stand for one day before being used for tests.

2.4. Coating of metal samples

Using a disposable dropper, 20ml of formulated VAPPRO 837C VCI were added to a watch glass. The de-rusted metal samples that have been tested with the EIS were then immersed in the watch glass for a specified period. The metal samples were then removed using tweezers and clipped onto a string held taut between two retort stands.

The metal samples were left to dry for a specified period. Immediately after drying, the metal samples were tested using EIS and their corrosion rates were calculated.

2.5. Determination of Corrosion Reduction Efficiency

Based on the corrosion rates of the metal sample before and after coating, the corrosion reduction efficiency is calculated based on the formula below:

$$\text{Reduction Efficiency (\%)} = (\text{CR uninhibited} - \text{CR inhibited}) / \text{CR uninhibited} \times 100$$

Where:

CR uninhibited = Corrosion rate of uninhibited sample

CR inhibited = Corrosion rate of inhibited sample

2.6. Elevated temperature drying

The set-up shown in Figure 2.6.1 was used for the elevated drying temperature test. The light bulb was first switched on to heat up the interior of the box. When the temperature inside the box stops fluctuating, metal samples that have just completed coating were clipped onto the string for drying over a specified period. After drying, the samples were immediately tested using the EIS to determine their corrosion rates.

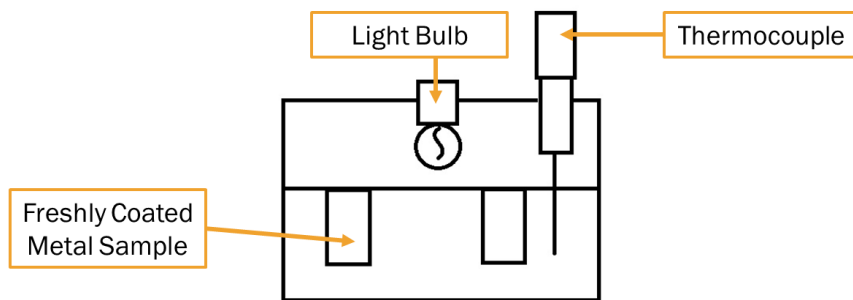


Figure 2.6.1: Elevated temperature drying set-up

2.7. Viscosity test

The Brookfield DV-E Viscometer was set up with spindle 1 and a speed of 100rpm. A 500ml beaker was filled to approximately two-thirds with the formulation to be tested. The spindle was then lowered into the formulation until the marking on the spindle was submerged. The rotor was then switched on and left to run. Once the viscosity range have stabilised, the upper viscosity limit was recorded.

2.8. Freeze-thaw test

The freeze thaw test was conducted following the ASTM D2243-95(2008) standard. The formulations to be tested were first tested for their initial viscosity (before freezing). The formulations were then stored at -18°C in a freezer for 17 hours. After 17 hours, the formulations were removed and thawed at room temperature for 7 hours. After thawing, the formulations were placed back in the freezer at -18°C and one more cycle of freeze-thaw was carried out. After the final thawing step was completed, the formulations were tested for their viscosity. The viscosity before and after freeze-thawing were compared to determine the freeze-thaw stability of the formulations.

2.9. Contact angle test

The metal sample to be tested was placed on the stage of the goniometer. A droplet of deionised water was then released from the syringe attached to the goniometer. Once the droplet's shape has stabilised, the computer software was used to measure the contact angle. The test was repeated on separate areas of the metal samples and the average contact angle was calculated.

2.10. pH tests

The pH test was conducted using a Eutech pH/Ion 510 bench top meter on the formulations. A beaker was first partially filled with the desired formulation. The pH probe was then immersed in the formulation. When the pH

reading has stabilised, the pH reading was recorded. The test was repeated to obtain additional readings and the average pH reading was then calculated.

2.11. Functional group analysis using FTIR

The FTIR test was conducted on a sample of the 20% CORPPRO formulation using the Attenuated Total Reflectance (ATR) method. A background scan was first carried out. After which, 2-3 drops of the formulation was added onto the diamond surface using a disposable dropper. The formulation was then scanned, and the resulting spectrum was analysed.

3. Results and discussions

3.1. Effects of varying concentration of CORPPRO on Corrosion Reduction Efficiency

Varying the concentration of CORPPRO, it was observed that 20% CORPPRO obtained the highest corrosion reduction efficiency compared to 10% and 30% CORPPRO. The 20% CORPPRO formulation obtained a corrosion reduction efficiency of 81%, 75% and 76% for 30min, 8hr and 24hr coating times respectively, as shown in Figure 3.1.1 below.

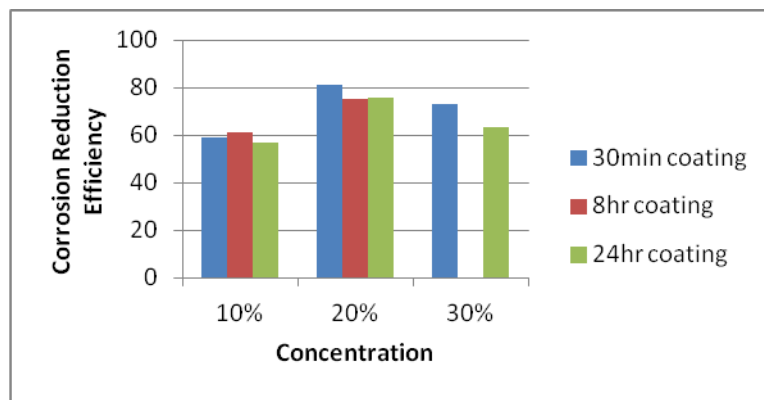


Figure 3.1.1: Effects of varying concentration on corrosion reduction efficiency for different coating times

3.2. Effects of varying concentration of CORPPRO on Corrosion Reduction Efficiency

| CORPPRO concentration (%) | Corrosion Reduction Efficiency (%) | | |
|---------------------------|------------------------------------|--------------------|----------------------|
| | Copper substrate | Aluminum substrate | Mild steel substrate |
| 10 | 34 | 31.5 | 57 |
| 20 | 45.5 | 66.5 | 76 |
| 30 | 37 | 59 | 63.5 |

Table 3.2.1: Effect of varying concentrations of CORPPRO on corrosion inhibition efficiency of different metal substrates (24hr coating, 24hr drying)

Through varying the concentration of CORPPRO, it was observed that the 20% CORPPRO formulation obtained the highest corrosion reduction efficiency for all three substrates. This can be seen from the 20% CORPPRO formulation obtaining 45.5%, 66.5%, and 76% for copper, aluminium and mild steel substrates, as shown in Figure 3.2.2 below.

By coating the different metal substrates, it was observed that the mild steel substrates obtained the highest corrosion reduction efficiency. This can be seen from the mild steel samples obtaining a corrosion reduction efficiency of 57%, 76% and 63.5% for 10%, 20% and 30% CORPPRO formulations, as shown in Figure 4-3 below.

The copper substrates obtained lower corrosion reduction efficiency of 35%, 45.5% and 37% for 10%, 20% and 30% CORPPRO formulations. This suggests that CORPPRO is able to provide excellent corrosion protection for ferrous metals, but is only able to provide moderate corrosion protection to copper. This does not fully agree with information obtained from Mulcco Singapore Pte Ltd's which states that VAPPRO 837C is able to provide excellent corrosion resistance to copper and iron substrates.

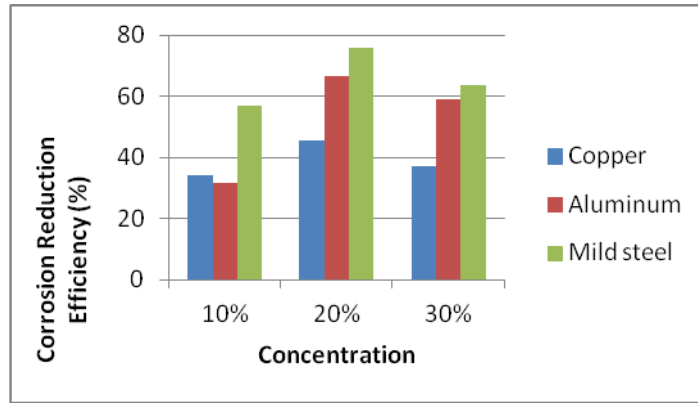


Figure 3.2.2: Effect of varying concentration of CORPPRO on corrosion reduction efficiency of different substrates

3.3. Optimum concentration of CORPPRO

From the results shown in Figure 3.1.1, it can be seen that 20% CORPPRO has the highest corrosion reduction efficiency when compared to 10% and 30% for 30min, 8hr and 24hr coating times. This supports the optimum concentration of 20% suggested to our group by Magna International.

From Figure 3.2.2, it can be seen that the corrosion reduction efficiency for 20% CORPPRO is the highest compared to the 10% and 30% CORPPRO formulations when used on all the different substrates (copper, aluminium and mild steel).

Therefore, 20% CORPPRO would be the optimum concentration to be used because it is able to achieve the highest corrosion reduction efficiency for all three types of metal substrates.

3.4. Effects of varying coating time on corrosion reduction efficiency

Through varying the coating time of CORPPRO, it was observed that the corrosion reduction efficiency of the formulations remained high (75% and above) after 30min of coating time. This can be seen from 20% CORPPRO formulations which obtained a corrosion reduction efficiency of 48%, 33%, 81%, 75% and 76% for 10min, 20min, 30min, 8hr and 24hr coating times respectively, as shown in Figure 3.4.1 below. This suggests that increasing the coating time beyond 30min has no significant effect on the corrosion reduction efficiency compared to a coating time of 30min.

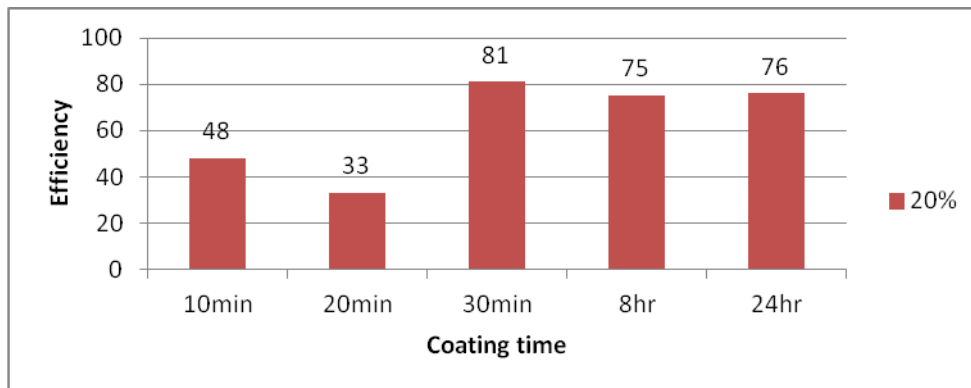


Figure 3.4.1: Effect of varying coating time on corrosion reduction efficiency for 24hr drying on mild steel substrate

This could be because at 30min the surface of the metal substrate is fully saturated with inhibitor molecules and the metal surface-inhibitor interactions have stabilised. Therefore any further coating time would not cause a decrease in corrosion, while a lower coating time would result in the substrate's surface not being saturated with inhibitor molecules which correlates to a higher corrosion rate.

Considering the cost of time for a corporation, using a coating time of 30min would be optimum as this would allow a fast processing time without any loss in corrosion inhibition.

3.5. Effects of varying drying time on Corrosion Reduction Efficiency

When using the drying time of CORPPRO as a variable, it was observed that drying times from 1hr to 5hr obtained low corrosion reduction efficiencies while a drying time of 24hr obtained higher corrosion reduction efficiency. This can be seen from 20% CORPPRO formulation obtaining 53.5%, 38%, 22% and 81% for 1hr, 2hr, 5hr and 24hr drying respectively, as shown in Figure 3.5.1 below. However, from visual observation of the metal samples, the coating appeared to be dry after 20min of drying

This could be because while the coating appears to be dry visually after 20min of drying, there could still be some water content present in the film which promotes corrosion. It is also possible that the protective film of inhibitor molecules have not been properly formed for drying times before 24hr. This suggests that the optimum drying time should be around 24hr.

This optimum drying time of 24hr is also conducive for practical consideration of working hours in the industry. It would be easy to keep track of the end of the drying time and ensure that it ends within working hours so that the metals can be stored immediately after drying.

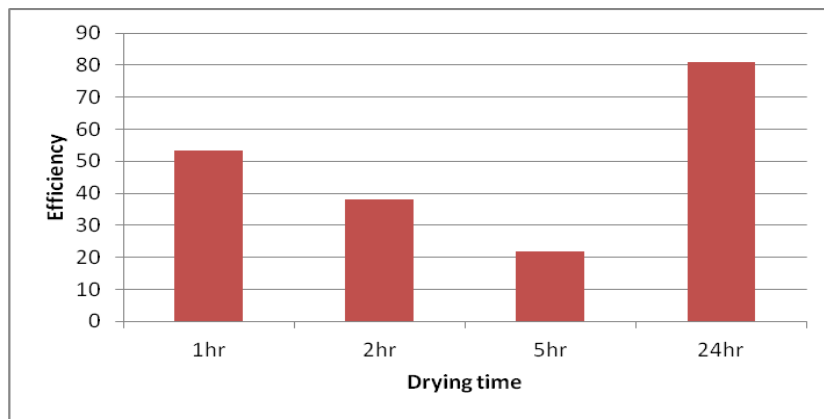


Figure 3.5.1: Effect of varying drying time on corrosion reduction efficiency for 20% CORPPRO, 30min coating time on mild steel substrate

3.6. Effects of drying at elevated temperatures

| Corrosion Reduction Efficiency (%) | |
|------------------------------------|--|
| Temperature (°C) | 20% CORPPRO 30 min coating 2hr room temperature drying |
| 20 | 38 |
| 33 | 58.6 |

Table 3.6.1: Effect of temperature during drying on corrosion reduction efficiency of 20% CORPPRO for 30min coating time

Through varying the temperature of drying, it was observed that drying at an elevated temperature of about 30°C obtains higher corrosion reduction efficiency. This can be seen from the 30°C drying obtaining a corrosion reduction efficiency of 58.6% while the 20°C drying obtained a corrosion reduction efficiency of 38%, as shown in Table 3.6.1 above.

This could be because at elevated temperatures, the inhibitor molecules have more kinetic energy and are more mobile and thus more likely to orient themselves such that the polar functional groups faces the metal surface to preferentially form a protective film over the surface of the metal substrate, therefore resulting in an increase in corrosion reduction efficiency for the metal sample that was dried at elevated temperatures.

After 2hrs drying at elevated temperatures, the surface of the metal sample still appeared wet on visual inspection. This is likely because the box used to contain the samples at elevated temperatures also limited the ventilation to a small area. This would reduce the rate of evaporation of the wet coating layer. Therefore for future testing of drying at elevated temperatures, it would be suggested to carry out the drying in a well-ventilated area.

Compared to samples that were dried at room temperature and not contained in a box but left in a well-ventilated area and had a dry surface on visual inspection, the samples dried at elevated temperatures showed higher corrosion reduction efficiency. This suggests that the corrosion reduction efficiency is not directly related to the water content present in the coated film, but rather on the complete formation of the protective film of inhibitor molecules.

3.7. Viscosity stability tests

| Date | Viscosity (cP) | | | Duration |
|------------|----------------|------|------|----------|
| | C10% | C20% | C30% | |
| 11/1/2013 | 17.2 | 27.1 | 50.3 | Initial |
| 11/8/2013 | 17.5 | 30.1 | 50.1 | 1 Week |
| 11/22/2013 | 16.8 | 31.1 | 50.9 | 3 Week |
| 11/29/2013 | 17.6 | 28.8 | 51 | 4 Week |
| 12/6/2013 | 16.3 | 30.5 | 50.7 | 5 Week |

Table 3.7.1: Effects of storage time on viscosity of formulations with 10%, 20% and 30% CORPPRO concentrations over 5 weeks

By varying the concentration of CORPPRO, it was observed that the viscosity of the formulation increased with increasing CORPPRO concentration. This can be seen from the 10%, 20% and 30% formulations having viscosities around 17cP, 29cP and 50cP respectively, as shown in Table 3.7.1 above. Therefore, viscosity tests could be done as a quality check during manufacturing to ensure that the formulations are of the specified concentrations.

The storage time for 10%, 20% and 30% CORPPRO concentrations were varied and the following observations were made. The viscosity of the formulations remained consistent over a 5-week period, as shown in Figure 3.7.2 below. This would suggest that there is no change in the condition of the formulation throughout the 5 week period. However, further testing is required to determine if viscosity remains constant over time for periods longer than 5 weeks.

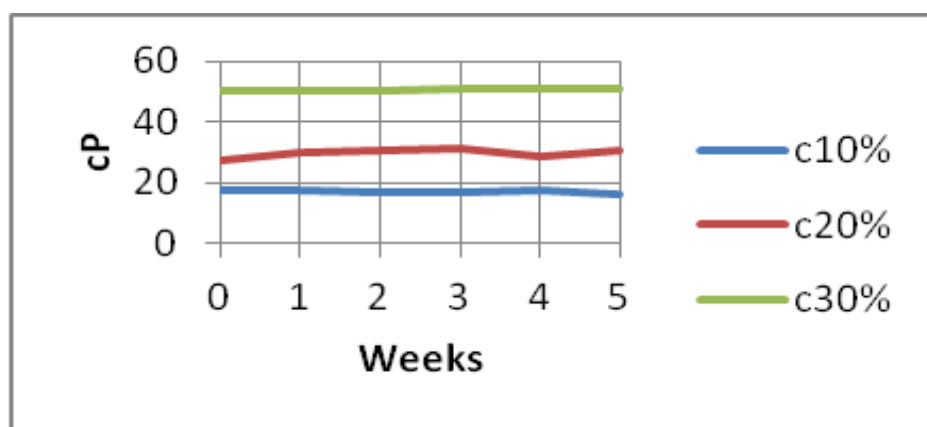


Figure 3.7.2: Effects of storage time on viscosity of formulations with 10%, 20% and 30% CORPPRO concentrations over 5 weeks

3.8. Freeze-thaw tests

| | Viscosity (cP) | | |
|---------------------------------------|----------------|--------------|--------|
| | Before freeze | After freeze | Freeze |
| c20% Freeze Thaw 1 with 1% antifreeze | 28.2 | 30.9 | Yes |
| c20% Freeze Thaw 2 with 1% antifreeze | 29.3 | 28.3 | Yes |
| c20% Freeze Thaw 1 w/o antifreeze | 31.2 | 30.0 | Yes |
| c20% Freeze Thaw 2 w/o antifreeze | 28.0 | 30.6 | Yes |

Table 3.8.1: Effects of freeze-thawing on the viscosity of 20% CORPPRO formulations with and without 1% anti-freeze

By varying the concentration of anti-freeze in the formulations, it was observed that all the formulations froze at -18°C. It was also observed that the viscosities of all the formulations remained around 29cP after undergoing the freeze-thaw test, as shown in Table 3.8.1 above. For all the formulations, there was no significant change in the viscosity after two cycles of freeze-thawing. Further testing is required in order to determine if the viscosity of the formulations will remain consistent after going through more freeze-thaw cycles.

The 20% CORPPRO formulations froze even after the addition of 1% ethylene glycol anti-freeze agent. To prevent the freezing of the formulations at -18 °C, a higher concentration of anti-freeze agent would have to be used.

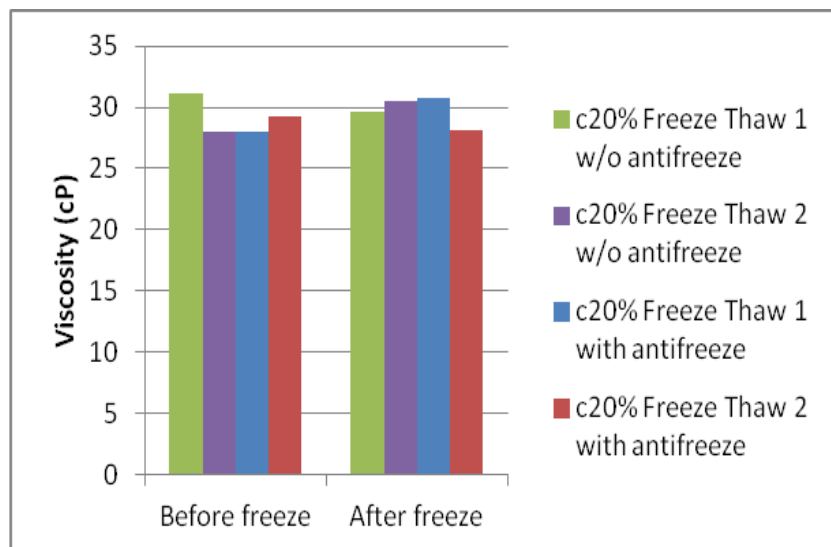


Figure 3.8.2: Effects of freeze-thawing on the viscosity of 20% CORPPRO formulations with and without 1% anti-freeze

3.9. pH test for varying concentration of CORPPRO

| CORPPRO Concentration (%) | Average pH |
|---------------------------|------------|
| 10 | 9.06 |
| 20 | 8.92 |
| 30 | 8.82 |

Table 3.9.1: Effect of concentration of CORPPRO pH of formulations with different concentrations

Through varying the concentration of CORPPRO, it was observed that the pH remained around pH 9 for all concentrations, as shown in Table 3.9.1 above. The MSDS of CORPPRO states that it has a pH of 9, therefore it can be seen that diluting CORPPRO with distilled water does not affect its pH. For all formulations, the pH is below 11 and thus, they will not cause skin irritation.

Since the pH of the formulations does not vary much as the concentration of CORPPRO varies, it would not be viable to use pH as a measure to determine the concentration of CORPPRO formulations during manufacturing. It would be advised to use viscosity instead of pH to determine the concentration of formulations produced during manufacturing.

3.10. Functional group determination by FTIR

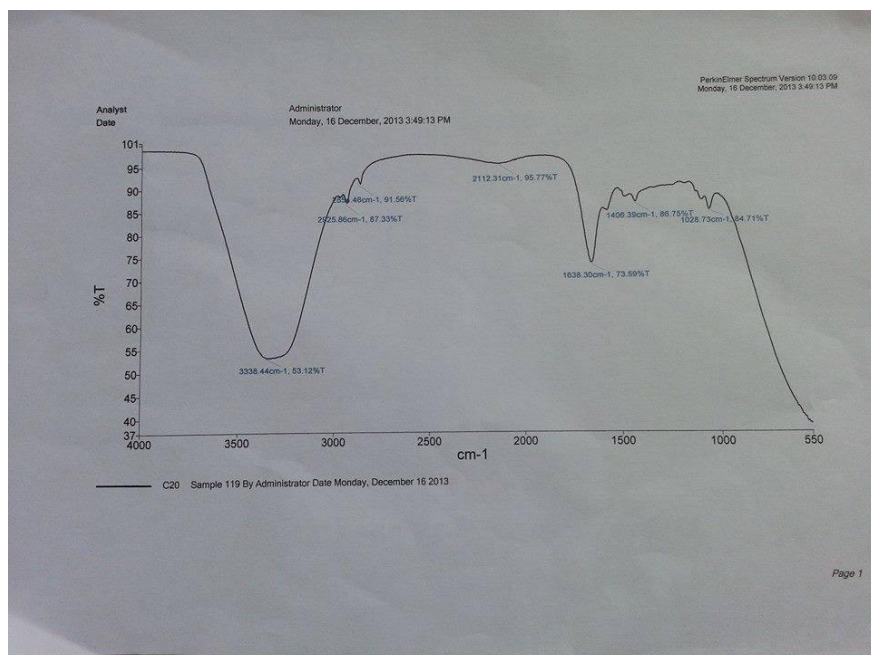


Figure 3.10.1: 20% CORPPRO FTIR spectrum

| Wavenumber (cm^{-1}) | Functional group | Transition |
|---------------------------------|------------------------------|--------------|
| ≈ 3300 | H_2O | -O-H stretch |
| 3000-2850 | Alkanes | C-H stretch |
| 1640-1550 | Primary and secondary amines | N-H bend |

Table 3.10.2: Correlated functional groups of significant peaks in 20% CORPPRO FTIR spectrum

Figure 3.10.1 below shows the FTIR spectrum of 20% CORPPRO. The significant peaks were identified and their correlated functional groups peaks are shown in Table 3.10.2. The spectrum shown in Figure 3.10.1 has a very prominent peak at around 3300 cm^{-1} , this could be due to alkyne C-H stretching. However it is more likely to be due to water -O-H stretching since the formulation contained 80% water. The peaks at 2925 cm^{-1} and 2850 cm^{-1} could be due to carboxylate O-H stretching or alkane C-H stretching. The peak at 1638 cm^{-1} is likely due to alkene C=C stretch or primary/secondary amine N-H bending. The peak at 1406 cm^{-1} is probably due to alkane C-H₃ stretching. The peak at 1028 cm^{-1} could be due to amine C-N stretch or carboxylate C-O stretching.

Based on the absorption peaks present in the spectrum, it is likely CORPPRO contains an organic compound with amine and carboxyl functional groups on a hydrocarbon backbone that contains unsaturated alkene groups. This matches the description of CORPPRO in its MSDS which states that CORPPRO contains “amine carboxylate”.

3.11. CORPPRO interaction with copper substrates

As seen in Figure 4-9, a blue-green stain forms on the surface of the copper substrates. This is probably due to some kind of interaction between the inhibitor molecules and the copper substrate which forms a complex which contains copper (II) ions. The interaction that results in the stain could have caused the copper samples to obtain lower corrosion reduction efficiency compared to mild steel as shown in section 3.2.



Figure 3.11.1: Copper samples drying

3.11. Contact angle test

| Concentration of CORPPRO used for coating | Liquid | Contact angle before coating (°) | Contact angle after coating (°) |
|---|--------|----------------------------------|---------------------------------|
| 10% | Water | 85.8 | Too small to detect |
| 20% | Water | 85.6 | Too small to detect |

Table 3.12.1: Contact angle test result

As seen in Table 4-9, the contact angle of water with the surface of mild steel substrates is about 86°. When a droplet of water is released onto the coated mild steel surface, the contact angle of the droplet to the surface rapidly decreases as the droplet spreads across the coated mild steel surface. When the droplet has stabilised (stopped spreading), the contact angle of the droplet to the coated metal surface is too small for the computer software to detect. This implies that the coating deposited on the mild steel substrate is quite hydrophilic. Therefore it is advised to store coated metals in dry conditions, as the hydrophilic coating could absorb moisture from the air.

4. Conclusions

The optimum concentration for CORPPRO formulations to achieve the highest corrosion reduction efficiency is 20% CORPPRO, as seen in section 3.3. The optimum processing parameters to achieve a short processing time without sacrificing corrosion reduction efficiency for coating mild steel samples are 30min coating and 24hr drying, as seen in section 3.4 and 3.5. The formulations were found to have stable viscosity over a 5 week period. The viscosities were also stable after freeze thawing for two cycles. This would suggest that there is no degradation of the VCI over the 5 week period and from freezing. But further testing is required to determine the amount of anti-freeze required to prevent freezing since the formulations with 1% antifreeze still froze at -18 °C. This can be seen from sections 3.7 and 3.8. We believe this information will be helpful to Magna International when it is assisting its clients.

5. References

- [1] Bayliss, D.A., Deacon, D.H.: Treatment of the Air in 'Steelwork Corrosion Control' CRC Press, 174 (2003).
- [2] Fontana, M.G.: Corrosion Engineering. 1-2, McGraw-Hill, New York, USA (1986).
- [3] Garfias, L., Gebert, A., Missett, N.: Corrosion of Electronic and Magnetic Materials, Issue 30. 15-17, The Electrochemical Society, Vienna (2010).
- [4] Hihara, L.H., Adler, R.P.I., Latanision, R.M.: Environmental Degradation of Advanced and Traditional Engineering Materials, CRC Press, 98 (2013).
- [5] Klink, S., Madej, E., Ventosa, E., Lindner, A., Schuhmann, W., La Mantia, F.: The importance of cell geometry for electrochemical impedance spectroscopy in three-electrode lithium ion battery test cells. *Electrochemistry Communications*, 22, 120-123 (2012).
- [6] Orazem, M.E., Tribollet, B.: *Electrochemical Impedance Spectroscopy*. Pennington, NJ, USA (2011).
- [7] Prenosil, M.: Volatile Corrosion Inhibitors Cortec Corp, 14-15 (2001).
- [8] Quitmeyer, J.A.: Amine Carboxylates: Additives in Metalworking Fluids. *Lubricating Engineering*, 52, 835 (1996).
- [9] Anon.: Research Opportunities in Corrosion Science and Engineering, Committee on Research Opportunities in Corrosion Science and Engineering, National Materials Advisory Board, Division on Engineering and Physical Sciences, National Research Council, National Academies Press, Washington D.C., USA (2011).

LOOKING FOR Zwick / Roell MACHINES?

Whether for static materials testing or the various forms of fatigue testing - we have the RIGHT SOLUTION FOR YOU!

- Universal Testing Machines
- Extrusion Plastometers
- Pendulum Impact Tester
- Hardness Testers
- Advance Creep Testing Machines
- Fatigue Testing Machines
- Drop Weight Testers
- Specimen Preparation Devices
- Ambient, Climate & High Temperature Furnaces



Reliable Test Results - Accurate, Repeatable, Reproducible & Traceable

We deliver premium customer value.



CALL US TO ENQUIRE
 +65 6778 3655

Email sales-sg@quantumsg.com • Log in to website www.zwick.com.sg



THE PLASTICS AND RUBBER INSTITUTE OF SINGAPORE

Tanglin Post Office Box 354 Singapore 912412

MEMBERSHIP/MEMBERSHIP UPGRADE APPLICATION FORM

Please fill and print out the form below and post back to:

The Membership Secretary
Plastics and Rubber Institute of Singapore
Tanglin Post Office Box 354
Singapore 912412

Name of Applicant: _____

Address (Home): _____

Telephone: (Home) _____ (Handphone) _____

Name & Address of Office: _____

Office Telephone/Fax: _____

Email Address: _____

Job Title / Responsibilities: _____

Date of Birth: _____

Course / Institution: _____ Year Graduated: _____

Other Qualifications: _____

Employment History:
(Please provide details of Job Title/Company/Years of Service)

For upgrading, please indicate: Current PRIS membership grade: _____

Grade applying for: _____

Date of Application: _____ Signature: _____